

Seismic Tomography with a Self-adaptive Parameterisation

Rado Faletič

This paper is submitted in partial fulfillment of a degree of
Bachelor of Science with Honours
The Australian National University

November 1997

Acknowledgements

I could not have undertaken this project without the *A.L. Hales Honours Year Scholarship* awarded to me by the Research School of Earth Science, ANU. I am also grateful for the assistance of many people throughout the year: Dr. Malcolm Sambridge for his guidance; Sri Widiyantoro and Professor Brian Kennett for their helpful discussions; Dr. Peter Hairsine for his constant encouragement; HJ, Mel, the other mathematics honours students and my family for their friendship and support.

Thank you.

Contents

| | |
|---|-----------|
| Acknowledgements | i |
| List of Figures | iv |
| Introduction | 1 |
| 1 Phenomena and Physics | 3 |
| 1.1 The Earth and Seismology | 3 |
| 1.1.1 History | 3 |
| 1.1.2 Seismic Sources | 5 |
| 1.1.3 Earth Structure | 6 |
| 1.2 Seismic Waves and Ray Theory | 7 |
| 1.2.1 Body Waves | 8 |
| 1.2.2 Surface Waves | 10 |
| 1.2.3 Ray Theory | 11 |
| 1.2.4 Phases | 14 |
| 2 Seismic Tomography | 17 |
| 2.1 Travel-time Tomography | 19 |
| 2.2 Parameterisations | 21 |
| 2.2.1 Spherical Grid | 22 |
| 2.2.2 Polyhedral Meshes | 22 |
| 2.2.3 Spherical Harmonics | 25 |
| 3 Self-adaptive Parameterisations | 27 |
| 3.1 Data and computational methods | 28 |
| 3.1.1 The Data | 28 |
| 3.1.2 Parameterisations | 28 |
| 3.1.3 Calculating the Fréchet Derivatives | 35 |
| 3.1.4 Matrix Techniques | 37 |
| 3.2 Refinement and results | 41 |

| | | |
|-------|--|-----------|
| 3.2.1 | Parameterisation Refinement | 41 |
| 3.2.2 | Plotting | 44 |
| 3.2.3 | Presentation and Discussion of Results | 45 |
| | Conclusion | 50 |
| | A Some Definitions and Theorems | 52 |
| A.1 | Snell's Law | 52 |
| A.2 | Useful Polynomials | 54 |
| A.3 | The Fréchet Derivative | 54 |
| | B Performance Figures | 56 |
| B.1 | Computing Times | 56 |
| B.2 | Model Statistics | 56 |
| | C Velocity Models | 59 |
| | Bibliography | 79 |

List of Figures

| | | |
|------|---|----|
| 1.1 | Global seismicity, 1975–1995. | 5 |
| 1.2 | Structural layers within the Earth. | 7 |
| 1.3 | The stress tensor. | 8 |
| 1.4 | Body waves in an elastic medium. | 10 |
| 1.5 | A ray traveling through the Earth. | 13 |
| 1.6 | Demonstrating triplication. | 15 |
| 1.7 | Some P and S wave phases. | 16 |
| 2.1 | Spherical parameterisation. | 23 |
| 2.2 | An example of a triangulation. | 24 |
| 3.1 | Geographical positions of the data used. | 29 |
| 3.2 | The icosahedron. | 30 |
| 3.3 | Three step refinement of a surface triangle on the icosahedron. | 32 |
| 3.4 | Refinements of the icosahedron. | 33 |
| 3.5 | Estimation of the cross section of a parameterisation. | 34 |
| 3.6 | The reference model, <i>ak135</i> . | 35 |
| 3.7 | Stepping along a ray path in a Delaunay triangulation. | 36 |
| 3.8 | Example of a definition for cell neighbours. | 38 |
| 3.9 | Defining cell neighbours used in this study. | 38 |
| 3.10 | Examples for nodal placement. | 43 |
| 3.11 | Bisection of a tetrahedron. | 43 |
| 3.12 | Model parameters for each parameterisation. | 47 |
| 3.13 | Variance reduction for each model. | 47 |
| A.1 | Demonstration of Snell’s law. | 52 |
| A.2 | Proving Snell’s law. | 53 |
| B.1 | Model convergence using % RMS as the indicator. | 57 |
| B.2 | Indicators of average cell properties. | 58 |

Introduction

Imaging of the Earth’s mantle through the mathematical process known as tomography has developed over the past twenty years, the most notably advances made with the introduction of new computing techniques. Of particular interest are tomographic problems using data from earthquakes, which come under the general classification of seismic tomography. Earthquake data sets can be extremely large, often containing hundreds of thousands of observational readings, so efficient numerical algorithms need to be implemented. Further complications arise when the available data is unevenly distributed around the globe, leading to a highly irregular sampling of the mantle, while heterogeneities within the mantle exhibit irregularities in both amplitude and shape.

Until recently, methods of performing seismic tomography on the mantle have been restricted to using regular parameterisations of the Earth, that is, parameterisations which do not take into account the irregular nature of the Earth. However, developments during the last ten years towards the construction of irregular grid structures for numerical problems have enabled their implementation to be of use to problems in the earth sciences. Of particular interest are grids, or meshes, which are composed entirely of tetrahedra. Such meshes can be easily adapted to suit the needs of a particular problem as they are capable of dividing a region of space into arbitrarily sized and distributed tetrahedra.

In seismic tomography, images of the mantle have a high dependence on the size and distribution of the data set used, and on the nature of the parameterisation. To use a parameterisation which “conforms” to the distribution of the data, such as employing smaller cells where data sampling is high, would increase the resolution of the tomographic image only in regions of adequate data coverage. However, this neglects the distribution of heterogeneities, which may or may not conform with the coverage of the data.

The purpose of this paper is to present a new, self-adaptive, form of parameterisation which will refine cell structure only where it is warranted. We will also examine the relationship, or trade-off, between the model fit and the nature of the refined parameterisations.

This paper commences with an introductory discussion of the nature of the Earth, and a presentation of seismic wave and ray theory. Chapter 1 will also describe the mathematical results which are important to the derivation of the seismic tomographic equations. The second chapter will derive these equations and their matrix representation through expanding the solution in terms of a finite basis, or parameterisation. A discussion of the most widely used parameterisations in seismic tomography will then be undertaken, with an emphasis on tetrahedral meshes. Chapter 3 describes the methodology which has been implemented to perform the tomographic inversions, discusses available options for mesh refinement, and presents an analysis of the results. It should be noted that some of the images have been reproduced in Appendix C. These results suggest that there is an inverse relationship between model fit and the number of parameters.

Chapter 1

Phenomena and Physics

1.1 The Earth and Seismology

Earthquakes are inelastic deformations within the Earth. The energy released from an earthquake is transmitted through the Earth by seismic waves (described in section 1.2.1), which cause deformations that are observed on the Earth's surface. Such deformations can cause havoc on man-made structures and natural landscapes. Entire cities have been destroyed as a result of earthquakes, and human casualties have been high in areas not prepared for the occurrence of a large earthquake. In addition, large scars can be created on the landscape due to the slippage of fault¹ zones during an earthquake.

In spite of this destruction, information gathered from earthquake events not only helps us improve the resistance of structures to damage during a quake, but also enables us to study the internal properties of the Earth from the characteristics of many earthquakes.

It was not until the end of the last century, with the creation of the seismometer, that the causes and physics of earthquakes could be quantitatively studied. More recently, major advances in the study of earthquake and earth structure have been made with the advent of computers. New theories about the structure and dynamics of the Earth have gone a long way to explaining where and how earthquakes occur.

1.1.1 History

Descriptions and attempted explanations of earthquakes can be traced back several millenia with the earliest records being made by the Chinese *circa* 1800 BC. The violent and uncontrollable nature of earthquakes has often led societies to

¹A fault is a plane of fractured rock.

believe them to be supernatural in origin, the work of gods or mythical creatures which dwell within the Earth [5, pg 2]. The prominent Greek philosophers Aristotle (384–322 BC) and Strabo (63 BC–AD 21) were among the first Europeans to begin cataloguing earthquake phenomena and speculating on the mechanics of their origin. Aristotle classed many earthquakes in terms of the ground motions they produced: vertical motion only, horizontal motion only, and so on. Both philosophers suggested that occasionally great winds from the sea would ignite combustible underground materials causing subsurface explosions, since it was observed that earthquakes more often occur near coastal regions [5, pp 3–4].

In the early 19th century it was believed that earthquakes, even strong events, were caused by falling debris, such as the collapse of cavern ceilings and landslides [14]. This theory, however, could not explain the release of vast amounts of energy necessary for many of the observed quakes, and once this was realised the search began for a more suitable theory. Such a theory was proposed in the 1960’s and is known as continental drift, which is now part of the broader theory of plate tectonics². This theory is largely consistent with the observed spatial pattern of earthquakes, Figure 1.1, which was not previously well understood [31, pg 49].

The first instrument for the measurement of earthquake properties was designed by a Chinese philosopher, Chang Heng, in AD 132. This instrument was designed for determining the initial direction of propagation of an earthquake, but it was also capable of detecting events some distance away. It was not until 1892 before a practical recording instrument was developed in Japan — the seismograph. Since then many devices have been developed, the simplest consisting of a large suspended weight which does not move significantly as the ground beneath it vibrates. Modern devices use systems of digital optic instruments to measure the stress and strain, due to Earth vibrations, of reference materials undergoing movements.

Along with the seismograph, another important factor in gaining knowledge about earthquakes has been the cataloguing of events, which did not take any consistent form until the mid 1700’s. Current catalogues describe thousands of earthquakes, but are still largely stored in analogue form. Modern high fidelity digital instrumentation directly digitises earthquake signals from seismometers

²A tectonic plate is in the outer portion of the Earth and consists of the crust and part of the mantle, called the lithosphere. Its boundary is defined as regions where it has significant motion with respect to adjacent lithosphere. Previously these boundaries were determined through zones of seismic activity (see Figure 1.1), although more recently global positioning systems (GPS) have been used to measure relative plate movements.

and records them in a compact electronic form, such as on computer disk.

1.1.2 Seismic Sources

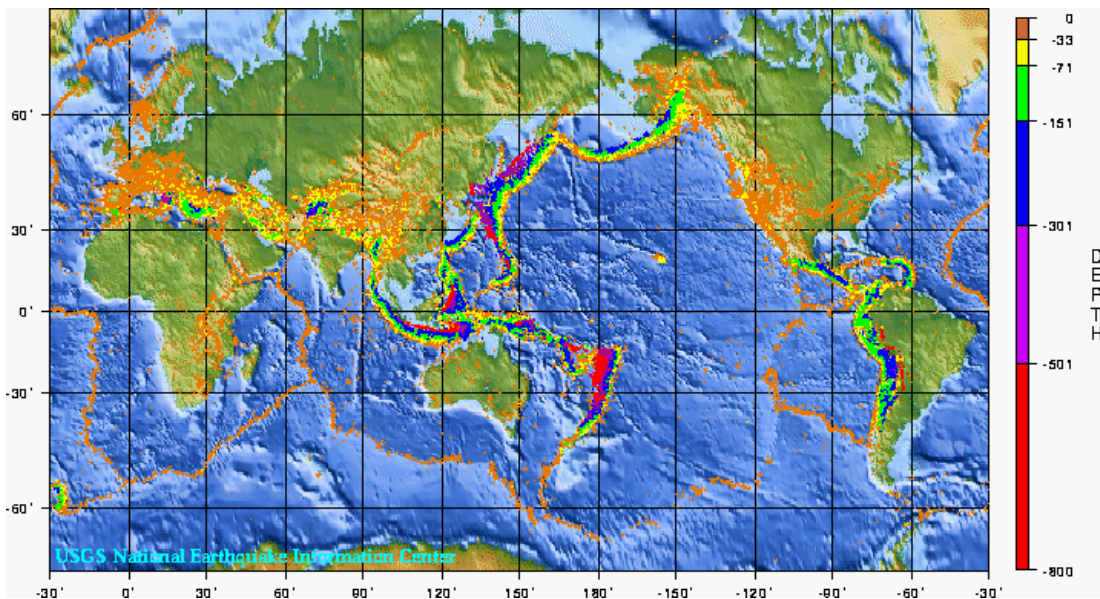


Figure 1.1: Global seismicity, 1975–1995.

As Figure 1.1 shows, most earthquakes are located in specific regions. These earthquakes are not all at the same depth, they vary from surface phenomena to about 700 km in depth. The regions near the surface of the Earth are known to be particularly interesting in terms of other geological features such as:

- active volcanos,
- island arcs,
- deep ocean trenches,
- oceanic ridges,
- mountain building (eg. the Himalayas).

It is worthwhile to note that seismic waves can also be generated by man-made sources, such as explosions (nuclear tests, blasting, etc.); a feature which is exploited for controlled experiments such as seismic prospecting. However, man-made sources release much less energy than many natural sources and are restricted to shallow depths. Earthquakes can also be triggered by the filling of man-made dams with water, such as occurred in the Snowy Mountains in New South Wales, as the water lubricates underlying rock fractures reducing friction.

Most quakes are tectonic in origin, that is, they result from the relative motion of the Earth’s tectonic plates. These plate interact through collisions, diversions and lateral “scraping”. There are several mechanisms by which tectonic earthquakes can be triggered. For events which occur close to the Earth’s surface, that is, in the crust, most can be explained by Reid’s elastic rebound theory, a theory which was first proposed to explain observations of earthquakes occurring along the San Andreas fault in San Francisco. This theory, proposed by Reid in 1911, states that if stresses in the Earth become too great for the constituent material, then it will fracture, causing an earthquake [48, pg 95]. The crust along either side of the San Andreas fault is moving propagates in opposite directions, so is subjected to lateral friction. If, however, the motion is obstructed, elastic strain may increase until the rock can no longer support it — causing an earthquake.

Reid’s theory is useful in explaining surface events, but it cannot explain events which occur deeper within the Earth. At greater depths the Earth’s material is able to sustain much greater stresses as it tends to behave more like a fluid (on a geological time scale, $\sim 10^6$ years) than surface material. One proposal for deep quakes is that material may undergo a phase change, to a phase which is more stable at the local temperature and pressure, which results in a sudden change of volume or shape producing a shock wave in the rock [18, pg 108]. Since deep earthquakes occur only in subducting lithosphere, another proposal for deep quakes is the dehydration of the descending slab. Dehydration can cause pore pressure to increase or lubrication along fault planes, both of which reduce friction, increasing movement in the rocks [32, pp 153–154]. In regions, such as tectonic plate interiors, where there is little or no plate activity, earthquakes are attributed to intra-plate stresses.

All processes described above produce a sudden displacement of material within the Earth. This releases elastic strain energy which then through the Earth in the form of seismic waves.

1.1.3 Earth Structure

Much of what is known about the internal structure of the Earth comes from earthquake observations, as seismic waves penetrate to all depths within the Earth. There are three basic “layers” in the Earth: crust, mantle and core, as depicted in Figure 1.2. The outer layer is the crust. There are two main type of crust: oceanic crust (about 7 km thick) which consists of basalt overlaid with sedimentary material; and continental crust (between 30–50 km thick) which consists of granite and sedimentary material overlying a basaltic layer. Below the

crust is the mantle, which is divided into two sublayers: the upper and lower mantle. The crust-mantle interface is called the Mohorovičić Discontinuity. The lower layer, occupying the centre of the Earth is the core, which is thought to consist of an inner solid, mostly iron, region and a bounding liquid region³.

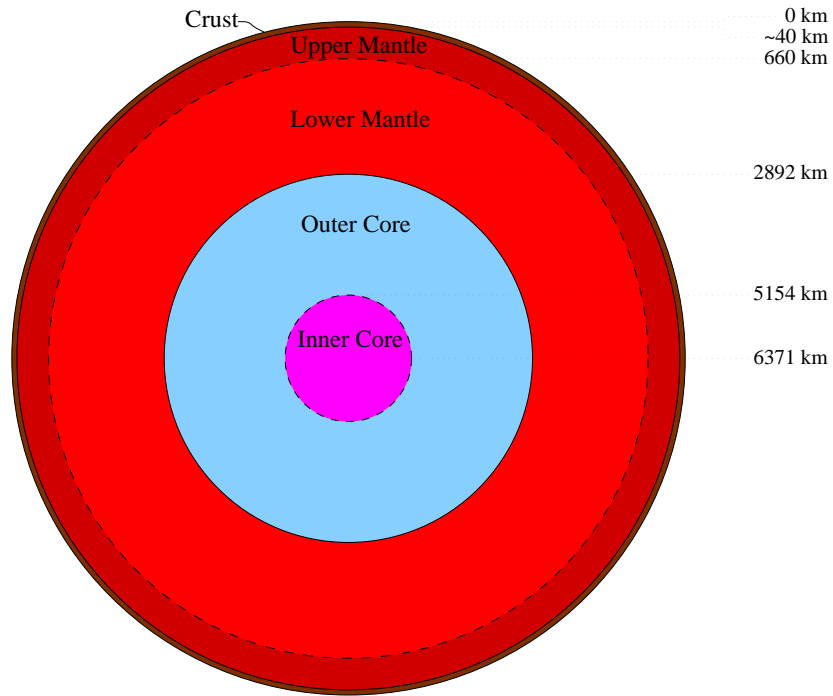


Figure 1.2: Structural layers within the Earth.

1.2 Seismic Waves and Ray Theory

The propagation of seismic waves in the Earth is governed by the elasticity properties of the materials from which it is made. These materials behave much like *dilatant compound* — a silicone polymer more commonly known as bouncing, or silly, putty [12]. If deformations are slow enough, on a geological time scale, then the material will flow elastically, like molten plastic. However, sudden movements cause the material to “snap”, releasing strain energy which is emitted as seismic waves.

Derivations for wave motion will follow those from Bullen [7, pp 110–120] and Bullen and Bolt [8, pp 30, 87–89]. The ray theory section is based on Bullen and Bolt [8, 154–156] and Nolet [40, pp 5–8].

³The outer core was first discovered to be liquid by its inability to support shear stresses through the transmission of shear waves (see section 1.2.1).

1.2.1 Body Waves

Balancing forces on any small volume element d^3r of material yields the elasticity equation⁴

$$\rho \frac{\partial^2 u_i}{\partial t^2} = \frac{\partial \sigma_{ij}}{\partial x_j} + f_i \quad (1.1)$$

where ρ is the density, u_i is the displacement in the direction x_i due to stresses (represented in the stress tensor σ_{ij}) and body forces f_i . The stress tensor σ_{ij} describes the force per unit area in the direction x_j on the plane face of d^3r perpendicular to x_i , the face being represented as (i) in Figure 1.3. It is usual

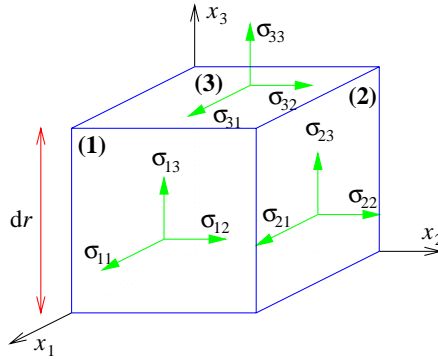


Figure 1.3: The stress tensor.

to only consider gravity in the body force term, setting $f_i = \rho \frac{\partial \mathcal{U}}{\partial x^i}$ where \mathcal{U} is the gravitational potential.

In a perfectly elastic isotropic⁵ solid the stress tensor may be rewritten as

$$\sigma_{ij} = \lambda \theta \delta_{ij} + 2\mu \left(\frac{\partial u_j}{\partial x^i} + \frac{\partial u_i}{\partial x^j} \right). \quad (1.2)$$

$\theta = \text{div } \mathbf{u}$ is the dilation, μ is the shear modulus, $\lambda = \kappa - \frac{2}{3}\mu$ is Lamé's parameter where κ is the bulk modulus, and $\frac{1}{2} \left(\frac{\partial u_j}{\partial x^i} + \frac{\partial u_i}{\partial x^j} \right)$ is the Cauchy strain tensor. It is usual to assume that the material is uniform (at least locally) so that λ and μ are constants. Then substituting 1.2 into 1.1 we get, in vector form,

$$\rho \frac{\partial^2 \mathbf{u}}{\partial t^2} = (\lambda + \mu) \nabla \theta + \mu \nabla^2 \mathbf{u} + \rho \nabla \mathcal{U}. \quad (1.3)$$

Defining new constants $\alpha = \sqrt{\frac{\lambda+2\mu}{\rho}}$ and $\beta = \sqrt{\frac{\mu}{\rho}}$, and setting $\boldsymbol{\xi} = \nabla \times \mathbf{u}$ equation 1.3 can be rewritten as

$$\frac{\partial^2 \mathbf{u}}{\partial t^2} = \alpha^2 \nabla \theta - \beta^2 \nabla \times \boldsymbol{\xi} + \nabla \mathcal{U}. \quad (1.4)$$

⁴The Einstein summation convention is used throughout. Repeated indices are summed over only if one index appears “up” and one “down”.

⁵Isotropicity is a good approximation to the nature of the materials within the Earth.

Taking, separately, the divergence and curl of this equation gives

$$\frac{\partial^2 \theta}{\partial t^2} = \alpha^2 \nabla^2 \theta + \nabla^2 \mathcal{U} \quad (1.5)$$

and

$$\frac{\partial^2 \boldsymbol{\xi}}{\partial t^2} = \beta^2 \nabla^2 \boldsymbol{\xi}. \quad (1.6)$$

It has been shown (Jeffreys, 1931) that the gravity term $\nabla^2 \mathcal{U}$ in 1.5 has little influence on the solution for \mathbf{u} , so it will be neglected, giving

$$\frac{\partial^2 \theta}{\partial t^2} = \alpha^2 \nabla^2 \theta. \quad (1.7)$$

Equations 1.7 and 1.6 are then scalar and vector wave equations respectively. 1.7 describes an irrotational wave traveling with speed α , and 1.6 a rotational wave traveling with speed β . The terms “rotational” and “irrotational” describe the nature of the motion. Mathematically they correspond to the fact that \mathbf{u} can be written as

$$\mathbf{u} = \nabla \phi - \nabla \times \boldsymbol{\psi}$$

where ϕ is a scalar potential and $\boldsymbol{\psi}$ is a vector potential ($\operatorname{div} \boldsymbol{\psi} = 0$). The irrotational wave is described completely by the scalar potential $\theta = \nabla^2 \phi$, and likewise the rotational wave is described completely by the vector potential $\boldsymbol{\xi} = \nabla^2 \boldsymbol{\psi}$.

If plane wave propagation is assumed, that is, we seek a solution of the form $\mathbf{u}(\mathbf{r}, t) = \mathbf{A}(\mathbf{r}) e^{i(\mathbf{k} \cdot \mathbf{r} - \omega t)}$ where \mathbf{k} is the wave vector⁶ and $\omega = \frac{kv}{2\pi}$ is the frequency of the plane wave and v is the wave velocity, then substitution of this solution into 1.4 will result in a cubic equation in v^2 with a single root at α^2 and a double root at β^2 . The root at $v = \alpha$ corresponds to the irrotational wave, equation 1.7, of which the plane wave form is a compressional wave. In seismology this is called a primary wave, or P wave (see Figure 1.4(a)), as $\alpha > \beta$, so it is the first wave to be detected at the surface of the Earth. The two solutions for $v = \beta$ correspond to the rotational wave in equation 1.6. The plane wave analogue of a rotational wave is a shear wave (secondary, or S wave, in seismology, see Figure 1.4(b)), and the two solutions give waves which are polarised orthogonally to one another. A purely horizontally polarised wave is denoted SH, whilst a purely vertically polarised wave is referred to as SV. In a perfect fluid $\mu = 0$, in which case $\beta = 0$. So, fluids cannot support rotational waves, and the fact that no S waves travel through the outer core proves that it is liquid.

⁶The wave vector \mathbf{k} has magnitude equal to $k = \frac{2\pi}{\lambda}$, where λ is the wavelength, and direction equal to the direction of wavefront propagation.

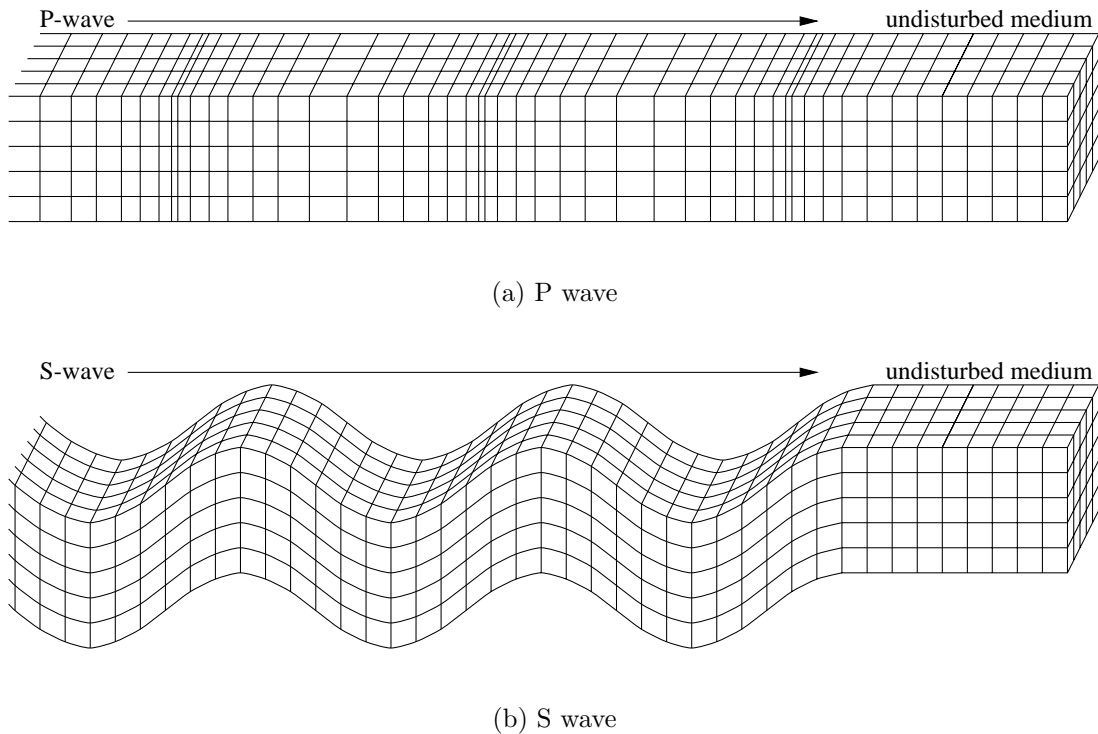


Figure 1.4: Body waves in an elastic medium.

1.2.2 Surface Waves

There also exist surface waves which are restricted to travel on the surface of the Earth, that is, the surface acts as a waveguide for seismic waves. These waves result from interactions of body waves with the free surface. There are two types of waves, named after the scientists who first predicted them, Rayleigh and Love. The motion of these waves can be formulated by rewriting equation 1.3 in terms of the potentials ϕ and ψ and considering plane wave solutions traveling parallel with the Earth's surface. Boundary conditions and observational requirements then dictate the form in which the plane waves take (see Bullen [7, pp 115–120] for detail on how this is performed).

Rayleigh waves travel like ocean waves, particles oscillate in an elliptical motion in the plane which lies along the direction of wave propagation and perpendicular to the surface [54, pg 215], a combination of P and SV. The speed of Rayleigh waves is given by the solution v_R to the following polynomial

$$\left(2 - \frac{v_R^2}{\beta^2}\right)^4 = 16 \left(1 - \frac{v_R^2}{\alpha^2}\right) \left(1 - \frac{v_R^2}{\beta^2}\right).$$

This has exactly one real valued solution for v_R , which is less than β in value.

Love waves need more than just a free surface to propagate, they require a “layer” of material beneath the boundary, and are purely SH. The nature of Love

waves will be affected by the properties of both the layered medium and the medium directly below it. If d is the thickness of the layer, then the equation for the velocity of Love waves (using symbols with dashes to represent properties of the layer) is

$$\mu \left(1 - \frac{v_L^2}{\beta^2}\right)^{\frac{1}{2}} = \mu' \left(\frac{v_L^2}{\beta'^2} - 1\right)^{\frac{1}{2}} \tan \left(kd \left(\frac{v_L^2}{\beta'^2} - 1\right)^{\frac{1}{2}}\right).$$

A solution for v_L exists only when $\beta' < v_L < \beta$, which is usually satisfied near the Earth's surface. Also note the dependence of the velocity of this wave on the wave number $k (= \frac{2\pi}{\lambda})$, meaning it is a dispersive wave.

1.2.3 Ray Theory

Ray theory is a tractable simplification of the full elastic wave equation, 1.3, and has had much success in explaining the main features of seismograms recorded at the Earth's surface. This theory can be derived by assuming a plane wave solution and substituting into 1.3, ignoring the gravity term. The plane wave solution assumed before was $\mathbf{u}(\mathbf{r}, t) = \mathbf{A}(\mathbf{r})e^{i(\mathbf{k} \cdot \mathbf{r} - \omega t)}$. It becomes more appropriate here to use a different form for a plane wave,

$$\mathbf{u}(\mathbf{r}, t) = \mathbf{A}(\mathbf{r})e^{i\omega(\tau(\mathbf{r}) - t)} \quad (1.8)$$

where $\tau(\mathbf{r})$ defines wave fronts upon setting $\tau(\mathbf{r}) = t$ for any given t . Substitution of 1.8 into 1.3 gives

$$\begin{aligned} -\rho\omega^2 \mathbf{A} e^{i\omega(\tau-t)} &= (\lambda + \mu) (\nabla (\nabla \cdot \mathbf{A}) + i\omega \nabla \tau (\nabla \cdot \mathbf{A}) \\ &\quad + i\omega \nabla (\mathbf{A} \cdot \nabla \tau) - \omega^2 (\mathbf{A} \cdot \nabla \tau) \nabla \tau) e^{i\omega(\tau-t)} \\ &\quad + \mu (\nabla^2 \mathbf{A} + i\omega \mathbf{A} \nabla^2 \tau - \omega^2 \mathbf{A} \|\nabla \tau\|^2) e^{i\omega(\tau-t)}. \end{aligned} \quad (1.9)$$

As can be seen, this equation has terms in ω of order zero, one and two. To be able to consider rays, we need to make the high frequency approximation ($\omega \rightarrow \infty$ or $\lambda \rightarrow 0$), an approximation which is valid in the Earth provided the wavelength is much smaller than any anomalies encountered by the wave [36, pg 9]. So, implementing this approximation gives

$$(\lambda + \mu) (\mathbf{A} \cdot \nabla \tau) \nabla \tau + \mu \mathbf{A} \|\nabla \tau\|^2 - \rho \mathbf{A} = \mathbf{0}. \quad (1.10)$$

This has two non-trivial solutions:

$$\mathbf{A} = c \nabla \tau \Rightarrow (\lambda + \mu) \|\nabla \tau\|^2 + \mu \|\nabla \tau\|^2 - \rho = 0 \quad (1.11)$$

$$\mathbf{A} \cdot \nabla \tau = 0 \Rightarrow \mu \|\nabla \tau\|^2 - \rho = 0 \quad (1.12)$$

where c is an arbitrary constant. Rewriting these equations give the following⁷

$$\|\nabla\tau\| = \sqrt{\frac{\rho}{\lambda + 2\mu}} = \frac{1}{\alpha} \quad (1.13)$$

$$\|\nabla\tau\| = \sqrt{\frac{\rho}{\mu}} = \frac{1}{\beta} \quad (1.14)$$

where α and β are the P and S wave velocities respectively. Now, since τ has been defined for constant wavefronts it follows that $\nabla\tau$ lies in the direction of wave propagation (perpendicular to the wavefronts). From this it can easily be seen, using 1.11 and 1.12, that 1.13 corresponds to P wave motion, and 1.14 to S waves.

A general velocity function v will be used from here on to represent α and β , in which case 1.13 and 1.14 reduce to $\|\nabla\tau\| = \frac{1}{v}$. This is a non-linear first order partial differential equation (PDE) in τ . To transform this into a first order system define the slowness vector⁸ \mathbf{s} by $\mathbf{s} = \nabla\tau$ which is clearly parallel to the wave propagation, as shown in Figure 1.5. The method of characteristics from PDE theory then yields characteristic curves, seismic rays, which are solutions to

$$\frac{d\mathbf{r}}{d\tau} = v^2 \mathbf{s}, \quad \frac{d\mathbf{s}}{d\tau} = -\frac{1}{v} \nabla v \quad (1.15)$$

given the initial position \mathbf{r}_0 , initial direction \mathbf{p}_0 and initial phase τ_0 . This is a system of first order ordinary differential equations in \mathbf{s} and \mathbf{r} , which has analytic solutions for simple variations in v , and can otherwise be solved by standard numerical methods [1, pg 723]. It should be noted here that, along with the high frequency approximation, ray theory is only valid for a point source (ie. the source region is much smaller than the wavelength). This breaks down in the vicinity of earthquakes of large magnitude, as the source may consist of an extensive fault region. However, in the far field the size of the earthquake is of little consequence and so ray theory can be applied.

An important case is one in which the velocity profile varies with depth only, ie. $v = v(r)$, as it is this variation which is dominant in the Earth. In this case $\nabla v = (\frac{\partial v}{\partial r}, 0, 0)$ which, from 1.15, implies that s_θ and s_ϕ are constants, where $\mathbf{s} = (s_r, s_\theta, s_\phi)$ in spherical coordinates. This gives immediately that $\frac{r \sin i}{v} = \text{constant}$ by noting that (s_θ, s_ϕ) constitutes the non-radial component of the slowness and then using Figure 1.5, where i is the angle the ray makes with the radial direction. This is simply a statement of Snell's law (Appendix A.1) [40, pg 5]. The quantity

⁷This form of equation, $\|\nabla\tau\| = \frac{1}{v}$. is called an eikonal equations for the location of the wavefront τ .

⁸If \mathbf{v} is the velocity vector then $\mathbf{s} = \frac{\mathbf{v}}{v^2}$ is defined as the slowness vector and $s = v^{-1}$ is simply called the slowness.

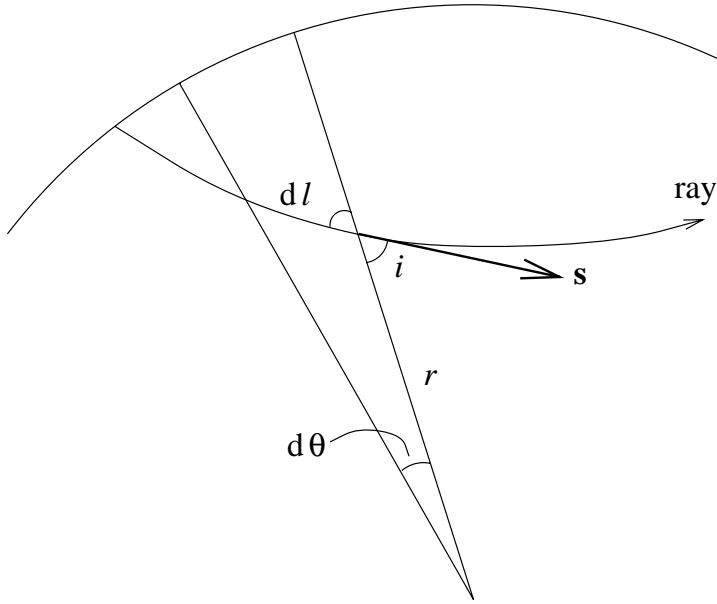


Figure 1.5: A ray traveling through the Earth.

$p = \frac{r \sin i}{v}$ is called the ray parameter and, as mentioned above, is constant along any given ray.

Using the ray parameter and that $(dl)^2 = (dr)^2 + r^2(d\theta)^2$ (where dl is the ray segment as shown in Figure 1.5) we can follow a ray from radius r_1 to radius r_2 to give the travel-time for that segment, T , and angular separation of the endpoints, Δ , as functions of p . The derivation is given in Bullen and Bolt [8, pp 157–158] and yields

$$T(p) = \int_{r_1}^{r_2} \frac{r}{v(r^2 - v^2 p^2)^{\frac{1}{2}}} dr \quad (1.16)$$

$$\Delta(p) = \int_{r_1}^{r_2} \frac{vp}{r(r^2 - v^2 p^2)^{\frac{1}{2}}} dr. \quad (1.17)$$

These can then be used to follow a ray path, for a given value of p and a velocity variation v . Conversely, if T_{total} and Δ_{total} are known, where the subscript “total” refers to the total length of the ray path, then $p = \frac{dT}{d\Delta}$ [8, pp 156–157]. Analytic solution to 1.16 and 1.17 can be found for certain specific velocity functions, the most important of which are the linear variation, $v(r) = a + br$, circular rays $v = a - br^2$ (called circular as it produces rays which are circles of radius $\frac{1}{2pb}$), and Mohorovičić’s law $v = ar^b$, where a and b are constants.

Another important consequence of the characteristic equations 1.15 is that they define rays which satisfy Fermat’s principle. Given any two points P_1 and P_2 in the Earth we would like to know the path a seismic ray will take from P_1 to P_2 . Then, Fermat’s principle can be stated as:

Theorem 1.2.1 (Fermat’s principle) *The path a seismic ray takes, Γ , from*

P_1 to P_2 is given by the following condition on the path integral of the slowness of the wave in the medium

$$\frac{d}{d\Gamma} \int_{\Gamma} s(\mathbf{r}) dl = 0, \quad (1.18)$$

where $d\Gamma$ represents small perturbations in the ray path Γ .

The integral in equation 1.18 is in units of time, but it is important to note that the condition does not necessarily give a path which is time minimising between P_1 and P_2 . More generally, it ensures that the travel time is stationary with respect to ray path perturbations.

The ray equations 1.15 can be combined to give a second order PDE

$$\nabla s = \frac{d}{dl} \left(s \frac{d\mathbf{r}}{dl} \right) \quad (1.19)$$

where dl is a ray segment ($dl = \|d\mathbf{r}\|$). Using this equation one can derive Fermat's principle using first order perturbation theory [53]. Conversely, starting with Fermat's principle it is possible to derive equation 1.19 [40, pg 8]. This is an important property, as it means that seismic rays will satisfy Fermat's principle.

1.2.4 Phases

As seismic waves propagate through the Earth they may reflect and refract from discontinuities, such as the core-mantle boundary (CMB) or the inner core boundary, or even from the surface of the Earth. It is also possible for S waves to be transformed into P waves, and vice versa, along the CMB. As a consequence, waves may traverse more than one path between source and receiver [20, pg 42]. This leads to the recording of more than one arrival time for each type of wave, P and S, which are termed “phases”. Considering P waves only, a ray which travels from source to receiver without undergoing any reflections is called a *P* phase. If the ray makes one reflection off the surface of the Earth it is termed a *PP* phase, or *pP* if the angle of incidence is low, *PPP* for two reflections and so on. If a P wave reflects off the CMB the letter *c* is used, and off the inner core is *i*. A P wave traveling through the outer core is denoted *K* and through the inner core with an *I*. All of these terms, and their corresponding geometric descriptions, are demonstrated in Figure 1.7(a).

The importance of the various phases is that each phase traverses and samples different regions of the Earth. For example, *pP*, not shown in the figure, is an important phase in determining the depth of an earthquake as it corresponds to a ray which is initially directed towards the surface of the Earth. In particular,

looking at the time differences between various phases at the Earth's surface provides information about Earth structure. However, on a seismogram some phases are obscured by background "seismic noise" due to their relatively small amplitude, making their arrival times difficult to pick. Another problem is that of triplication, a single wave type being recorded at a station at three distinct arrival times as demonstrated in Figure 1.6. This comes about from refraction

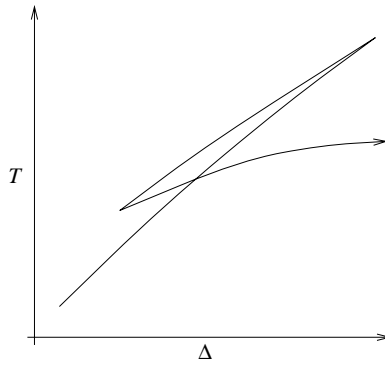


Figure 1.6: Demonstrating triplication.

within the Earth allowing different rays to converge at the same point on the Earth's surface. Often, in global studies, only the first arriving *P* phase is used, to avoid the incorrect arrival time readings for the other phases.

Figure 1.7(b) also depicts *P* wave phases in the top half, along with some of the *S* wave phases in the lower half. Notice those *S* phases which are transformed into *P* or *K* through interactions with the CMB.

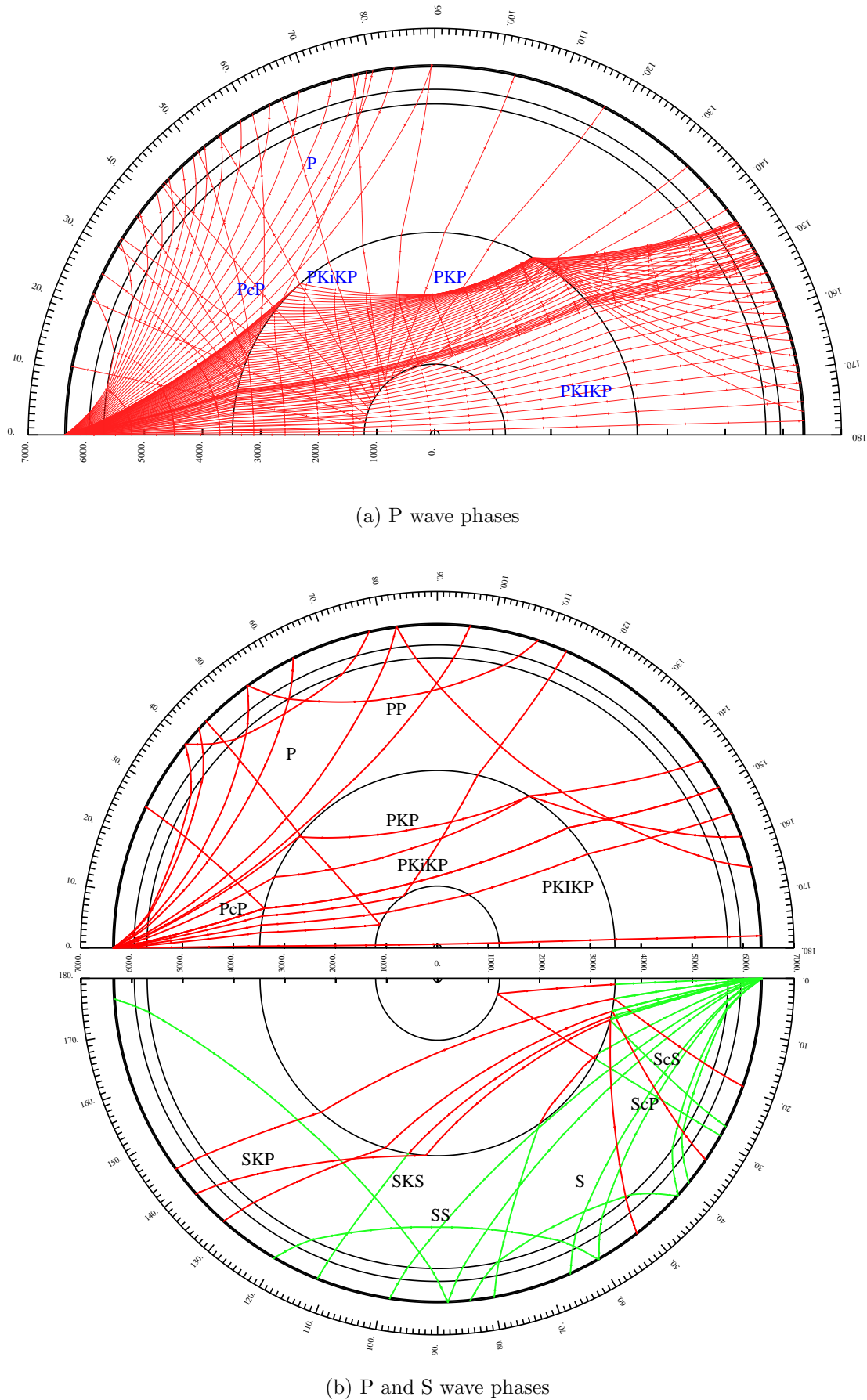


Figure 1.7: Some P and S wave phases.

Chapter 2

Seismic Tomography

In seismic tomography we are concerned with the reconstruction of the two or three dimensional variations in seismic wavespeed (α and β). From knowing these variations it is possible to develop models which may represent physical properties such as density or temperature. For example, an approximate guide to temperature variations is that waves generally travel faster through cold material than they do through hot. The space of all Earth models, where an Earth model is a finite valued function $f : E (= \{\mathbf{r} \in R^3 : \mathbf{r} \in \text{Earth}\}) \rightarrow R$, is a subspace of the Hilbert space $L_2(E)$.

In section 1.2.3 it was shown how elasticity theory gave rise to the ray theory approximation for the propagation of seismic disturbances. In seismic tomography rays can be used to probe the Earth, analogously to X-rays in medical tomography (computer assisted tomography (CAT) scans). However, there are some major differences. In medical tomography both the source and receiver positions are known to high accuracy, and the X-rays traverse straight paths from source to receiver. In contrast, only the receiver location is known to high accuracy for a seismic ray, although the epicentre¹ is often known to sufficient accuracy, and the rays traverse curved paths whose shape depends on the wavespeed structure of the Earth.

Problems in seismic tomography range from local to global in scale. Localised problems are essentially involved with seismic exploration, whereas global tomography is usually concerned with studying larger features of the Earth such as plate subduction. The broad spectrum of applications of tomography demand a wide variety of techniques.

Seismic exploration is carried out for a number of reasons, the main ones being the locating of hydrocarbon and ore reservoirs, and the determining their geome-

¹The epicentre is the projection of the earthquake source onto the surface of the Earth.

tries [36, pg vii]. The two main techniques employed are cross well, or cross hole or cross bore, tomography and seismic reflection. Cross well tomography involves using wells in which to place an artificial seismic source, such as explosives, and seismic receivers. The waves which propagate from source to receiver probe the region between wells, the information from which can then be used in a tomographic inversion [36, pg 1]. The sources and receivers are placed so as to achieve optimal ray coverage of the sample region, whose dimensions range from less than 100 m to several kilometres. Seismic reflection is concerned with analysing reflection data from downwards propagating waves, and is usually performed by placing a source and receiver very close together then recording the reflections of waves from rock interfaces in the crust. The nature of the reflections often indicate the presence of certain minerals, allowing ore bodies to be located [44, pg 203].

In contrast to these controlled experiments, the data for global tomography is usually derived from natural seismic sources and recorded at fixed locations worldwide. This often means that the ray coverage is not optimised: earthquakes occurring primarily along plate boundaries and recording stations being positioned mainly in areas of interest on land. The general aim of global tomography is to gain understanding of the internal dynamics of the Earth, often through investigating the lateral structure [54, pg 254].

The most common type of data used in tomographic problems is that of the travel times of seismic waves from sources to receivers, being the basis for travel-time tomography. From a source to receiver there is one travel time for any given phase, and it is usual to consider phases separately. If one were to incorporate data from as many phases as possible, for a given event and receiver, then the data would essentially consist of the entire seismogram. This can be used, by modeling a synthetic seismogram based on the model parameters, to deduce suitable models. This form of tomography is known as waveform tomography [41, pg 301]. Typically, there are a large number of model parameters involved in such a problem, and the equations relating the data to the model parameters are nonlinear, hence waveform tomography is not as easily implemented as its travel-time counterpart. A third tomographic method is the modeling of the normal modes of vibration², spheroidal and toroidal, of the Earth to determine its internal characteristics [52, pg 23].

This chapter will discuss the most common techniques of travel-time tomog-

²When the Earth is disturbed, such as the occurrence of an earthquake, it will vibrate at particular frequencies, much like the characteristic frequencies of a bell when struck with a hammer.

rathy, some of which are also used in other forms of tomography, and comment on their suitabilities and weaknesses.

2.1 Travel-time Tomography

The most utilised form of tomography is that involving the travel-time of a seismic wave from source to receiver. For any given earthquake, observation stations on the surface of the Earth will record the arrival time of various waves (phases) associated with that event: P wave, S wave, surface waves and various reflected waves. Suppose the arrival time of a particular phase at a given station is T_i^a . The hypocentral³ coordinates $(X_i^h, Y_i^h, Z_i^h, T_i^h)$, where X_i^h , Y_i^h and Z_i^h are general three dimensional coordinates, typically geographical with X_i^h being colongitude, Y_i^h colatitude and Z_i^h the depth from sea level, are not known. Estimates of these coordinates are made by assuming a velocity model of the Earth, typically one which is dependent on depth only, and applying a least squares method to all arrival time data for many receivers. The main indicator is the difference in arrival time between the P and S wave phases. The epicentral coordinates can usually be estimated to sufficient accuracy, but the depth to the hypocentre is much less resolved (between 2–100 km), and the event time can be calculated to within several seconds. The accuracy of these estimations depends on the distribution of stations about the event.

Set the travel-time to be $T_i = T_i^a - T_i^h$. Since section 1.2.3 demonstrated that we can consider rays, we can integrate along the ray path Γ_i from (X_i^h, Y_i^h, Z_i^h) to the receiver to get

$$T_i = \int_{\Gamma_i} \frac{1}{v(\mathbf{r})} dl, \quad (2.1)$$

where dl is an element of length along the path Γ_i . If weights associated with the data are to be included, perhaps relating to data error, then it is standard to include a data kernel $G_i(\mathbf{r})$ to give $T_i = \int_{\Gamma_i} G_i(\mathbf{r}) \frac{1}{v(\mathbf{r})} dl$.

Equation 2.1 is nonlinear: dependence on v^{-1} and an unknown ray path Γ_i . It is desirable to linearise this equation about a known ray path. So, suppose we have an initial reference model, typically one which has spherical symmetry, $v_o = v_o(r)$. This enables the use of 1.15 to trace the ray either from source to receiver or vice-versa, hence deducing the ray path Γ_{0i} . We can calculate the travel time under this model by an integral along the ray path in the reference

³The hypocentre is the actual position of the earthquake, assuming a point source, including the time of the event.

model $v_o(r)$

$$T_{0i} = \int_{\Gamma_{0i}} \frac{1}{v_0} dl. \quad (2.2)$$

Define the slowness as $s = v^{-1}$, which allows us to rewrite equations 2.1 and 2.2 as

$$T_i = \int_{\Gamma_i} s dl \quad (2.3)$$

$$T_{0i} = \int_{\Gamma_{0i}} s_0 dl. \quad (2.4)$$

What we then seek is the difference, in travel-time, between T_i and T_{0i} , so define the travel-time residual as $\delta T_i = T_i - T_{0i}$. Combining 2.3 and 2.4 then gives

$$\delta T_i = \int_{\Gamma_i} s dl - \int_{\Gamma_{0i}} s_0 dl. \quad (2.5)$$

If we suppose that the perturbation in the slowness is small (deriving from a small perturbation in velocity), ie. $\delta s \ll s$ where δs is defined by $s \approx s_0 + \delta s$, then the perturbation in Γ_i , with respect to Γ_{0i} , will also be small. This enables us to use Fermat's principle (Theorem 1.18). Firstly,

$$\begin{aligned} \delta T_i &= \int_{\Gamma_i} s dl - \int_{\Gamma_{0i}} s_0 dl \\ &\approx \int_{\Gamma_i} (s_0 + \delta s) dl - \int_{\Gamma_{0i}} s_0 dl. \end{aligned}$$

Now, supposing that $\Gamma_i \approx \Gamma_{0i} + \delta\Gamma_i$ we have

$$\begin{aligned} \int_{\Gamma_i} (s_0 + \delta s) dl &\approx \int_{\Gamma_{0i}} (s_0 + \delta s) dl + \int_{\delta\Gamma_i} (s_0 + \delta s) dl \\ &= \int_{\Gamma_{0i}} s_0 dl + \int_{\Gamma_{0i}} \delta s dl + \int_{\delta\Gamma_i} s_0 dl + \int_{\delta\Gamma_i} \delta s dl. \end{aligned}$$

The last term is second order, so is discarded, and the second last term is an integral over the perturbation in the ray path which, by Fermat's principle, is zero. Therefore

$$\begin{aligned} \delta T_i &\approx \int_{\Gamma_{0i}} s_0 dl + \int_{\Gamma_{0i}} \delta s dl - \int_{\Gamma_{0i}} s_0 dl \\ &= \int_{\Gamma_{0i}} \delta s dl. \end{aligned} \quad (2.6)$$

So, the problem of solving for v in equation 2.1 has thus reduced to solving for δs in 2.6.

The solution, δs , to equation 2.6 is most commonly found by approximating δs in terms of a finite⁴ basis $\{e_j(\mathbf{r})\}_{j=1}^m$

$$\delta s \approx c^j e_j \quad (2.7)$$

⁴Finiteness is necessary as the solution is to be calculated by computer.

where $c_j = (\delta s, e_j)$.⁵ So,

$$\begin{aligned}\delta T_i &\approx \int_{\Gamma_{0i}} c^j e_j \, dl \\ &= c^j \int_{\Gamma_{0i}} e_j \, dl \\ &= A_{ij} c^j\end{aligned}$$

where the Fréchet derivative matrix (see appendix A.3) A_{ij} is given by

$$A_{ij} = \int_{\Gamma_{0i}} e_j \, dl. \quad (2.8)$$

If we suppose that we are considering n rays in total, then we can rewrite this in vector notation

$$\delta \mathbf{T} = A \mathbf{c} \quad (2.9)$$

where A is an $n \times m$ matrix, \mathbf{c} is an m -vector and $\delta \mathbf{T}$ is the n -data vector. There are many algorithms available to solve such a system, such as *Conjugate Gradient* and *Simultaneous Iterative Reconstruction Technique* methods. In the typical seismic tomographic problem $n > m$.

2.2 Parameterisations

The basis functions e_j , used to generate the matrix elements A_{ij} , can take on many suitable forms, the most common fall into two categories:

1. block parameterisation,
2. spherical harmonics.

Both types of basis have been employed successfully in imaging the structure of the Earth. However, each basis is suited to different purposes. For example, van der Hilst *et al.* [55] have used a fine block parameterisation to study the convective properties of the mantle, and Dziewonski [17] has used spherical harmonics to study the lateral variations in the lower mantle, and in particular the core-mantle boundary (CMB). The discussion which follows will describe key basis and parameterisations used, their qualities and results.

Block parameterisations involve subdividing the Earth into three dimensional regions, called blocks or cells. A suitable basis for this parameterisation takes the

⁵(f, g) = $\int_E f(\mathbf{r})g(\mathbf{r}) \, d^3\mathbf{r}$ is the inner product on $L^2(E)$.

form

$$e_j(\mathbf{r}) = \begin{cases} f_j(\text{cell } j) & \mathbf{r} \in \text{cell } j \\ 0 & \mathbf{r} \notin \text{cell } j \end{cases} \quad (2.10)$$

where f_j is a function of the j -th cell only. For example, a simple function is $f_j = 1$. It is more constructive to use an orthonormal basis, in which case, using the $L^2(E)$ norm, $f_j = V_j^{-\frac{1}{2}}$ with V_j being the volume of cell j .

2.2.1 Spherical Grid

Until recently only one type of block parameterisations has been dominant: the spherical grid. As the Earth is spherically symmetric it makes sense to use a parameterisation based on spherical coordinates. This spherical grid can be customised using irregular depth intervals, possibly to match with interfaces such as the Mohorovičić Discontinuity or the CMB. Figure 2.1 depicts a $2^\circ \times 2^\circ$ parameterisation with irregular depth layers as used by Widiyantoro [58] to conform with such interfaces. Inoue *et al.* [29] use different depth layers, given by a quadratic

$$d_i = 2600 \left(\frac{i}{16} \right)^2 + 300 \frac{i}{16}, \quad i = 0, 1, \dots, 16,$$

where d_i is the depth to interface i , and a surface cell size of $5.625^\circ \times 5.625^\circ$. These parameterisations have been designed for studying the mantle only, so there is no cell coverage of the core.

However, this type of parameterisation has a significant problem with the distribution of cell sizes. Although uniform cell sizes are not necessarily desirable, introducing resolution and model bias by using differing cell sizes may be a desired effect, the spherical parameterisation has much smaller cells surrounding the poles than around the equator. This means that the resolution of any model will be much better close to the polar axis. The cell density being greater at the poles also causes models to be biased at these regions. Another flaw is that the cells at the poles create a singularity, in that rather than projecting a spherical quadrilateral on the surface of the Earth they project a spherical triangle⁶.

2.2.2 Polyhedral Meshes

Recent years has seen the introduction of polyhedral meshes in tomographic problems [23, 51]. These consist of a series of nodes and edges from which the polyhe-

⁶Given a polygon whose vertices lie on the surface of a sphere, the spherical version of this polygon consists of the same vertices connected with the arcs of great circles rather than straight lines.

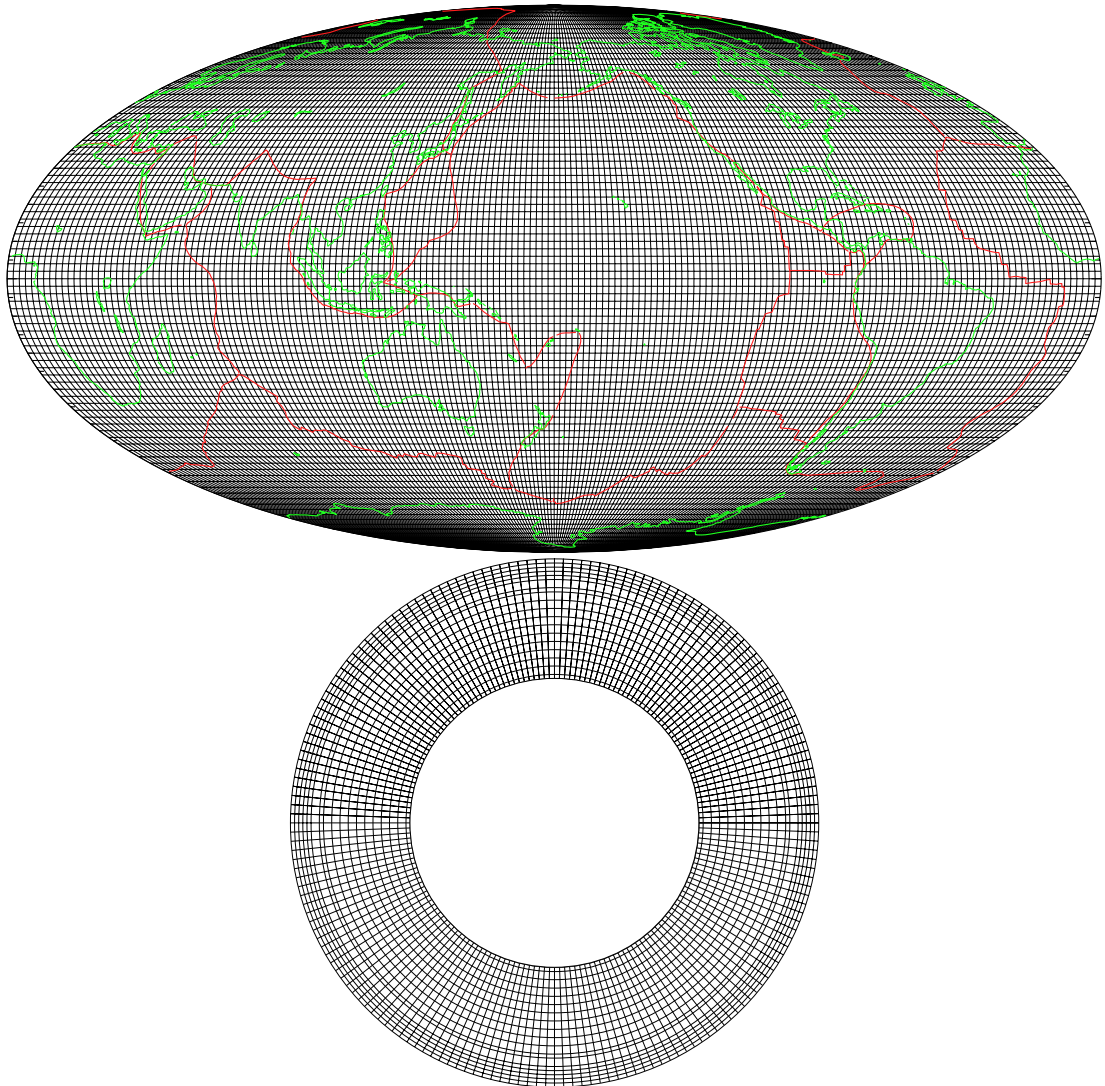


Figure 2.1: Spherical parameterisation.

dra are defined. For example, a cube is defined by eight nodes and twelve edges. A polyhedral mesh may consist of different classes of polyhedra interdispersed amongst each other, but the simplest example consists purely of tetrahedra. Unlike other polyhedra, a tetrahedron is defined completely by four nodes since each node is connected by an edge to each other node. A polyhedral mesh consisting solely of tetrahedra is called a tetrahedral mesh and the process of creating such a mesh from a sequence of nodes is called a tetrahedralisation.

In two dimensions a tetrahedralisation reduces to a triangulation, Figure 2.2 gives an example of a triangulation. Since a tetrahedralisation is difficult to visualise I will demonstrate the defining vertices for a triangulation, which will then carry over into three dimensions. For the triangulation shown in Figure 2.2 the defining list of nodes, or vertices, is as shown in Table 2.1.

Clearly, given any set of nodes, there is no unique tetrahedralisation (unless

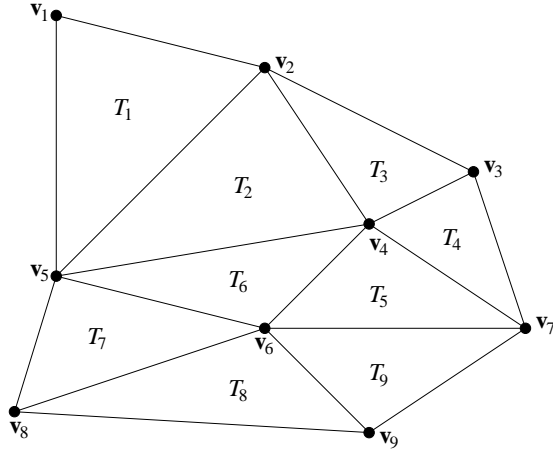


Figure 2.2: An example of a triangulation.

| Triangle | Vertices | Triangle | Vertices |
|----------|-----------------|----------|-----------------|
| T_1 | v_1, v_2, v_5 | T_6 | v_4, v_6, v_5 |
| T_2 | v_2, v_4, v_5 | T_7 | v_5, v_6, v_8 |
| T_3 | v_2, v_3, v_4 | T_8 | v_6, v_9, v_8 |
| T_4 | v_3, v_7, v_4 | T_9 | v_6, v_7, v_9 |
| T_5 | v_4, v_7, v_6 | | |

Table 2.1: Triangulation data for the triangulation in Figure 2.2.

there are exactly 4 nodes in total). Even for a small number of nodes the task of creating a tetrahedralisation by hand is almost impossible, particularly if one wishes to impose certain *conformity* conditions on the final mesh such as keeping all tetrahedra as close to the same shape as possible. What is needed is an algorithm which can be implemented on computer to generate a mesh.

The most popular method of tetrahedralisation is the Delaunay tetrahedralisation (or triangulation in R^3). This has three important properties: given any set of nodes the Delaunay tetrahedralisation is almost always unique⁷, the size of any given tetrahedron inversely reflects the nodal density, and it satisfies the maximum-minimal angle property⁸ [50]. The second property enables the

⁷If a set of nodes produces non unique Delaunay tetrahedralisations then it is common practice to perturb the nodes and recalculate the tetrahedralisation. Note that non unique Delaunay tetrahedralisations may only occur if any five nodes are cospherical, ie. lie on the same sphere.

⁸Considering triangulations, suppose N is a set of n nodes in R^2 and $\mathcal{T}(N)$ is the set of all possible triangulations of N . Let T be a particular triangulation in $\mathcal{T}(N)$, and denote the minimum angle of triangle j in T by $\theta_{\min j}$. Let $m(T) = \frac{1}{n} \sum_{j=1}^n \theta_{\min j}$ be the average of the minimum angles in T , in particular let $m(D)$ be the average minimum angle of the Delaunay triangulation of N . Then $m(D) = \max \{m(T) : T \in \mathcal{T}(N)\}$. This is known as the maximum-

construction of meshes which are coarse in some regions and fine in others simply by varying the nodal density, allowing for highly irregular tetrahedralisations.

For a tetrahedral parameterisation it is convenient, for simplicity, to use basis functions which are constant in a given cell, such as setting $f_j = 1$ in equation 2.10. This assumes, however, that continuity is not required in the function, which in this case is δs . A discontinuous Earth model is unrealistic, and if continuity is required within a cell it becomes more constructive to define basis functions per node rather than per cell. An example of such a basis function is

$$e_j(\mathbf{r}) = \begin{cases} \frac{(\mathbf{r}-\mathbf{v}_{j_1}) \cdot ((\mathbf{v}_{j_2}-\mathbf{v}_{j_1}) \times (\mathbf{v}_{j_3}-\mathbf{v}_{j_1}))}{(\mathbf{v}_j-\mathbf{v}_{j_1}) \cdot ((\mathbf{v}_{j_2}-\mathbf{v}_{j_1}) \times (\mathbf{v}_{j_3}-\mathbf{v}_{j_1}))} & \mathbf{r} \in \text{cell containing } \mathbf{v}_j \\ 0 & \text{otherwise} \end{cases}$$

where \mathbf{v}_j is node j and $\{\mathbf{v}_j, \mathbf{v}_{j_1}, \mathbf{v}_{j_2}, \mathbf{v}_{j_3}\}$ are the vertices of the tetrahedron containing \mathbf{r} [51]. Note that this will produce discontinuity across adjacent tetrahedra. Other basis functions can be used to achieve a higher degree of smoothness, such as the natural neighbour basis functions presented by Sambridge *et al.* [50].

2.2.3 Spherical Harmonics

A block parameterisation is usually adequate in studying variations in the Earth which are relatively localised. For large scale variations it becomes more appropriate to use a spherical harmonics expansion of the slowness perturbation such as

$$\delta s = \sum_{i=0}^I \sum_{j=0}^J \sum_{k=-j}^j c_{ijk} f_i(r) P_{jk}(\cos \theta) e^{ik\theta} \quad (2.11)$$

where P_{jk} denotes the associated Legendre polynomial of degree j and order k , and f_i is usually a polynomial function. This results in $(K+1) \sum_{m=1}^{L+1} (2m-1)$ unknown coefficients. Typically f_i will be a Legendre or Chebyshev polynomial of degree i , see Appendix A.2 for definitions of these polynomials. One can view the spherical harmonics approach as an extension of the spherically symmetric models $v = v(r)$ by including polynomial terms in longitude and latitude. If the spherically symmetric models are seen as “average” models, then the application of spherical harmonics are seen to “better” these averages by incorporating systematic variations into the models [39].

The model δs , from equation 2.7, can be expressed to arbitrary accuracy by setting I and J as large as is necessary, even infinity, but practical computing minimum angle property. In a sense this ensures that the Delaunay triangulation has the least number of long and thin triangles, a property which carries over into R^3 .

requirements dictate they be finite. Since each integral

$$\int_{\Gamma_{0i}} f_i(r) P_{jk}(\cos \theta) e^{ik\theta} \, dl$$

must be calculated manually the computations can be time consuming, meaning I and J should be small. In fact, Dziewonski [17] used value of $I = 4$ and $J = 6$, resulting in 245 unknowns as opposed to 291,600 as used by Widjiantoro [55], and was able to achieve a stable solution for a lower mantle model which depicted long wavelength variations.

Arguments for using a spherical harmonic parameterisation are that it requires fewer parameters than a block parameterisation to result in the same level of visual smoothness in a model, and a harmonic velocity model can be directly compared with other harmonic models depicting gravitational and magnetic fields [29].

Chapter 3

Self-adaptive Parameterisations

Tetrahedral meshes were discussed in section 2.2.2 as an alternative to the conventional spherical harmonic and spherical grid parameterisations. One of the major difficulties of both these parameterisations is that arbitrary local refinement is difficult without refining the entire parameterisation. This is the scope in which tetrahedral meshes have a distinct advantage. They enable cells of varying sizes to be distributed according to the required resolution of regions within the Earth. For example, Sambridge and Gudmundsson [51] demonstrate the use of irregularly sized tetrahedra to characterise tectonic boundaries and continental regions, thus introducing resolution only where it is desired.

The aim of this chapter is to discuss a technique, new to seismic tomography, which will self-adapt a given mesh. Mesh refinement and grid adaptation has played a big part in modern numerical modeling, such as computational fluid dynamics and engineering problems, but it has only recently been employed in seismic tomography [37]. The use of tetrahedral meshes in geophysical problems is also quite recent, such as Constable *et al.* [11].

Section 3.1 will present the data used and standard computational methods employed. It will also detail the parameterisations to be used as a starting point for further refinement. Section 3.2 will discuss various options for cell subdivision and present the results of using the bisection method for standard P wave travel-time tomography. These results are analysed and comparison is made with the *P-Nature97* P wave velocity model by Widiyantoro [55, 58].

3.1 Data and computational methods

3.1.1 The Data

P wave residuals from the EHB-96 data set were used in this study. This set comprises event relocation and phase reidentification, by Engdahl, Van der Hilst and Buland in 1996, of ISC¹ and NEIC² data from 1964 to 1995. The travel-time residuals are with respect to the *ak135* model [33], a one dimensional reference model $v = v(r)$. Summary rays³ derived from this set, for the direct *P* phases only, totalled 549,046, which corresponds to 77,863 events recorded at a subset of 3,750 stations, distributed irregularly worldwide. Global positioning of the data is depicted in Figures 3.1(a) and 3.1(b) respectively.

Filters were then applied to the summary rays. These eliminated rays for which:

1. The residual was greater than 5 s,
2. The angle between the epicentre and receiving stations was greater than 95°,
3. There were fewer than 20 observations for the event,
4. The precision of the arrival time was less than 1 s.

Filter 1 ensures there are no outliers in the data so that the distribution in traveltimes can be approximated by a Gaussian distribution. Rays which bottom in the core are eliminated with filter 2. Filters 3 and 4 dismiss data for which the errors in earthquake location and arrival times, respectively, were significant.

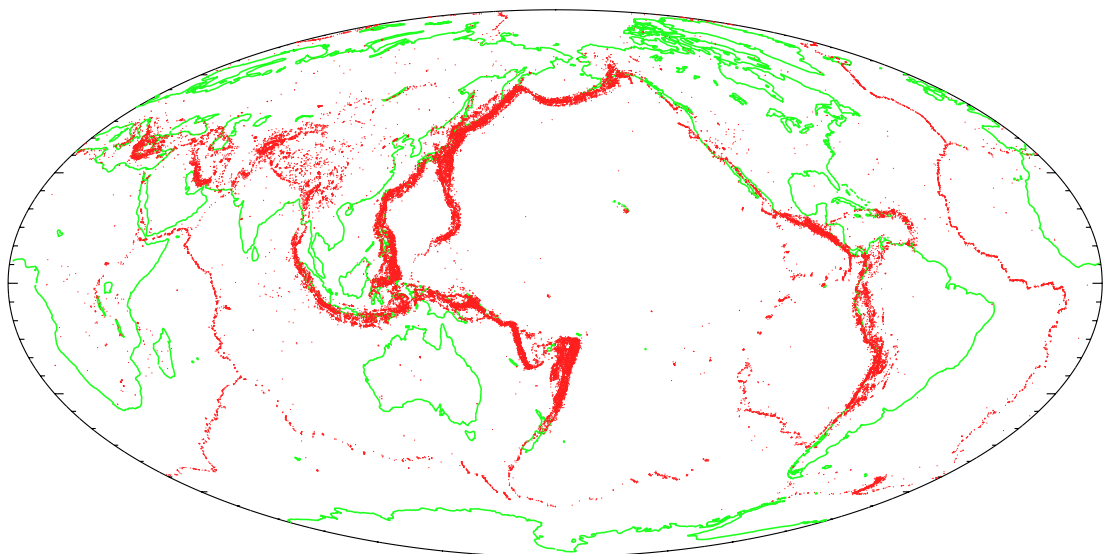
3.1.2 Parameterisations

As a starting point for mesh refinement a “regular” parameterisation is required, ie. uniformly distributed cells which are approximately the same size. There are two feasible options for this: Cartesian or tetrahedral cells. To facilitate the local refinement of a Cartesian grid, it would have to be stored in a similar way to a tetrahedral mesh as list of vertices for each cell, with the addition that the edges also need to be stored. However, each cube has eight vertices and six adjacent cells (as opposed to four vertices and four adjacent cells for a tetrahedron), so

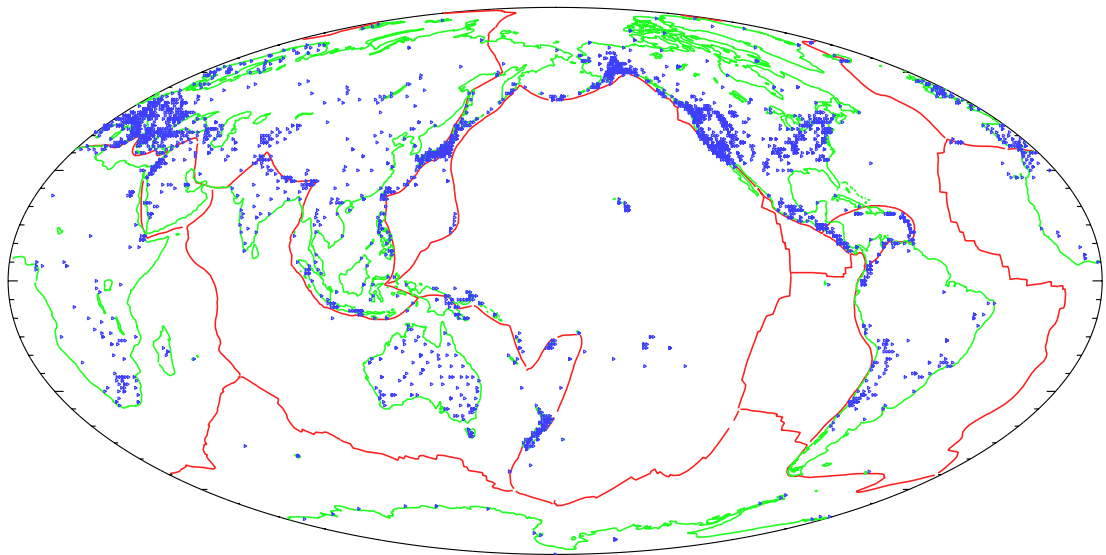
¹International Seismological Centre.

²National Earthquake Information Center.

³A summary ray is constructed as an “average” of nearby rays. This construction alleviates some of the error due to earthquake mislocation, arrival time readings and phase identifications, but in doing so tends to make residuals insensitive to structure at the hypocentre.



(a) Epicentres of the event data.



(b) Recording stations.

Figure 3.1: Geographical positions of the data used.

computationally it becomes more efficient to use a tetrahedral mesh. The primary reason for using tetrahedra rather than cubes, or any other shape, is that the data structure⁴, refinement process, and navigation tools⁵ are well established for tetrahedra.

Delaunay tetrahedralisation was chosen over other methods as the algorithms for modeled computing such meshes are more reliable and more commonly available. The method used to compute the Delaunay tetrahedralisation (and triangulations, for initial parameterisation creation) was the *quickhull* algorithm of Barber, Dobkin and Huhdanpaa [2], using the *Qhull* software available from the Geometry Centre [21]. Images displayed⁶ in this section were created with *Geomview*, also from the Geometry Centre.

The initial parameterisation was built from the surface triangulation of the icosahedron, shown in Figure 3.2. This was used as a starting point as it has the most number of faces of all five regular polyhedra⁷. It is a crude parameterisation

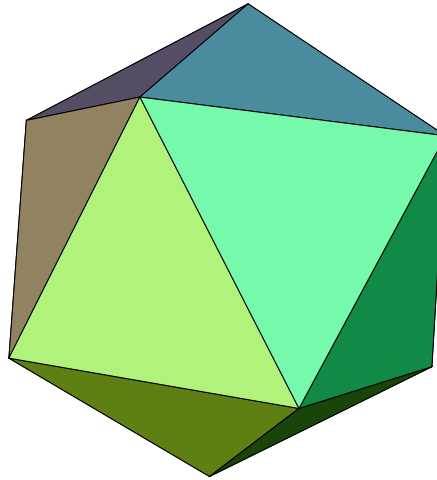


Figure 3.2: The icosahedron.

of the surface of a sphere, as all vertices lie on the same spherical shell. If this were to represent the exterior face of a parameterisation of the Earth, then the mid-point of any of the triangular faces would be about 1,300 km below the surface of the Earth. This is a limitation of the parameterisation since it would mean that a large outer portion of the Earth is not included in the parameterisation and therefore cannot be . There are two solutions: the size of the icosahedron

⁴This refers to the way in which the parameterisation is stored. For tetrahedra it is simply a list of nodes, but for other polyhedral meshes one must also store edges.

⁵Given a point x , it is necessary to compute which cell it lies in. This is simple for any regular grid, but sophisticated algorithms are required for polyhedral meshes.

⁶Surface parameterisation images only.

⁷The five regular polyhedra, called the Platonic solids, are the tetrahedron, cube, octahedron, dodecahedron and icosahedron.

can be increased until the Earth lies wholly inside it, or the surface triangles could be transformed into spherical triangles. The problem with the first option is that the opposite effect will occur, there will be large portions of space in the parameterisation which lies outside the Earth. Throughout this study the second option was used.

I will label the icosahedral shell as *shell0*. In order to get a depth parameterisation of the Earth, as well as the surface, this shell was reproduced at several depth layers within the Earth, and the resulting sequence of nodes was used as the basis of a Delaunay tetrahedralisation (a single point was also placed at the center of the sphere to improve the conformity of the resulting mesh). The depth layers chosen were the same as those used by Widiyantoro [58], and are shown in Table 3.1, where S_n is the n^{th} spherical shell (with $n = 0, 2, \dots, 18$).

| Surface | Depth (km) | Surface | Depth (km) |
|---------|------------|----------|------------|
| S_0 | 0 | S_{10} | 1400 |
| S_1 | 100 | S_{11} | 1600 |
| S_2 | 200 | S_{12} | 1800 |
| S_3 | 300 | S_{13} | 2000 |
| S_4 | 410 | S_{14} | 2200 |
| S_5 | 520 | S_{15} | 2400 |
| S_6 | 660 | S_{16} | 2600 |
| S_7 | 820 | S_{17} | 2750 |
| S_8 | 1000 | S_{18} | 2889 |
| S_9 | 1200 | | |

Table 3.1: Depth intervals used in this study.

Using these depth layers the first interval will be 100 km thick. However, the mid-points of the outer tetrahedra are 1300 km below the surface. This makes the outermost layer about 1000 km thicker than layers beneath. To try and overcome this discrepancy *shell0* has been refined in the following way to produce smaller surface triangles. Firstly, new points are added at the midpoint between any two connected vertices. Then these points are projected onto the surface of the spherical shell, creating a better approximation of a sphere [11, 57]. This process is demonstrated in Figure 3.3. The resulting object I will label *shell1*, Figure 3.4(a). This process may be repeated several times, going up to *shell4*. The next refinement, *shell5*, was also produced, but computational instabilities made the calculation of the corresponding tetrahedral mesh not possible. The resulting surface parameterisations are shown in Figure 3.4. Of these, only the icosahedron (Figure 3.2) is truly regular. However, I will also call these objects

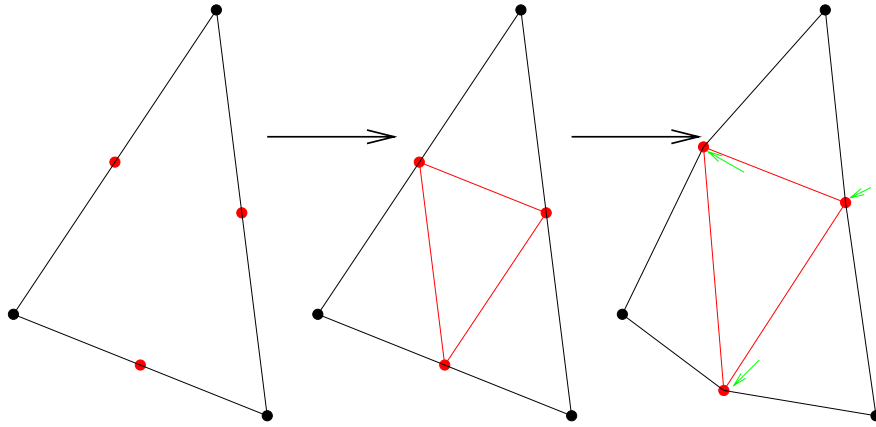


Figure 3.3: Three step refinement of a surface triangle on the icosahedron.

regular, as they are not biased in any way and provide an approximately even distribution of cells.

Clearly, in generating the tetrahedralisation from each surface subdivision, using the depth intervals in Table 3.1, the cell volume decreases with depth. In order to partly alleviate this problem, the mesh generated by $shell(n)$ (for $n \geq 1$) has the deepest five shells replaced by the shells generated by $shell(n-1)$. For

| surface | subdivision | cell length | surface | subdivision | cell length |
|----------------|---------------|-------------|-----------------|---------------|-------------|
| S ₀ | <i>shell3</i> | 500 km | S ₁₀ | <i>shell3</i> | 390 km |
| S ₁ | <i>shell3</i> | 492 km | S ₁₁ | <i>shell3</i> | 375 km |
| S ₂ | <i>shell3</i> | 484 km | S ₁₂ | <i>shell3</i> | 359 km |
| S ₃ | <i>shell3</i> | 477 km | S ₁₃ | <i>shell3</i> | 343 km |
| S ₄ | <i>shell3</i> | 468 km | S ₁₄ | <i>shell2</i> | 655 km |
| S ₅ | <i>shell3</i> | 460 km | S ₁₅ | <i>shell2</i> | 624 km |
| S ₆ | <i>shell3</i> | 449 km | S ₁₆ | <i>shell2</i> | 592 km |
| S ₇ | <i>shell3</i> | 436 km | S ₁₇ | <i>shell2</i> | 569 km |
| S ₈ | <i>shell3</i> | 422 km | S ₁₈ | <i>shell2</i> | 547 km |
| S ₉ | <i>shell3</i> | 406 km | | | |

Table 3.2: Depth structure for the mesh generated by *shell3*.

example, the tetrahedralisation produced by *shell3* the appropriate shells are tabulated in Table 3.2 together with the order of magnitude of the average cell side length. The newly defined parameterisations will be denoted *param*(n).0.

In two dimensions, such a construct will look like Figure 3.5(a). This is an estimation of what a cross section of a complete parameterisation, using *param3.0*, may look like. Note the large cells at the interface between one refinement level and the next. This type of cell structure comes about from the strict regularity (symmetry) of the point distribution. In an attempt to reduce the occurrence

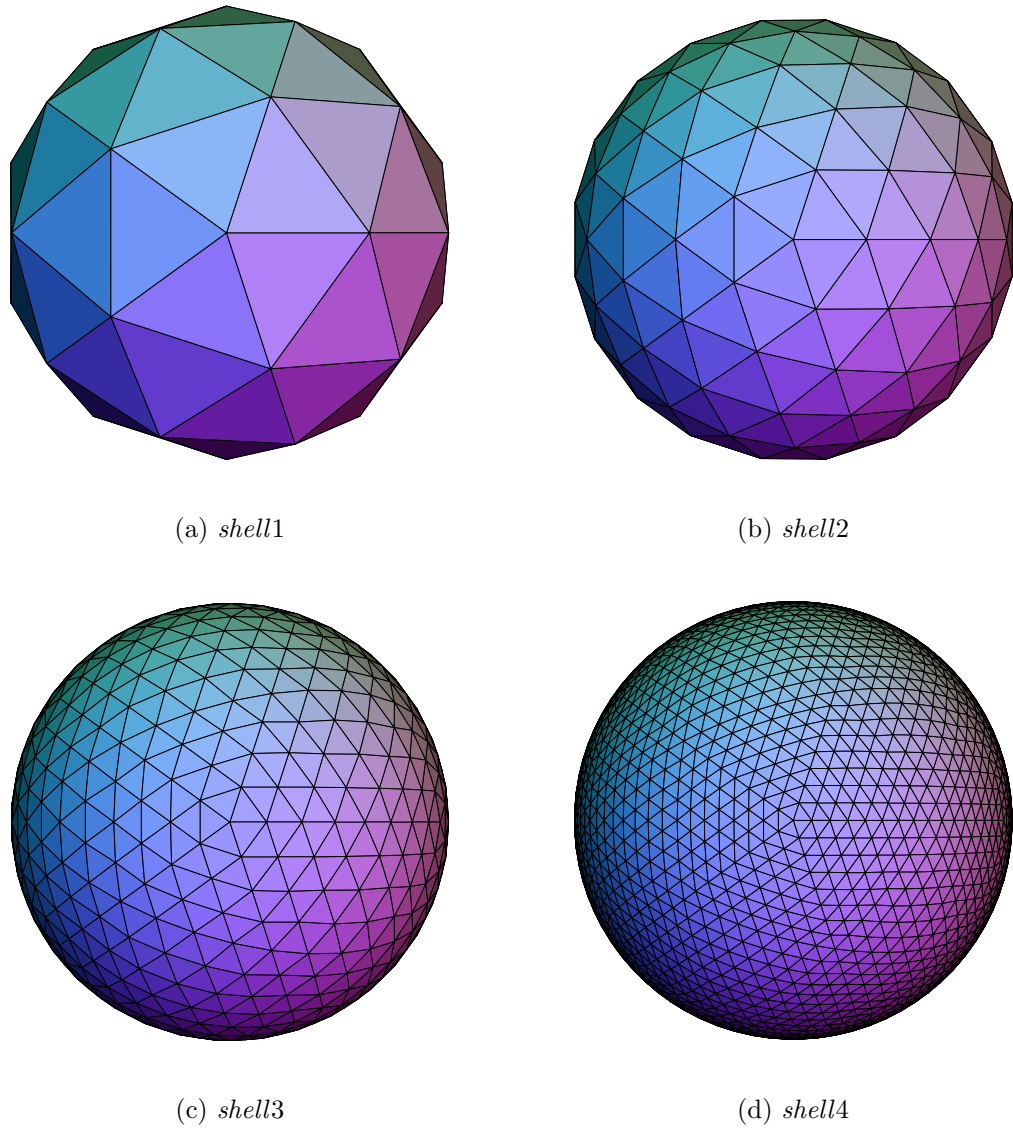


Figure 3.4: Refinements of the icosahedron.

of this feature all nodes (in the three dimensional parameterisation) have been perturbed randomly between ± 1 km. This also increases mesh conformity when using the *quickhull* algorithm since regularly spaced points are prone to producing planar point sets which produce degenerate tetrahedralisations. It is believed that the creation of these large cells is mostly a two dimensional effect, but visualising such an object in three dimensions is difficult. However, if such a feature was to be produced in a three dimensional mesh, it would be quickly absorbed by the irregular refinement process to be applied based on spatial gradients (section 3.2.1). It is interesting to note that when approximating a cross section of the parameterisation *param4.0* this effect disappears completely, as shown in Figure 3.5(b); which may be due to the increase in nodal density.

One of the aims of this project is to discuss the suitability of each parame-

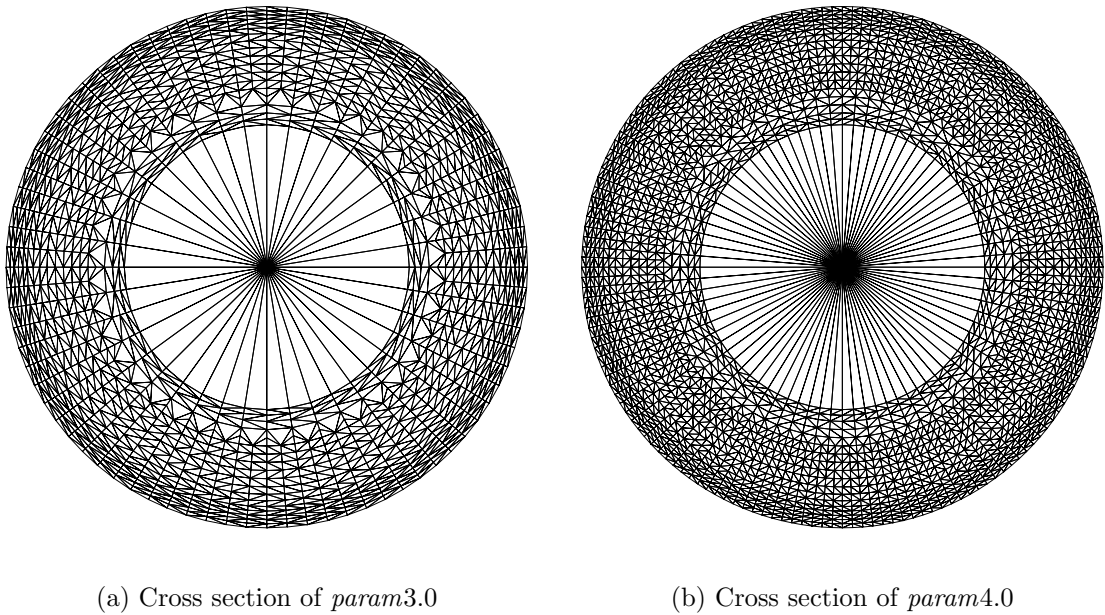


Figure 3.5: Estimation of the cross section of a parameterisation.

terisation for seismic tomography by examining the results of irregularly subdividing each mesh further. This suitability, and the quality of the results, is to be weighed up against the difference in the number of cells in each parameterisation. Table 3.3 shows data for these “regular” parameterisations: \mathcal{S}_s and \mathcal{T}_s are the number of points and number of triangles on the generating surface ($shell(n)$), $npoints$ is the total number of points in the generated parameterisation and $ncell$ is the total number of cells. Δr is an estimation of the distance from the centre of any given surface triangle to the surface of the Earth and *P-Nature97* denotes the parameterisation used by Widjiantoro in [58] and [55]. The parameterisation

| subdivision | \mathcal{S}_s | \mathcal{T}_s | $npoints$ | $ncell$ | Δr |
|-------------------|-----------------|-----------------|-----------|---------|------------|
| <i>param0.0</i> | 12 | 20 | 229 | 1,315 | 1,308 km |
| <i>param1.0</i> | 42 | 80 | 649 | 4,056 | 419 km |
| <i>param2.0</i> | 162 | 320 | 2,479 | 16,189 | 91 km |
| <i>param3.0</i> | 642 | 1,280 | 9,799 | 64,973 | 27 km |
| <i>param4.0</i> | 2,562 | 5,120 | 39,079 | 259,418 | 6 km |
| <i>P-Nature97</i> | 16,200 | 16,200 | 307,800 | 291,600 | 0 km |

Table 3.3: Number of points and cells for different parameterisations.

generated by *shell0* was not used for modeling as it was perceived to be far too coarse, and too limited an approximation of the Earth to be useful.

Orthonormal basis functions were used, $e_j = V_j^{-\frac{1}{2}}$. The volume of a tetrahe-

dron is given by $V = \frac{1}{6} |\mathbf{w}_1 \cdot (\mathbf{w}_2 \times \mathbf{w}_3)|$, where $\{\mathbf{w}_1, \mathbf{w}_2, \mathbf{w}_3\}$ are defined as

$$\mathbf{w}_1 = \mathbf{r}_1 - \mathbf{r}_4$$

$$\mathbf{w}_2 = \mathbf{r}_2 - \mathbf{r}_4$$

$$\mathbf{w}_3 = \mathbf{r}_3 - \mathbf{r}_4,$$

$\{\mathbf{r}_i\}_{i=1}^4$ are the vertices of the tetrahedron.

3.1.3 Calculating the Fréchet Derivatives

In order to find the elements of the Fréchet derivative matrix, A_{ij} from equation 2.8, the calculation of the integrals $\int_{\Gamma_{0i}} e_j \, dl$ was required. The reference model used *ak135*, which was derived by Kennett *et al.* [33], is a spherically symmetric model (ie. it depends upon r only) and is depicted graphically in Figure 3.6.

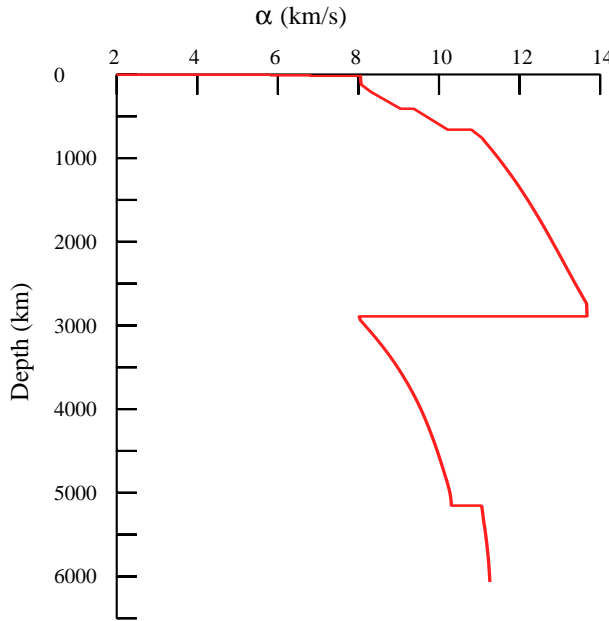


Figure 3.6: The reference model, *ak135*.

Note that

$$\begin{aligned} \int_{\Gamma_{0i}} e_j \, dl &= V_j^{-\frac{1}{2}} \int_{\Gamma_{0i}} \, dl \\ &= V_j^{-\frac{1}{2}} l_j \end{aligned}$$

setting l_j to be the length of the ray in tetrahedron j . The calculation of the l_j was as follows. The ray was sampled at 10 km depth intervals (1 km close to the bottoming point of the ray where it propagates almost horizontally). Given a point along the ray \mathbf{r}_1 with radius r_1 and velocity v_1 , given by *ak135*, it is

necessary to determine the next point along the ray so as to determine the cells through which the ray travels. Suppose the next point is \mathbf{r}_2 which has radius r_2 , then the velocity with respect to $ak135$, v_2 , can be immediately determined. The Mohorovičić law, $v = ar^b$, is used as an interpolation scheme between the two points to allow the angle subtended at the centre of the Earth, Δ , to be calculated using equation 1.17⁸. The constants a and b are easily determined from the values v_1 and v_2 . Then, knowing \mathbf{r}_1 , r_2 and Δ the next point \mathbf{r}_2 can be given. See Figure 3.7 for an example of stepping along a ray through a Delaunay triangulation.

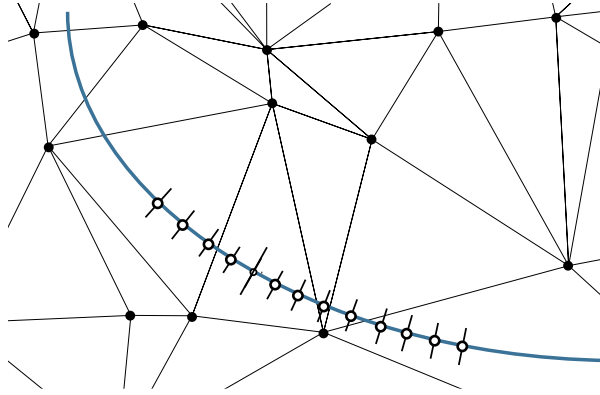


Figure 3.7: Stepping along a ray path in a Delaunay triangulation.

The length of the ray between the two points \mathbf{r}_1 and \mathbf{r}_2 was then just taken to be the difference $\|\mathbf{r}_2 - \mathbf{r}_1\|$. If both points lie in cell j then this length is simply added to the total ray length in that cell. However, if one of these points lies inside cell j and the other lies in cell $k \neq j$, then half of this length is added to the total length of the ray in cell j , and half to the total length in cell k .

The method of determining if a point lies in a given cell was that described in Sambridge and Gudmundsson [51]. Using this algorithm in a ray tracing routine increases the computation time by no more than 25% of similar routines using a Cartesian grid.

Ray tracing was performed by starting at the recording station and tracing to the hypocentre. This makes sure that the position of the station is not missed, which may occur when tracing in the opposite direction as the location of the hypocentre is never precisely known.

⁸The ray parameter p is also needed in this calculation, and it has been provided in the data set.

3.1.4 Matrix Techniques

To solve for the coefficients in equation 2.9 a least squares approach is taken. That is, we wish to solve the following

$$\min \|A\mathbf{c} - \delta\mathbf{T}\|^2 \quad (3.1)$$

using the Euclidean norm. Other norms can be used, replacing equation 3.1 by $\min \|A\mathbf{c} - \delta\mathbf{T}\|^p$ where $p \geq 1$, but for large systems the computations become much less efficient than using the Euclidean norm.

Differentiating 3.1 with respect to \mathbf{c} and setting the result to zero gives the normal equations

$$A^T A\mathbf{c} = A^T \delta\mathbf{T}. \quad (3.2)$$

In many seismic tomographic problems A will be sparse and non-square, often leading to a large range in eigenvalues of $A^T A$, of the order $\sim 10^5$. The smaller eigenvalues are then effectively zero, leading to non-unique solutions of 3.2.

Several methods are available to try and overcome this problem, see [56]. The methods employed here are

1. minimum norm,
2. gradient damping.

Both methods entail adding extra equations to $\delta\mathbf{T} = A\mathbf{c}$. In the case of minimum norm we add $d_1 I_{ncell}\mathbf{c} = \mathbf{0}$ to the system, where d_1 is a constant and I_{ncell} is the identity matrix with rank equal to the number of cells ($ncell$) in the parameterisation. This alters condition 3.1 to become

$$\min \left\| (A\mathbf{c} - \delta\mathbf{T})^T (A\mathbf{c} - \delta\mathbf{T}) + d_1^2 \mathbf{c}^T \mathbf{c} \right\| \quad (3.3)$$

which has the effect of biasing towards a model which has zero slowness perturbation with respect to the reference model, *ak135*.

The gradient damping method, used to produce a more realistic smooth model, minimises the gradient between the value of a given cell with each of its neighbours — a first order smoothing effect described by

$$\min \sum_i \sum_{n_i} (c_i - c_{n_i})^2, \quad (3.4)$$

where $i = 1, \dots, ncell$ and n_i is the index of the n^{th} cell neighbouring cell i . For example, Widiyantoro [58] uses the definition that the neighbouring cells for cell i are those cells which share any number of nodes with cell i . So, for a Cartesian

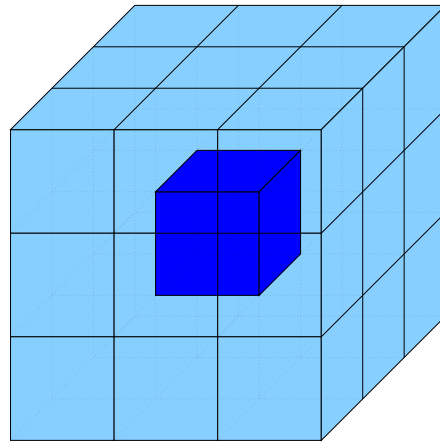


Figure 3.8: Example of a definition for cell neighbours.

grid parameterisation this can be depicted as in Figure 3.8, where each cell (apart from those on the surface of the Earth) has 26 neighbours. Unfortunately, this definition is not as easy to implement in a tetrahedral parameterisation as any cell may have, realistically, anywhere between 10 and 100 neighbours. In this study, rather than construct new codes to perform this task, computer codes already in existence have been used which utilise a more appropriate definition of cell neighbour — any cell which shares a *face* with cell i . A cell in a Cartesian grid will then have 6 neighbours, as shown in Figure 3.9(a). The analogue in a tetrahedral mesh is depicted in Figure 3.9(b). Note that a tetrahedron can have a maximum of four neighbours. This fact is important as it means that models calculated using

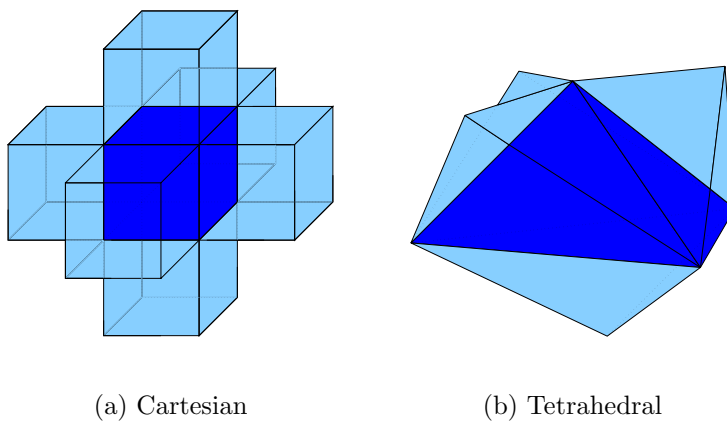


Figure 3.9: Defining cell neighbours used in this study.

a tetrahedral parameterisation will be overall much less smooth than models, utilising a Cartesian-like cell structure (such as Widjiantoro's spherical grid in Figure 2.1 [58]), smoothed over neighbours as per the first definition.

Minimising 3.4 with respect to c_k , by taking the derivative and setting the

result to zero, gives, after some algebra

$$c_k - \left(1 + \sum_{n_k} \frac{1}{N_{n_k}}\right)^{-1} \sum_{n_k} \left(\frac{1}{N_k} + \frac{1}{N_{n_k}}\right) = 0, \quad (3.5)$$

setting N_k to be the number of neighbouring cells for cell k , and N_{n_k} to be the number of neighbouring cell for cell n_k . This generates an auxiliary set of equations given by $d_2 C \mathbf{c} = \mathbf{0}$, d_2 is a constant and the $ncell \times ncell$ matrix C is given by

$$C_{ij} = \begin{cases} -1 & j = i, \\ \left(1 + \sum_{n_i} \frac{1}{N_{n_i}}\right)^{-1} \sum_{n_i} \left(\frac{1}{N_i} + \frac{1}{N_{n_i}}\right) & j = n_i, \\ 0 & \text{otherwise.} \end{cases}$$

Implementing both minimum norm and conjugate gradient smoothing transforms equation 2.9 into

$$M\mathbf{c} = \mathbf{q}, \quad (3.6)$$

where

$$M = \begin{pmatrix} A \\ d_1 I_{ncell} \\ d_2 C \end{pmatrix} \quad \text{and} \quad \mathbf{q} = \begin{pmatrix} \delta \mathbf{T} \\ \mathbf{0} \\ \mathbf{0} \end{pmatrix}.$$

The constants d_1 and d_2 are adjusted manually to vary the weight given to the two regularising terms relative to the data equation.

As with most large least squares problems, this one is solved iteratively. This method involves taking an initial “guess” (usually a combination of \mathbf{q} and M) of the solution, \mathbf{c}_0 , and calculating the difference $\mathbf{r}_0 = \mathbf{q} - M\mathbf{c}_0$. This information is then used to better the estimate of the solution to $\mathbf{c}_1 = \mathbf{c}_0 + f(\mathbf{r}_0)$ where f is an error estimate function [43]. If this is repeated x times then the x^{th} estimate will be $\mathbf{c}_x = \mathbf{c}_{x-1} + f(\mathbf{r}_{x-1})$. Throughout this study 20 iterations have been performed for each parameterisation, and the iterative solver used was the *LSQR* routine, described in [56, 42].

Recall that the vector \mathbf{c} describes the function δs through $\delta s = c^j e_j$, where each e_j is nonzero only in cell j , where it is equal to $V_j^{-\frac{1}{2}}$. So, to recover the velocity perturbation in cell j from the value c^j we firstly let $\delta s_j = V_j^{-\frac{1}{2}} c_j$, which is the slowness perturbation in cell j . Now, $\delta v_i \approx v_j - v_0$, where v_0 is the reference

model value for the velocity in cell j , and $v_j = s_j^{-1}$, so

$$\begin{aligned}\delta v_j &\approx v_j - v_0 \\ &= s_j^{-1} - v_0 \\ &\approx (s_0 + \delta s_j)^{-1} - v_0 \\ &= (v_0^{-1} + \delta s_j)^{-1} - v_0.\end{aligned}$$

The key indicators used for determining model reliability are the convergence of the solution upon successive iterations, and the variance reduction. Convergence is measured in terms of the length of the vector $\mathbf{q} - M\mathbf{c}_x$, typically a ratio with $\|\mathbf{q}\|$, ie.

$$\frac{\|\mathbf{q} - M\mathbf{c}_x\|}{\|\mathbf{q}\|}.$$

If we multiply the denominator and numerator by $\frac{1}{\sqrt{w}}$, where w is equal to the number of datum plus $2 \times n_{cell}$, then this fraction can be rewritten in term of the root mean squared (RMS) of each vector

$$\begin{aligned}\frac{\|\mathbf{q} - M\mathbf{c}_x\|}{\|\mathbf{q}\|} &= \frac{\frac{1}{\sqrt{w}} \|\mathbf{q} - M\mathbf{c}_x\|}{\frac{1}{\sqrt{w}} \|\mathbf{q}\|} \\ &= \frac{\sqrt{\frac{\|\mathbf{q} - M\mathbf{c}_x\|^2}{w}}}{\sqrt{\frac{\|\mathbf{q}\|^2}{w}}} \\ &= \frac{\text{RMS}(\mathbf{q} - M\mathbf{c}_x)}{\text{RMS}(\mathbf{q})}.\end{aligned}$$

This can be expressed as a percentage, hence shall be referred to as % RMS.

The variance reduction is an estimation of how close, at least in magnitude, the quantity $A\mathbf{c}_f$, where \mathbf{c}_f is the final solution, is from the data vector $\delta\mathbf{T}$. Given any vector \mathbf{y} the variance is defined as $\text{Var}(\mathbf{y}) = (\text{RMS}(\mathbf{y}))^2$, so we can define the variance reduction of the vector \mathbf{c}_f as

$$\begin{aligned}\text{V.R.}(\mathbf{c}_f) &= 1 - \frac{\text{Var}(\delta\mathbf{T} - A\mathbf{c}_f)}{\text{Var}(\delta\mathbf{T})} \\ &= 1 - \frac{\|\delta\mathbf{T} - A\mathbf{c}_f\|^2}{\|\delta\mathbf{T}\|^2}.\end{aligned}$$

This is usually expressed as a percentage, and a high value for the variance reduction ($\sim 50\%$) means the model \mathbf{c}_f recovers the data very well. Typically, in seismic tomographic inversions, the variance reduction lies between 10% and 50%. This value depends on the parameterisation used, the values of the damping

parameters d_1 and d_2 , the number of iterations performed, the data⁹, and whether event relocation has been included in the solution parameters.

Throughout this study, the values of d_1 and d_2 have been set to

$$d_1 = 10^{-10}\ell \quad \text{and} \quad d_2 = 10^{-1}\ell,$$

where ℓ is the average cell side length in the parameterisation. These value were used, after many tests, to try and maximise the variance reduction whilst producing visually appealing models (noting that d_2 effectively smoothes the model).

3.2 Refinement and results

The parameterisations defined in section 3.1.2 were designed to provide an approximately uniform distribution of cells throughout the Earth. However, the Earth itself is not uniform. It is therefore desirable to use a parameterisation which can adequately resolve anomalies within the Earth but at the same time computer memory and speed should be optimised. If one were simply to refine the entire parameterisation to increase the resolution, for example, using *param3.0* as opposed to *param2.0*, then resolution would also be increased in regions of very little structural variation. This would have the undesirable effect of consuming computer memory and time. Another consideration is the scattered nature of the data coverage (see Figure 3.1), which results in many cells not being sampled. To further refine these unsampled cells is a waste of resources, and it would be more desirable to increase resolution where ray densities are high.

This section will present options for refining a given tetrahedral mesh. The results of performing a chosen refinement procedure on the parameterisations *param(n).0*, defined in section 3.1.2, will be presented and analysed.

3.2.1 Parameterisation Refinement

There were two points to consider in refining any mesh. Firstly, the criteria for determining whether or not a cell is subdivided, and secondly the way in which cells are refined. Both considerations have many methods available, some of which will be discussed here as appropriate.

The main options for determining if a cell was to be subdivided were ray-density and gradients in the velocity model resulting from a previous iteration.

⁹Different types of data (P , pP , S , ...) sample the Earth differently and hence provide different coverage of the Earth.

Given any cell, the ray density in that cell can be defined as the number of rays passing through it, or the number of rays per unit volume passing through the cell. It is conceivable that both definitions would produce similar results, particularly when refinement is applied to one of the “regular” tetrahedral parameterisations. The advantage of using ray densities as a criteria for cell subdivision is that refinement will occur based on available data coverage. For example, in the upper mantle a refinement algorithm would produce finer cells in regions of plate subduction and in continental regions, where the stations coverage is greater. However, this feature may be undesirable, particularly if adaptive refinement is sought based on the quality of models and velocity variations rather than an *a priori* data coverage constraint.

A more suitable refinement criteria can be designed based on spatial gradients in the three dimensional velocity model. Here the gradient can be defined in several ways, but in any case it is important to note that mesh refinement would occur where model variations are relatively high thus disregarding the quality and quantity of the available data, and any other factors introduced on bias. It was for this reason that this method was chosen to be implemented in this study, but it is expected that refinement using either method will produce comparable meshes.

The way in which the model “gradient” has been defined, for cell i , is simply

$$\max_{n_i} \frac{|v_{n_i} - v_i|}{\|\mathbf{b}_{n_i} - \mathbf{b}_i\|} \quad (3.7)$$

where n_i is the n^{th} neighbour of cell i , v_i and v_{n_i} are the model values (P wave velocity) of cells i and n_i respectively, and \mathbf{b}_i and \mathbf{b}_{n_i} are the respective tetrahedral centroids¹⁰. This, essentially, picks the maximum gradient through all of the faces of cell i .

Next, the cell refinement technique had to be chosen. The simplest method is to place a single node at the centroid of the tetrahedron in question. When a new Delaunay tetrahedralisation is constructed about the nodes the most likely result is four new tetrahedra replacing the old one, as demonstrated in Figure 3.10(a), which would leave neighbouring tetrahedra untouched. This seems appropriate, but has the undesired consequence that triangles on the surface of the Earth will, most likely, never be subdivided. There are many variations of this approach, one example being to also place new nodes at the centre of each face of the tetrahedron [38], the likely result of recalculating the tetrahedralisation is shown in Figure 3.10(b).

¹⁰Given the four vertices of a tetrahedron, $\{\mathbf{v}_j\}_{j=1}^4$, the centroid is defined as the average $\frac{1}{4} \sum_{j=1}^4 \mathbf{v}_j$.

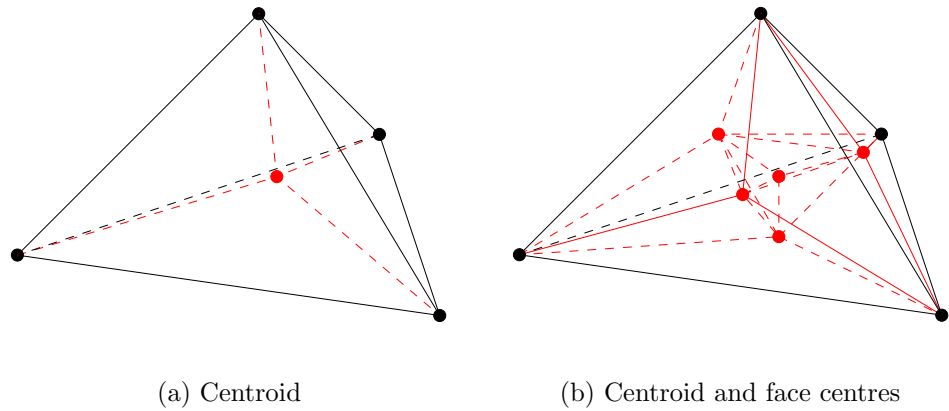


Figure 3.10: Examples for nodal placement.

The most standard mechanism for subdividing tetrahedra is bisection, where a single point is placed at the midsection of each edge [46]. The most likely outcome is the cell will subdivide into eight smaller tetrahedra, as in Figure 3.11, and that each neighbouring tetrahedra will subdivide into four smaller ones. So, upon

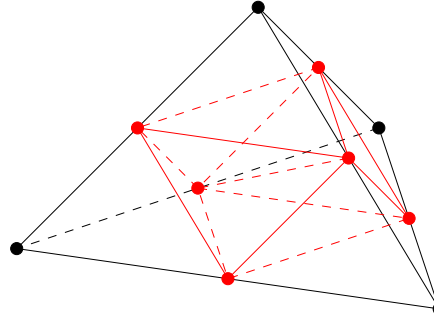


Figure 3.11: Bisection of a tetrahedron.

adding six new points at least twenty-four tetrahedra emerge. This is comparable, in ratio of points added to number of tetrahedra created, to the centroid method above. However, recall that a cell neighbour has been defined as any tetrahedron sharing a face with the given cell. But there are other tetrahedra which share only two nodes, an edge, with the cell in question, and these will also be subdivided. So, bisection produces more refined cells, upon refining a single cell in the mesh, than simply placing a point at the centroid. The advantage bisection has over other methods, such as the variation on centroid placement described above, is that the eight tetrahedra resulting from the subdivided cell are comparable in shape to the original tetrahedron [35], ensuring mesh conformity does not degrade too rapidly upon refinement.

Mesh refinement methods such as those described above enable resolution to be enhanced in regions of interest by adding extra nodes, but does not allow for

the destruction of resolution where it is not required. If “deresolution” is desired there are two methods by which to do so. The simplest is to remove nodes from appropriate regions in the mesh. Again, ray densities and spatial gradients in previous models can be used to determine these regions. Unlike mesh refinement, where the placement of a node largely only effect the tetrahedron being refined, and its neighbours, removing a node affects all tetrahedra which share that node, so caution is required in determining which nodes are to be removed.

The second solution is, rather than adding or removing nodes, to relocate existing node so as to reduce resolution from where it is unwarranted and increase it in regions of interest. The benefit of this method is that there is no increase in the use of resources when modeling under the refined parameterisation. This is a popular method in airflow problems, for example see [4], and has been applied to seismic tomography by Michelini [37] (note that different basis functions are used by Michelini, opting for B-splines¹¹ which are defined at nodal points of the curvilinear grid). However, algorithms for relocating nodes are nonlinear, and since a single node in a tetrahedralisation may be connected, via an edge, to over 20 other nodes in the mesh the relocation process may be computationally expensive.

In this study mesh refinement through bisection was the only method employed for adaptation of the parameterisation.

3.2.2 Plotting

Tetrahedralisations are difficult to visualise, unless one is only concerned with the external faces of the mesh. Because the Earth parameterisations have been subdivided internally, we would like to be able to see the structure of the mesh and resultant models. The method used here to visualise lateral variations is to intersect a spherical shell of radius r with the parameterisation and projecting the cut points onto a map of the Earth (in Mollweide projection). A tetrahedron is said to be “cut” if it has at least one vertex lying inside the intersecting sphere and at least one outside the sphere. The “cut points” are the points in the edges of the tetrahedron where the sphere intersects. These points are found as follows. Suppose two vertices of a tetrahedron \mathbf{r}_1 and \mathbf{r}_2 lie on opposite sides of the intersecting sphere, say $\|\mathbf{r}_1\| < r < \|\mathbf{r}_2\|$, then the cut point will be a vector \mathbf{r}_c such that $\|\mathbf{r}_c\| = r$ and $\mathbf{r}_c = a\mathbf{r}_1 + (1 - a)\mathbf{r}_2$ for some $a \in [0, 1]$. There will be

¹¹Given any spline space a basis can be found of so called B-splines. A B-spline is particularly “nice” as its support is minimal, hence the coefficients of any expansion in B-splines describes local variations [45, pp 95–98].

two solutions for a , but only one of these will lie in the interval $[0, 1]$, the other solution corresponding to a point elsewhere on the intersecting sphere. By noting that $\|a\mathbf{r}_1 + (1 - a)\mathbf{r}_2\|^2 = r^2$, this can be expanded resulting in a quadratic in a , the solutions of which are

$$a = \frac{-(\mathbf{r}_1 - \mathbf{r}_2) \cdot \mathbf{r}_2 \pm \sqrt{((\mathbf{r}_1 - \mathbf{r}_2) \cdot \mathbf{r}_2)^2 - \|\mathbf{r}_1 - \mathbf{r}_2\|^2 (\|\mathbf{r}_2\|^2 - r^2)}}{\|\mathbf{r}_1 - \mathbf{r}_2\|^2}.$$

The cut points are then projected onto the surface of the Earth and connect with new edges, generating a triangle if there are three cut points, and a quadrilateral for four cut points. This method, in vicinity of the tetrahedron, approximates the intersecting sphere to a plane. See Appendix C for examples of such slices. The “streaking” and “outlined triangles” are projection effects which arise from the slicing process.

3.2.3 Presentation and Discussion of Results

Ray tracing was performed on each of the parameterisations $param(n).0$, where $n = 1, 2, 3, 4$, and the matrix methods of section 3.1.4 were used to estimate P wave velocity perturbation models of the mantle. Each parameterisation was then refined based on spatial gradients in the models. The refined parameterisations are labeled as $param(n).x$, where n is the level of initial parameterisation (1, 2, 3 or 4) and x refers to the refinement level ($x = 1$ for the first refinement of $x = 0$, and $x = 2$ is the further refinement of $x = 1$, etc.). The velocity perturbation models resulting from using $param(n).x$ will also be referred to as $param(n).x$ for convenience.

The number of cells subdivided at each refinement step was set to 5% of the number of cells in the current parameterisation. This produced, upon tetrahedralisation of the new nodes, approximately double the number of cells as previously. Also, an upper limit of 500,000 cells was imposed on the parameterisations, hence $param4.0$ was only refined once (to $param4.1$). Despite the fact that the cell subdivision method, bisection, was chosen to ensure mesh conformity did not degrade too much during mesh refinement, subdivisions could not proceed beyond $x = 3$ due to computational instabilities in the *Qhull* program for generating tetrahedralisations. Other refinement techniques, such as centroid placement, may enable the parameterisation adaptation process to continue further.

Figures B.1(a) through B.1(d) (Appendix B.2) depict the % RMS, the convergence indicator, for each parameterisation. A solution is said to converge, upon subsequent iterations of the *LSQR* routine, if the % RMS converges. Clearly, it is desirable for the % RMS to not only converge, but to do so quickly so as

to limit the total number of iterations needed to obtain a stable solution. Also, lower values of % RMS imply a better fit with the data.

Each of the figures show that the difference in % RMS between $\text{param}(n).0$ and $\text{param}(n).1$ is the largest difference. Another observation is that, given n , convergence is slower for the more refined parameterisations, ie. the slope of the graph has larger magnitude. However, the refined models seem to be converging to a smaller value of % RMS which, if iterations are continued, will produce a better fitting, more stable model. Also, note that the solutions using the series of parameterisations $\text{param}1.x$, for $x = 0, 1, 2, 3$, converge notably slower than solutions for the other ten parameterisations.

The most important numerical indicators for the results for these parameterisations are shown in Table B.2 (Appendix B.2): the number of parameters (nodes and tetrahedra) and the variance reduction. These are also depicted in Figures 3.12(a), 3.12(b) and 3.13. The graphs for the number of cells and number of nodes are identical in shape (note the difference in magnitude), clearly showing an increasing exponential dependence, with overlap between the number of parameters for $\text{param}(n).3$ and $\text{param}(n + 1).0$. Conversely, there is no such overlap for the variance reduction. In fact, the shape of the graph, for any of the refinement series $\text{param}(n).x$, as x increases appears almost as the inverse of an exponential curve, ie. a logarithmic curve. Note that the general trend, from $\text{param}1.0$ to $\text{param}4.1$, is again an exponential one. However, it is expected that this trend would not continue much further, since the data would not be able to resolve the fine structure at the scale of the parameterisation.

The “inverse” relationship between the variance reduction and model parameters is not totally unexpected, as the data is only capable of producing a finite resolution, as mentioned above. So, in a sense, the refinements are exhausting the data, at least in the refined regions. This is an important result, as it is desirable to increase the variance reduction, through refinement of the parameterisation, whilst minimising the increase in number of parameters. An important factor in determining the resolving capacity of the data is the sampling regime used in ray tracing. In this study depth intervals of 10 km were used. It is foreseeable that, after several refinements, some of the cells in a mesh will have dimension of the order of 10 km, meaning ray tracing is liable to “skip” the very cells produced in an attempt to enhance the resolution.

Further parameterisation indicators are the average ray density, Figure B.2(a), and average cell size, Figure B.2(b), in Appendix B.2. Ray density here has been defined as the number of rays per cell, rather than the number of rays per unit volume. Although cell volume is a good indicator of cell size, the average side

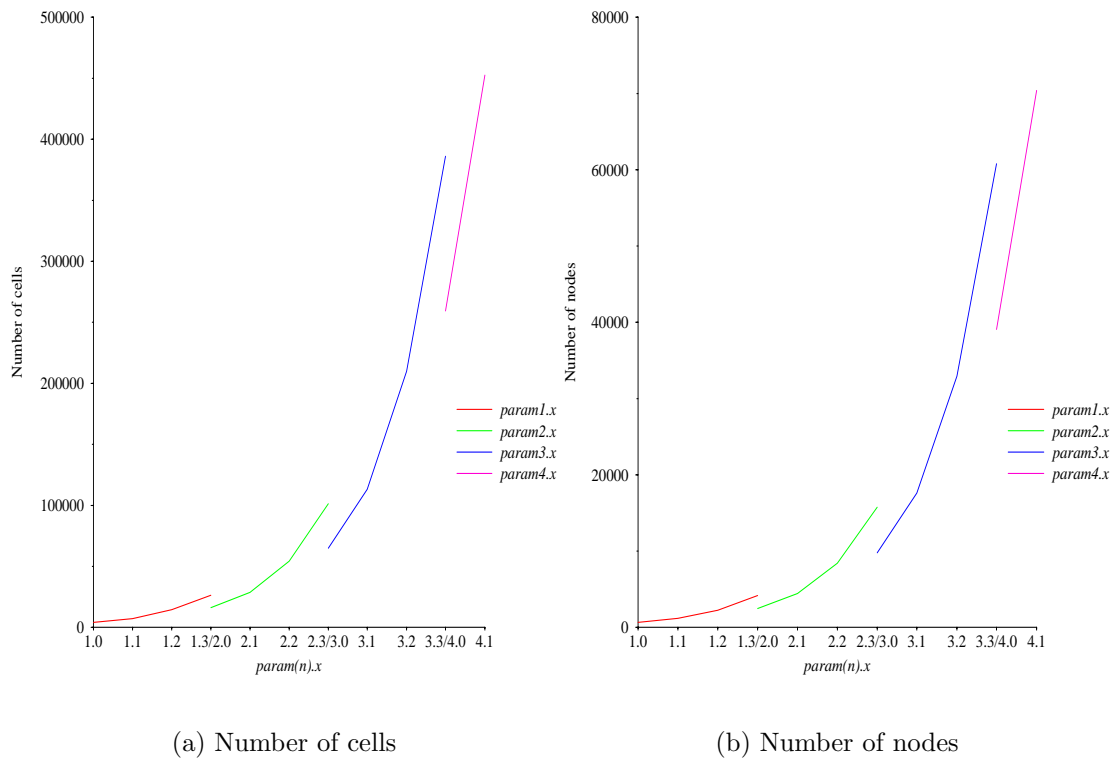


Figure 3.12: Model parameters for each parameterisation.

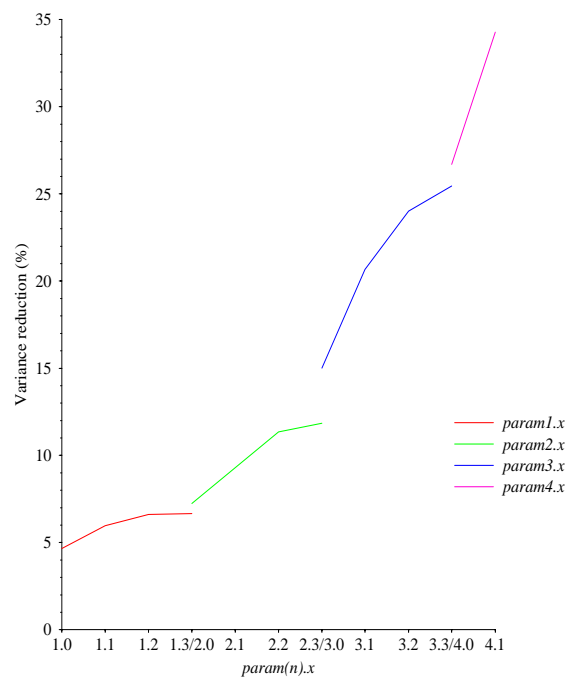


Figure 3.13: Variance reduction for each model.

length is used here. This is done by first calculating the average volume of all cells in a given parameterisation. This volume is then identified with a regular tetrahedron whose side length l is given by the solution to $V = \frac{l^3\sqrt{3}}{16}$. Both ray density and cell width are represented as a percentage of the initial values, for $\text{param}(n).0$, in the figures. All parameterisations show a markable decrease in ray density upon subsequent mesh refinements, whereas the decrease in cell width is not as pronounced.

Slices of the resultant models are given in Appendix C. Two depth slices have been reproduced, 500 km and 1,300 km, for each parameterisation, along with mesh slices for the parameterisations *param1.3*, *param2.3*, *param3.3* and *param4.1*, for the same depths. The perturbations are represented as a percentage of the reference model values (*ak135*), and are clipped at the percentages given in the legends. For each n , the clipping value has been fixed for $\text{param}(n).x$ as x increases to show relative improvements in the model as refinement occurs.

A promising feature of all models is that they depict, approximately, the same structures within the Earth. That is, the refinement process has focussed on the same areas of structural variation for each refinement series. For comparison, the same depth slices for the *P-Nature97* model, by Widjiantoro [55], have been reproduced in Appendix C.5. This model was derived in essential the same way as the models depicted here, and used a spherical grid parameterisation. The notable differences are that this model also included *pP* phases in its derivation, and the matrix inversion included equations for event relocation and performed 50 iterations (rather than 20 performed in this study). The variance reduction was 47%. The following is a description of the notable features of each model.

The crudest model, using *param1.0*, is too crude to be able to deduce any structure. At 500 km there appears to be slow¹² anomalies in the same vicinities as in *P-Nature97*, but structure both at 500 km and 1300 km is too coarse to make identifications with particular anomalies. The refinement *param1.1* shows a marked increase in structure from *param1.0*. Both the 500 km and 1300 maps clearly shows structure appearing underneath the continental regions. The next two refinements, *param1.2* and *param1.3*, show little more improvement in the visual quality of the model, ie. there is little more structure resolved. These visual aspects of the model are reflected in the statistics presented above — the first refinement producing the most noticeable increase in model fit whilst further refinements were less significant.

The next level of parameterisation undergoes similar changes through refine-

¹²The term “slow” will be used to describe a wavespeed which is slower than the reference speed, and one which is faster than the reference speed is called “fast”.

ment. *param2.0* shows large scale variations much like would be expected if one were to use a spherical harmonics parameterisation (note that to produce similar results using spherical harmonics would involve fewer parameters [17]). The first refinement, *param2.1*, introduces some structure into the anomalous regions, and *param2.2* sees this structure being further refined with little change in distribution of the anomalies. The third refinement, again, sees little change in the appearance of the model.

The third level of subdivision of the icosahedron, *param3.0*, appears to produce a velocity distribution which agrees with *P-Nature97*. The refinement producing *param3.1* does not resolve any more anomalies but does enhance the structure of those present to conform better with *P-Nature97*. The further refinements, *param3.2* and *param3.3*, enhance the resolution in anomalous regions, but do little to improve the structural properties of these regions.

Parameterisations *param4.0* and *param4.1* show the most agreement with *P-Nature97*, probably due to the cell distribution in *param4.0* being comparable to that in the spherical grid used by Widijantoro [58]. Note that the anomalies in *param4.1* are much more emphasized than in *param4.0*. This effect occurs with the other parameterisations, although not at such a dramatic extent. It is most likely due to the model being biased towards smaller cell sizes.

Generally, each refinement series attempts to identify regions of high velocity variation, and upon successive refinement will attempt to further refine these velocity anomalies. This reflects precisely the imposed condition that refinement is to proceed in regions with maximum spatial gradients.

Conclusion

This examination of self-adaptive parameterisations in seismic tomography, through cell bisection, clearly indicates that arbitrary iterations of the process cannot be performed if one seeks to optimise both the number of model parameters and model fit. This finding is supported by an analysis of the key indicators of variance reduction and model parameter numbers, and by visual comparison of the resultant models with an independent model.

As the variance reduction graph (Figure 3.13) shows, the first refinement constitutes the largest increase in variance reduction, with the effect of subsequent refinements being less pronounced. The increase in the number of model parameters (Figure 3.12(a)) behaves inversely to this, with the first refinement resulting in the smallest increase. However, the general trend, over all parameterisations, is that both the variance reduction and number of model parameters increase exponentially as the average cell size decreases. These results imply that resolution enhancements, through irregular refinements, increase upon only a small number of iterations before using a finer regular parameterisation becomes a more optimal regime.

The graphical presentation of the models (Appendix C) demonstrates the effectiveness of using a tetrahedral parameterisation, as compared with a spherical grid method, to represent the lateral velocity variations within the Earth's mantle. Moreover, the refinement technique subdivides only those regions which warrant further resolution, such as where velocity anomalies are greatest. This technique is not biased by data coverage or known velocity structure, and so is a truly adaptive process.

One possible implementation of self-adaptive parameterisations in seismic tomography, could consist of a combination of both irregular and regular refinements. For example, irregularly refining a parameterisation upon odd numbered iterations and some form of regular refinement upon the even number iterations. This would ensure that the resolving capability of the data is not exhausted in regions of high anomalous variations before it is exhausted elsewhere. However, further work would be necessary to analyse the suitability of such a technique.

Future work on self-adaptive parameterisations in seismic tomographic problems need to investigate employing different cell subdivision techniques, such as centroid placement, and different refinement conditions such ray density and other *a priori* constraints. Regions of mesh refinement under the different regimes, spatial gradients as used in this study and ray density, should be compared so as to determine the best method for optimising data usage whilst ensuring velocity anomalies are adequately resolved.

Appendix A

Some Definitions and Theorems

A.1 Snell's Law

In a horizontally stratified medium Snell's law is:

Corollary A.1.1 (Snell's law) *Consider a seismic ray traveling through a region of the Earth with speed v_1 , which is incident on a second region through which the speed is v_2 . Let θ be the angle of incidence, and ψ be the angle of transmission of the boundary between the regions as shown in Figure A.1. Then*

$$\frac{\sin \theta}{v_1} = \frac{\sin \psi}{v_2}. \quad (\text{A.1})$$

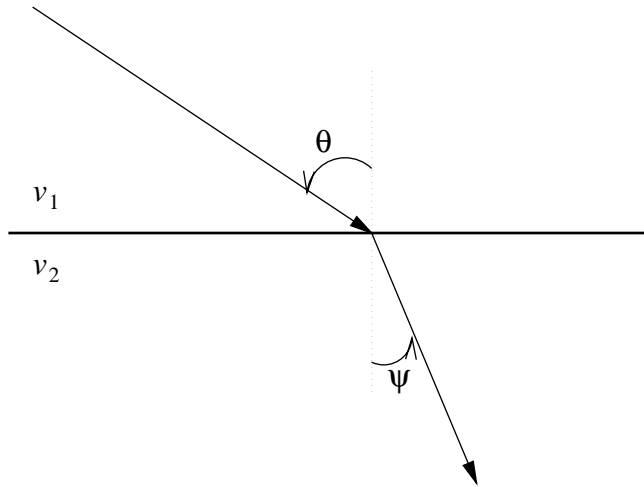


Figure A.1: Demonstration of Snell's law.

PROOF: Consider a ray traveling from P_1 to P_2 , as in Figure A.2. The points P_1 and P_2 are fixed. Let h_1 and h_2 be the distances from P_1 and P_2 to the interface respectively, and also set l_1 and l_2 to be the respective distances to the point of

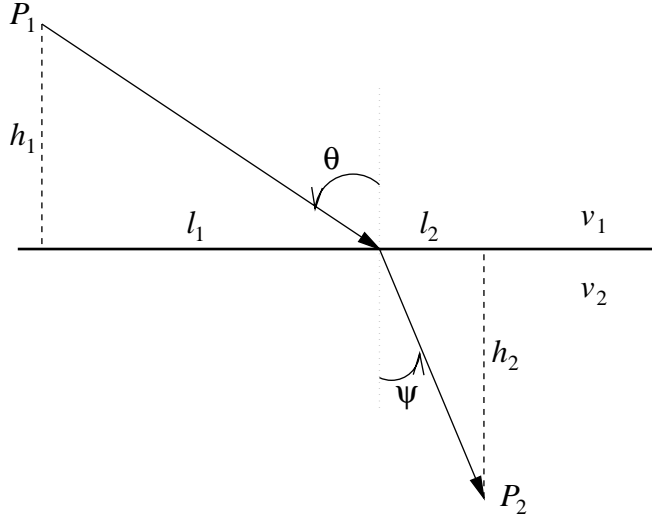


Figure A.2: Proving Snell's law.

refraction. So, the quantities h_1 , h_2 and $l_1 + l_2$ remain fixed. Let P_0 be the point at which the ray intersects the boundary and set $L = l_1 + l_2$, in which case we get

$$\begin{aligned} \int_{P_1}^{P_2} \frac{1}{v} dl &= \int_{P_1}^{P_0} \frac{1}{v_1} dl + \int_{P_0}^{P_2} \frac{1}{v_2} dl \\ &= \frac{1}{v_1} \sqrt{h_1^2 + l_1^2} + \frac{1}{v_2} \sqrt{h_2^2 + l_2^2}. \end{aligned}$$

Now, $l_2 = L - l_1$, in which case Fermat's principle gives

$$\begin{aligned} \frac{d}{dl_1} \left(\frac{1}{v_1} \sqrt{h_1^2 + l_1^2} + \frac{1}{v_2} \sqrt{h_2^2 + (L - l_1)^2} \right) &= 0 \\ \Rightarrow \frac{l_1}{v_1} \frac{1}{\sqrt{h_1^2 + l_1^2}} - \frac{l_2}{v_2} \frac{1}{\sqrt{h_2^2 + l_2^2}} &= 0. \end{aligned}$$

Now, $\sin \theta = \frac{l_1}{\sqrt{h_1^2 + l_1^2}}$ and $\sin \psi = \frac{l_2}{\sqrt{h_2^2 + l_2^2}}$, from which it follows that $\frac{\sin \theta}{v_1} = \frac{\sin \psi}{v_2}$. \square

If this is extended to incorporate more regions, it turns out that $\frac{\sin \theta_i}{v_i}$ is constant along any given ray, where θ_i represents the angle of incidence from the i -th region (through which the ray has velocity v_i) to the $(i+1)$ -th region. More generally, for a medium which varies continuously $\frac{\sin \theta}{v}$ remains constant. In such a medium the ray parameter is $p = \frac{\sin \theta}{v}$, hence its usefulness in ray tracing (note that p is simply the horizontal slowness). For radial stratification the ray parameter becomes $p = \frac{r \sin \theta}{v}$.

A.2 Useful Polynomials

Definition A.2.1 (Legendre polynomial) The function $P_n : R \rightarrow R$ defined by

$$P_n(x) = \frac{1}{2^n n!} \frac{d^n}{dx^n} (x^2 - 1)^n$$

is called the *Legendre polynomial of degree n*.

The Legendre polynomials have the property that

$$\int_{-1}^1 P_n(x) P_{n'}(x) dx = \begin{cases} 0 & n \neq n', \\ \frac{2}{2n+1} & n = n', \end{cases}$$

making them an orthogonal basis on $[-1, 1]$.

Definition A.2.2 (Associated Legendre polynomial) The function $P_{nm} : R \rightarrow R$ defined by

$$P_{nm}(x) = (1 - x^2)^{\frac{m}{2}} \frac{d^m}{dx^m} P_n(x)$$

is called the *associated Legendre polynomial of degree n*.

The associated Legendre polynomials satisfy

$$\int_{-1}^1 P_{nm}(x) P_{n'm}(x) dx = \begin{cases} 0 & n \neq n', \\ \frac{2}{2n+1} \frac{(n+m)!}{(n-m)!} & n = n'. \end{cases}$$

Definition A.2.3 (Chebyshev polynomial) The function $T_n : [-1, 1] \rightarrow R$ defined by

$$T_n(x) = \cos(n \arccos x)$$

is called the *Chebyshev polynomial of degree n*.

A.3 The Fréchet Derivative

In Euclidean space the derivative at a point \mathbf{x} of a function f is the best linear approximation of the function at that point. In more general spaces, in particular normed vector spaces, notions of linearity of a function can be used to define a derivative. However, there are many possible ways to define the derivative of a function in such a space, and one such definition is that of the Fréchet derivative [59, pp 6–9].

Definition A.3.1 (Fréchet derivative) Suppose X and Y are normed vector spaces. Let $\mathbf{a} \in X$ and suppose a function f is defined on an open neighbourhood A of \mathbf{a} , ie. $f : A \rightarrow Y$. f is said to be Fréchet differentiable at \mathbf{a} if there exists a bounded linear transformation $u : X \rightarrow Y$ such that

$$\frac{f(\mathbf{a} + \varepsilon \mathbf{x}) - f(\mathbf{a}) - u(\varepsilon \mathbf{x})}{\varepsilon} \rightarrow \mathbf{0} \text{ uniformly as } \varepsilon \rightarrow 0$$

for each $\mathbf{x} \in X$. If such a function exists then it is called the Fréchet derivative and denoted f' .

In seismic tomography δT_i is regarded as a function from the space of all perturbation models δs (which is a subspace of an L_2 space) to R , ie. $\delta T_i = \delta T_i(\delta s)$. Using the above definition, suppose the Fréchet derivative of δT_i exists and denote it by u , also let x be any slowness perturbation model

$$\begin{aligned} \frac{\delta T_i(\delta s + \varepsilon x) - \delta T_i(\delta s) - u(\varepsilon x)}{\varepsilon} &= \frac{\int_{\Gamma_{0i}} (\delta s + \varepsilon x) \, dl - \int_{\Gamma_{0i}} \delta s \, dl - u(\varepsilon x)}{\varepsilon} \\ &= \frac{\int_{\Gamma_{0i}} \delta s \, dl + \int_{\Gamma_{0i}} \varepsilon x \, dl - \int_{\Gamma_{0i}} \delta s \, dl - u(\varepsilon x)}{\varepsilon} \\ &= \frac{\int_{\Gamma_{0i}} \varepsilon x \, dl - u(\varepsilon x)}{\varepsilon} \\ &= \frac{1}{\varepsilon} \int_{\Gamma_{0i}} \varepsilon x \, dl - \frac{u(\varepsilon x)}{\varepsilon} \\ &= \int_{\Gamma_{0i}} x \, dl - u(x) \\ &\rightarrow 0 \text{ uniformly as } \varepsilon \rightarrow 0 \end{aligned}$$

This must occur for all x , and since there is no dependence on ε and the line integral over Γ_{0i} always exists, the Fréchet derivative exists and is equal to

$$\delta T'_i(x) = u(x) = \int_{\Gamma_{0i}} x \, dl.$$

Therefore the Fréchet derivative of a perturbation model $\delta s = c^j e_j$, where e_j are basis functions, is

$$\begin{aligned} \delta T'_i(\delta s) &= \delta T'_i(c^j e_j) \\ &= c^j \delta T'_i(e_j) \\ &= c^j \int_{\Gamma_{0i}} e_j \, dl. \end{aligned}$$

The Fréchet derivative matrix A_{ij} can be defined as $A_{ij} = \delta T'_i(e_j)$, from which $\delta T'_i(\delta s) = A_{ij} c^j$.

Appendix B

Performance Figures

B.1 Computing Times

| routine | computer | CPUs | memory (Mb) | time (hrs) |
|-------------|--------------------|------|-------------|------------|
| ray tracing | Sun Ultra-Sparc 20 | 1 | 128 | 12–14 |
| <i>LSQR</i> | DEC Alpha | 2 | 256 | 2–3 |

Table B.1: Computing times.

B.2 Model Statistics

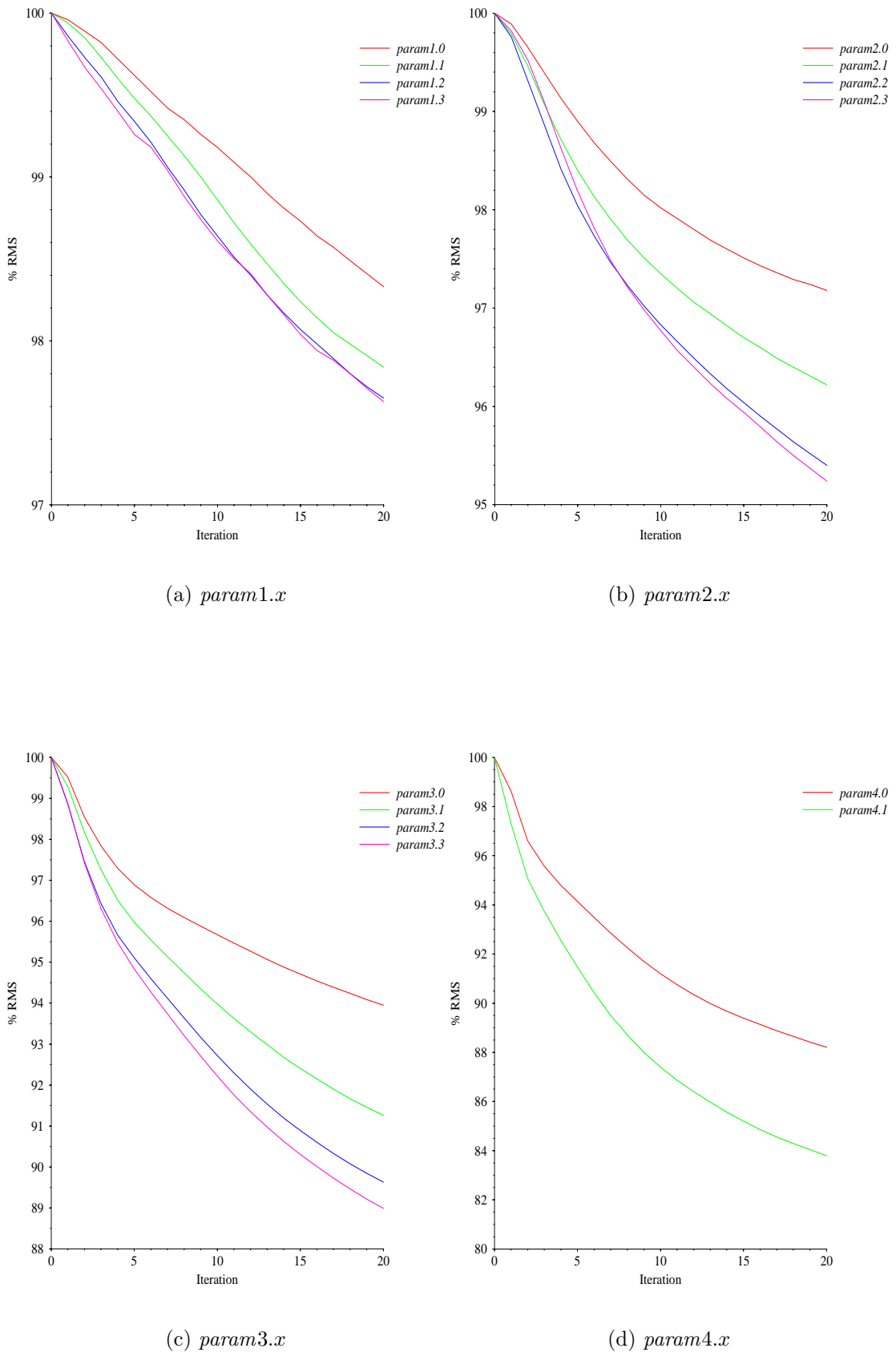


Figure B.1: Model convergence using % RMS as the indicator.

| Parameterisation | <i>ncell</i> | <i>npoints</i> | V.R. |
|------------------|--------------|----------------|--------|
| <i>param1.0</i> | 4,056 | 649 | 4.65% |
| <i>param1.1</i> | 7,258 | 1,177 | 5.97% |
| <i>param1.2</i> | 14,428 | 2,245 | 6.61% |
| <i>param1.3</i> | 26,457 | 4,163 | 6.66% |
| <i>param2.0</i> | 16,189 | 2,479 | 7.25% |
| <i>param2.1</i> | 28,814 | 4,458 | 9.30% |
| <i>param2.2</i> | 54,284 | 8,411 | 11.36% |
| <i>param2.3</i> | 101,257 | 15,765 | 11.85% |
| <i>param3.0</i> | 64,973 | 9,799 | 15.01% |
| <i>param3.1</i> | 113,225 | 17,626 | 20.67% |
| <i>param3.2</i> | 209,889 | 32,931 | 24.02% |
| <i>param3.3</i> | 386,019 | 60,813 | 25.45% |
| <i>param4.0</i> | 259,418 | 39,079 | 26.69% |
| <i>param4.1</i> | 452,634 | 70,402 | 34.28% |

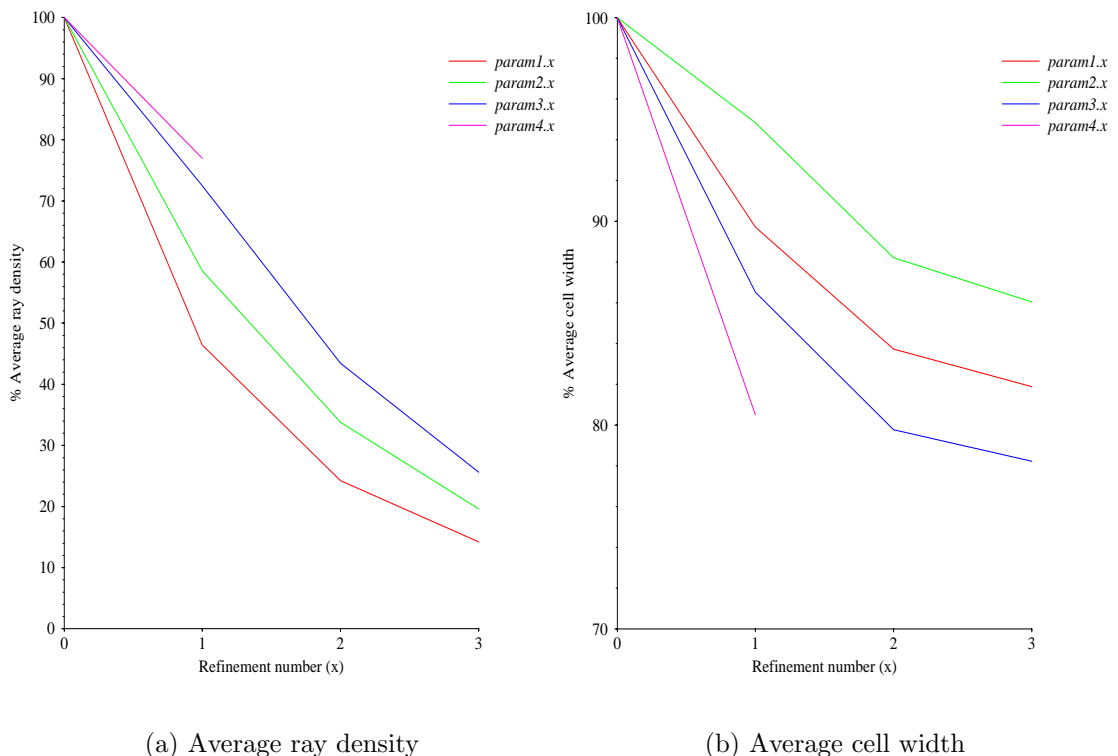
Table B.2: Results of refining the four parametrisations *param*(*n*).0.

Figure B.2: Indicators of average cell properties.

Appendix C

Velocity Models

C.1 *param1.x*

C.1.1 500 km

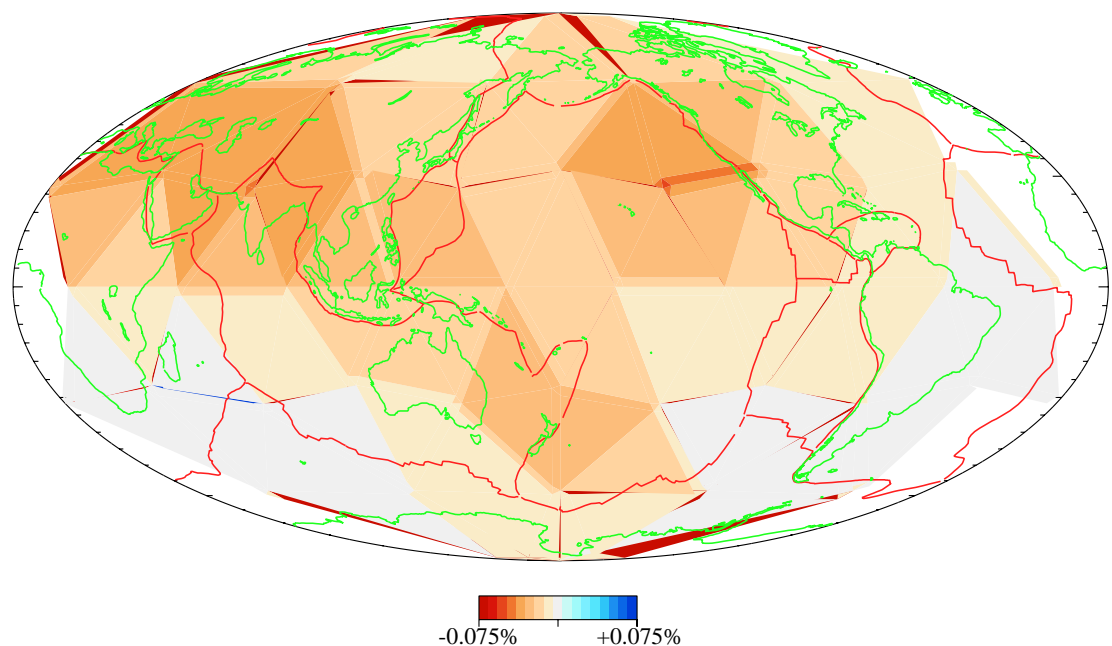
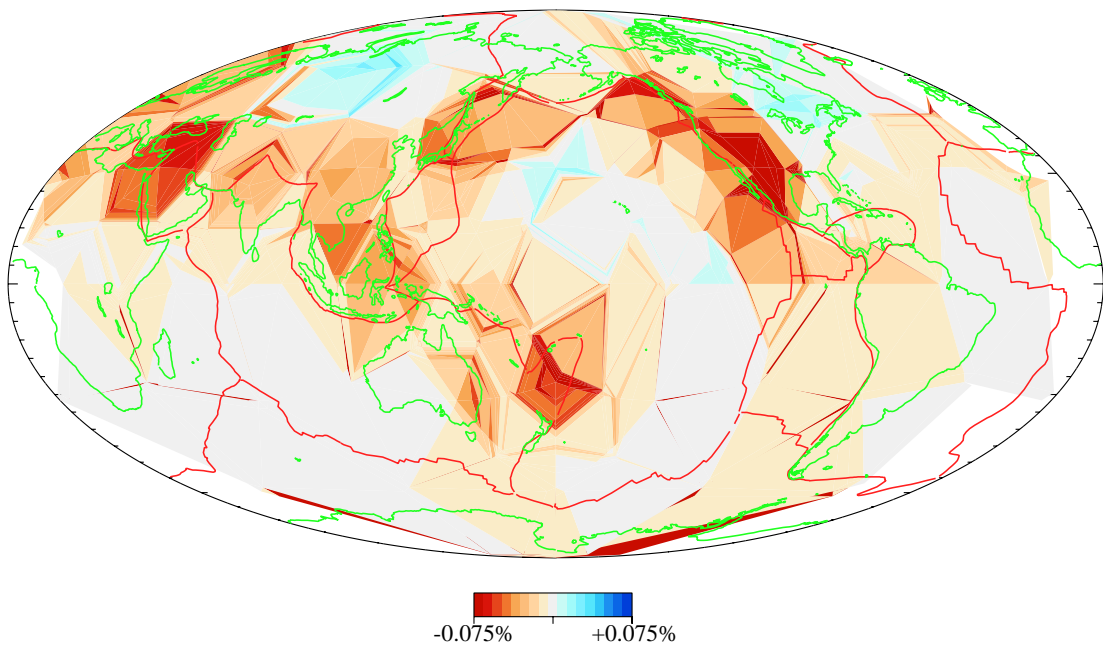
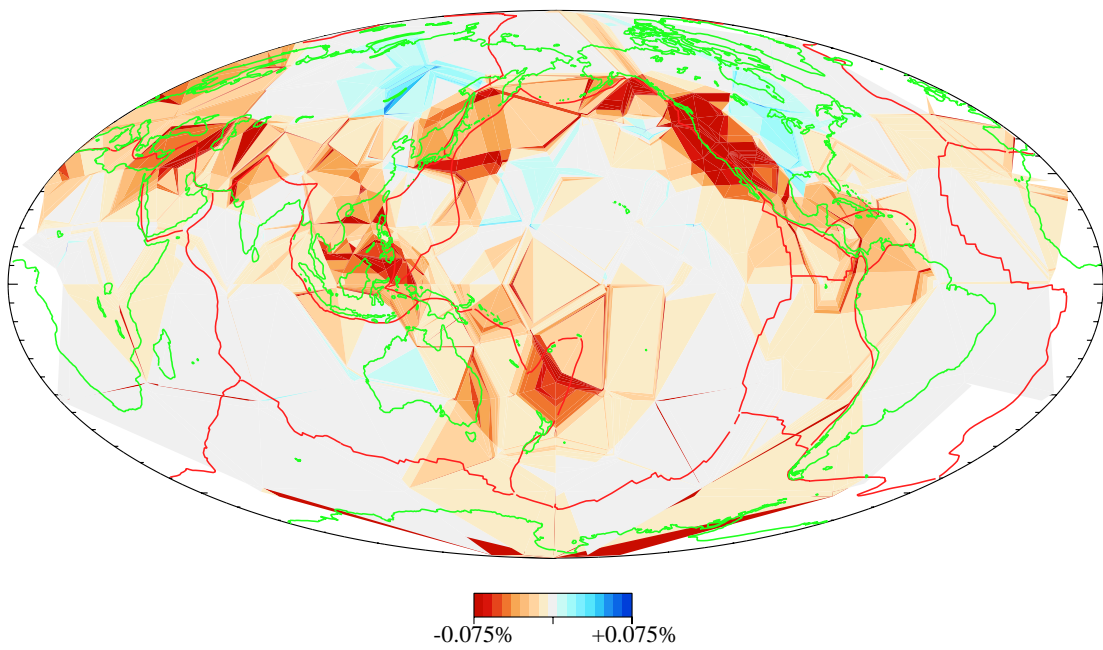
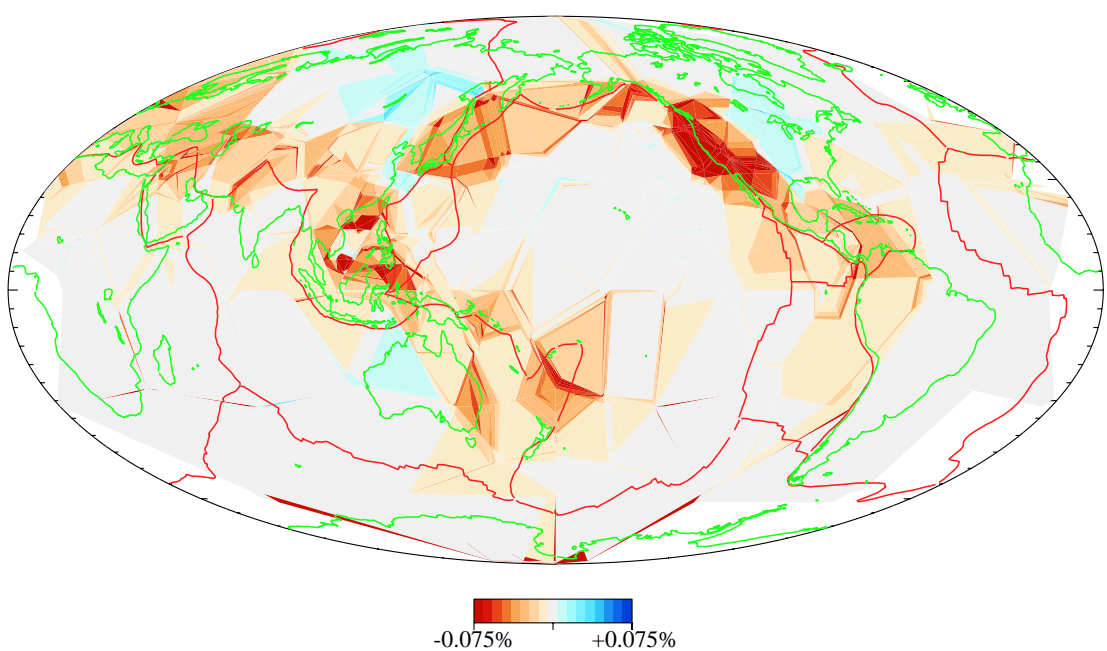


Figure C.1: *param1.0*

Figure C.2: *param1.1*Figure C.3: *param1.2*

Figure C.4: *param1.3*

C.1.2 1300 km

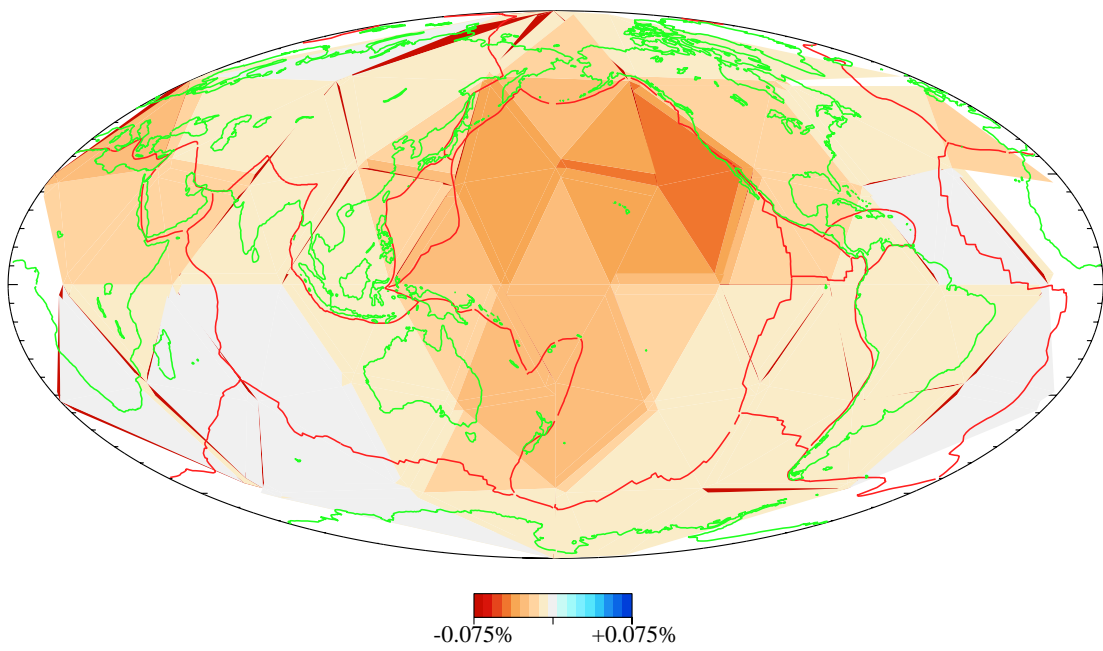


Figure C.5: *param1.0*

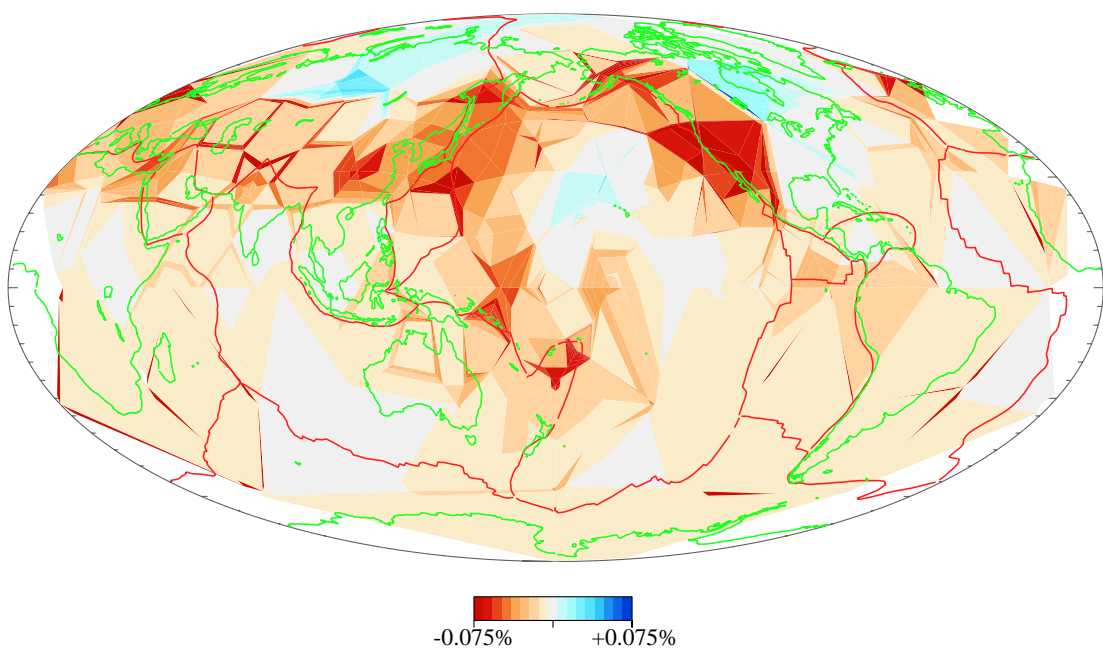
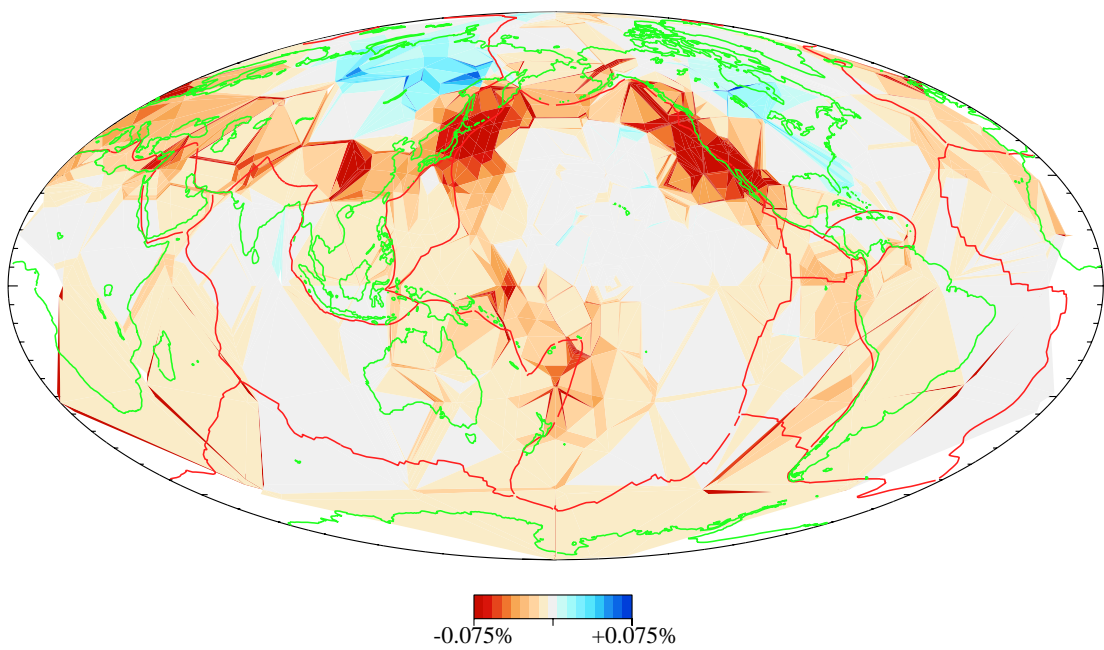
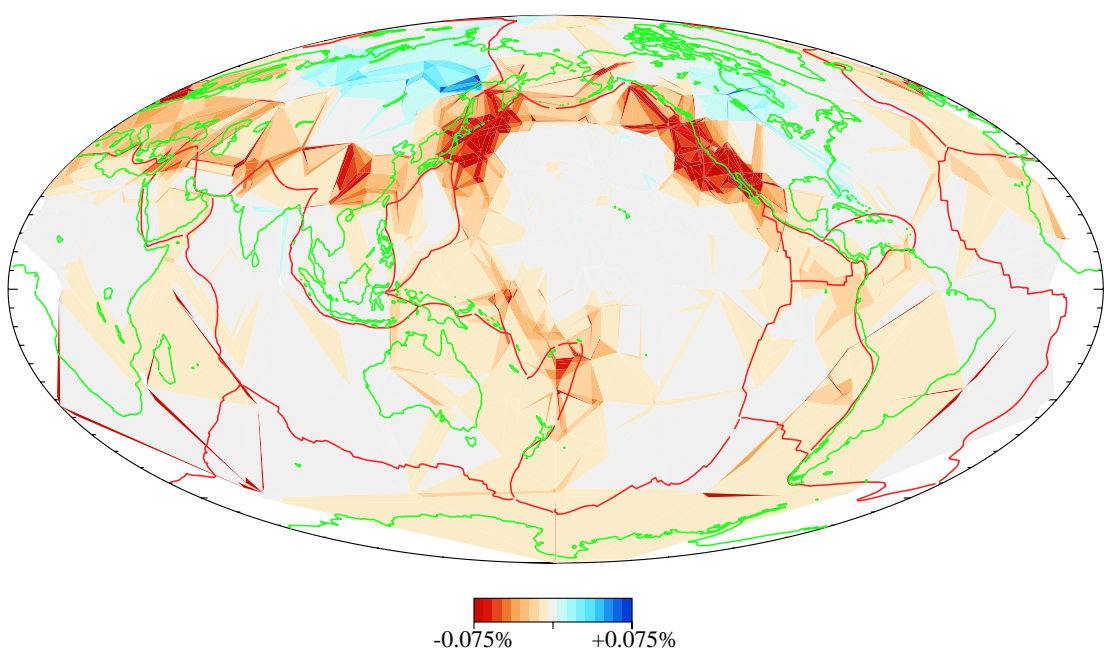


Figure C.6: *param1.1*

Figure C.7: *param1.2*Figure C.8: *param1.3*

C.1.3 Mesh Slices

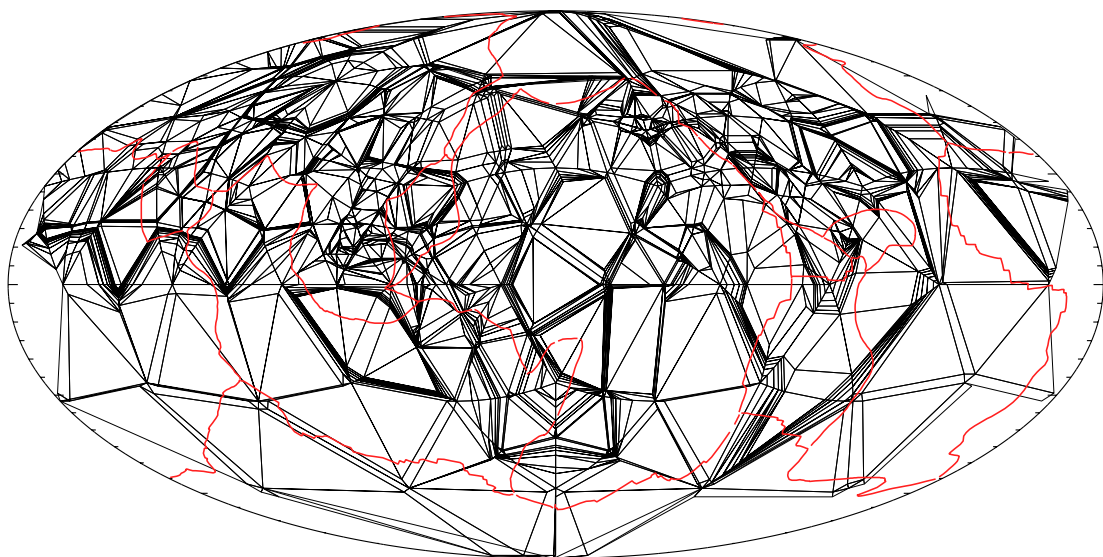


Figure C.9: *param1.3* at 500 km

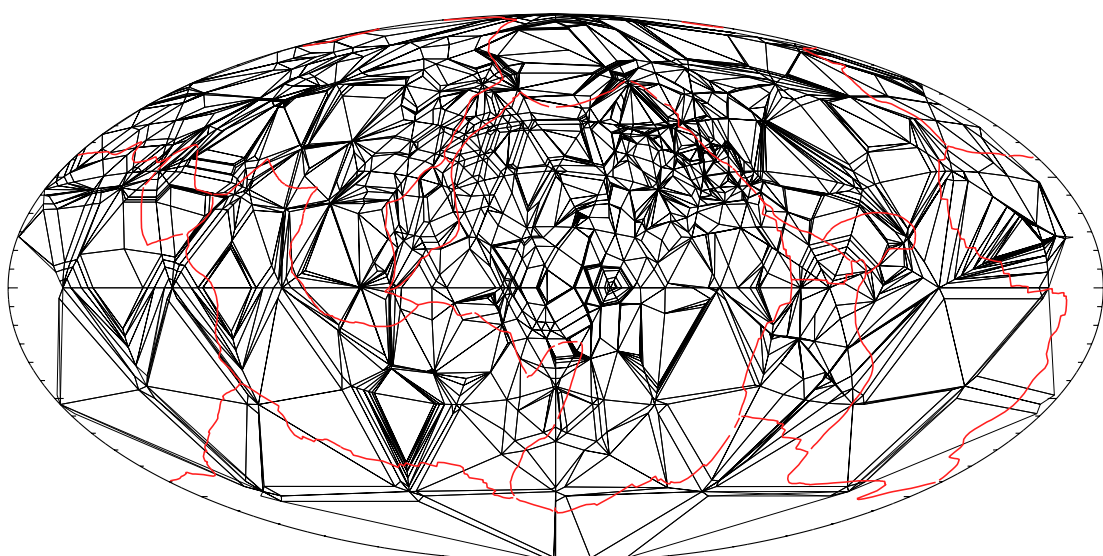


Figure C.10: *param1.3* at 1300 km

C.2 *param2.x*

C.2.1 500 km

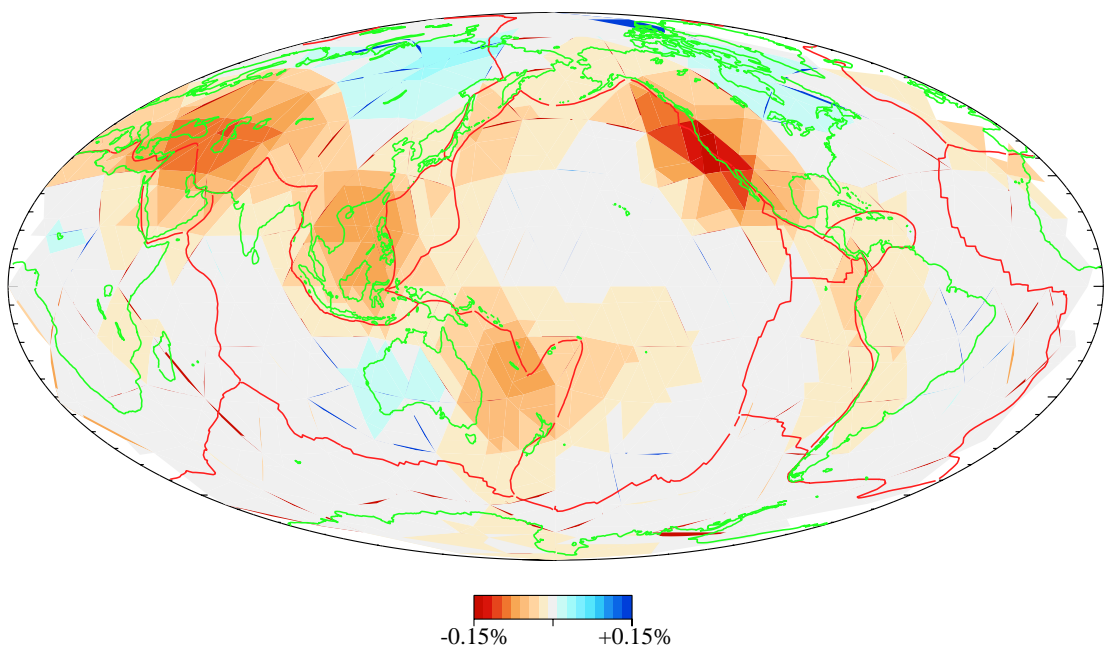


Figure C.11: *param2.0*

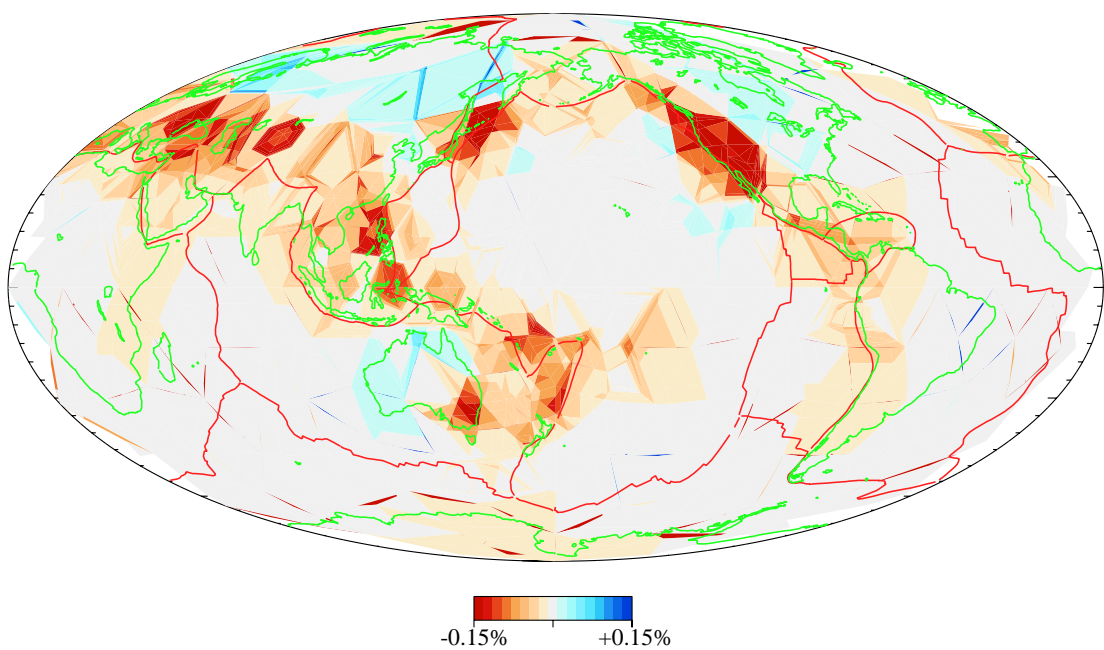
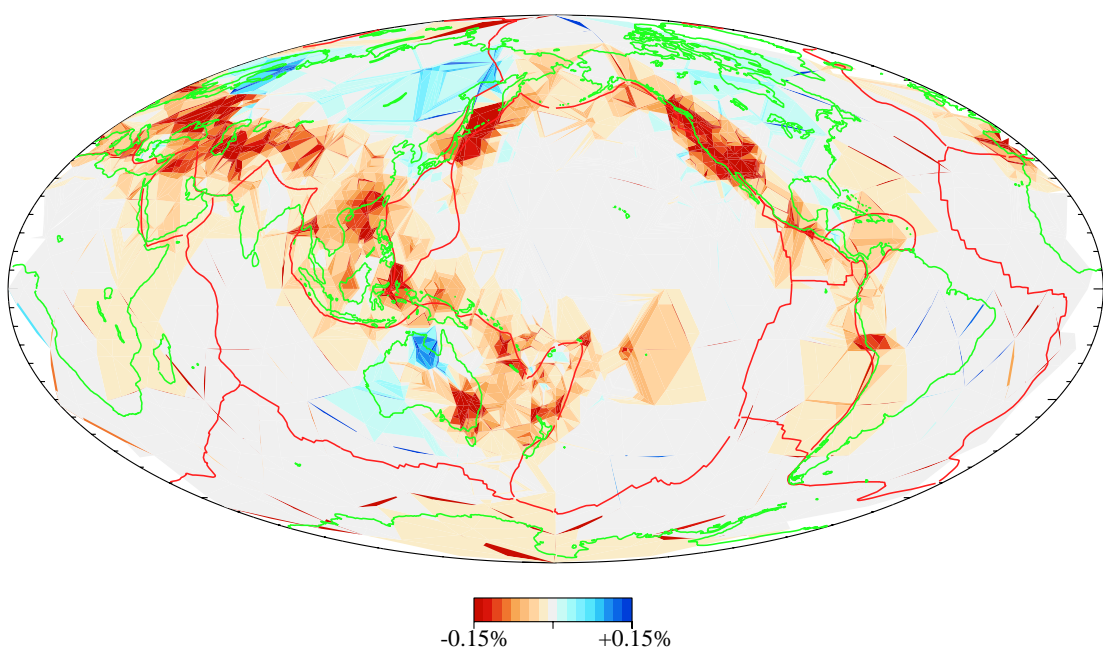
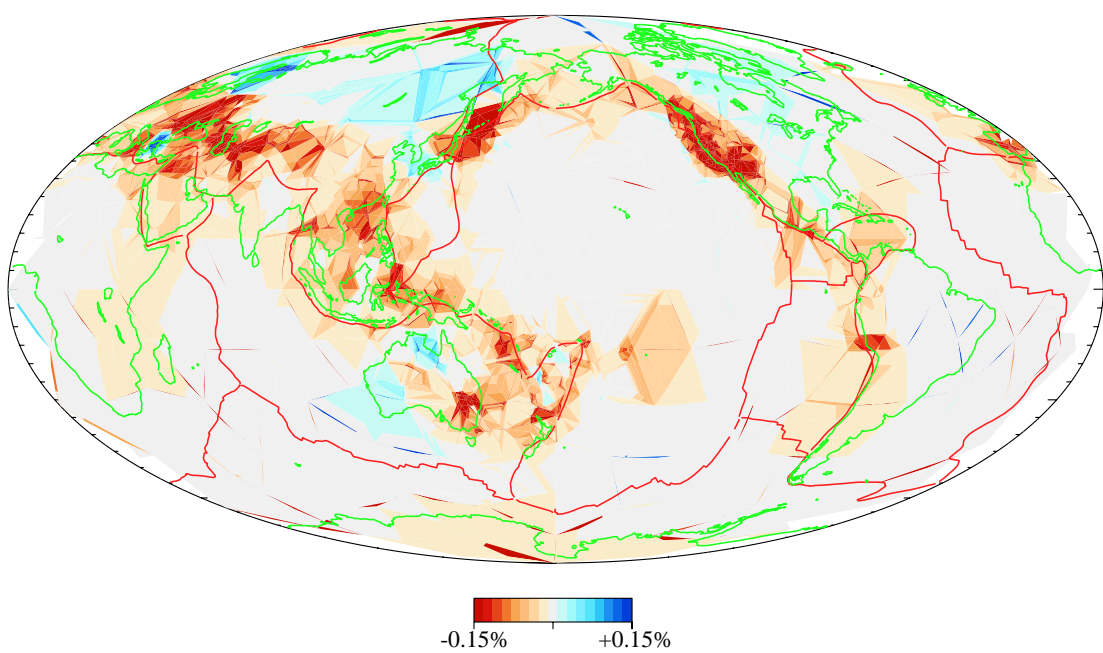


Figure C.12: *param2.1*

Figure C.13: *param2.2*Figure C.14: *param2.3*

C.2.2 1300 km

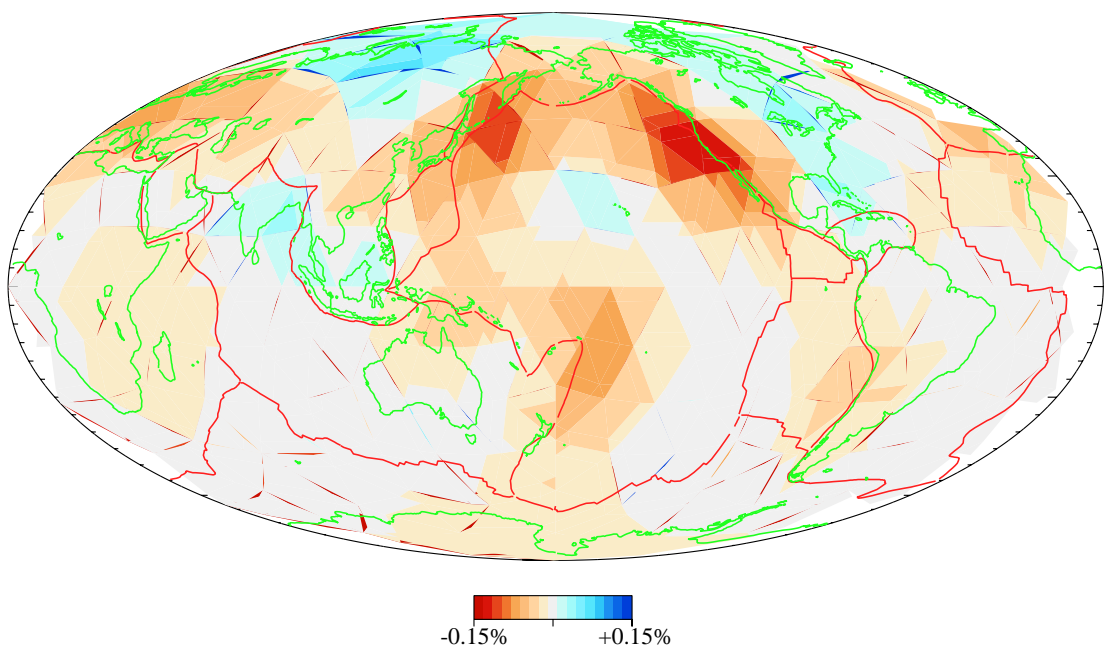


Figure C.15: *param2.0*

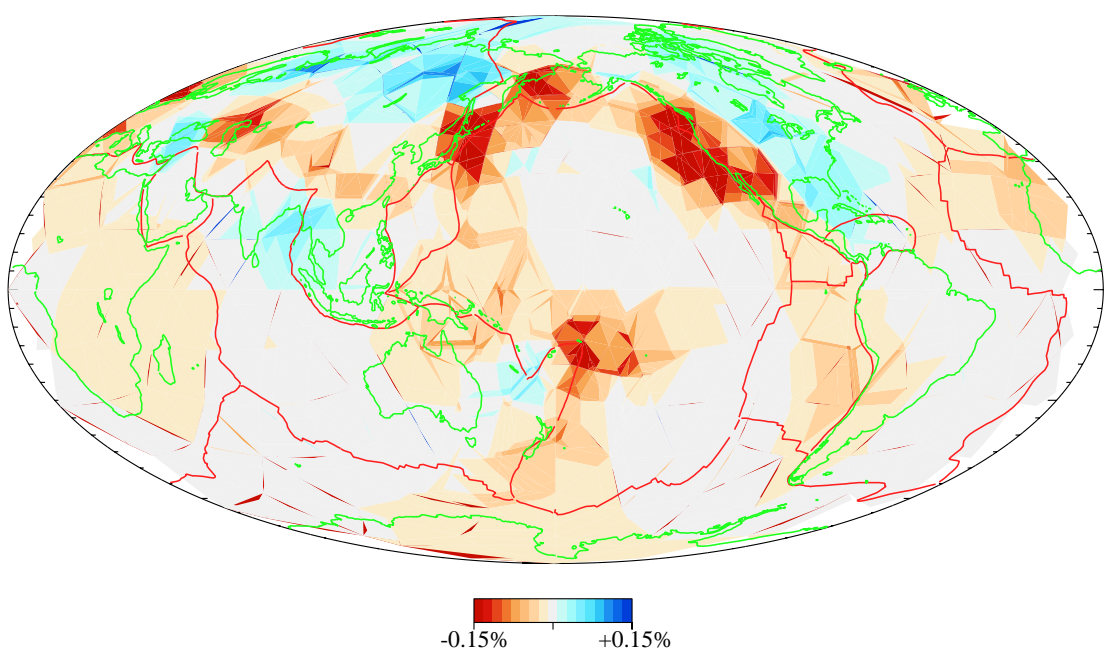
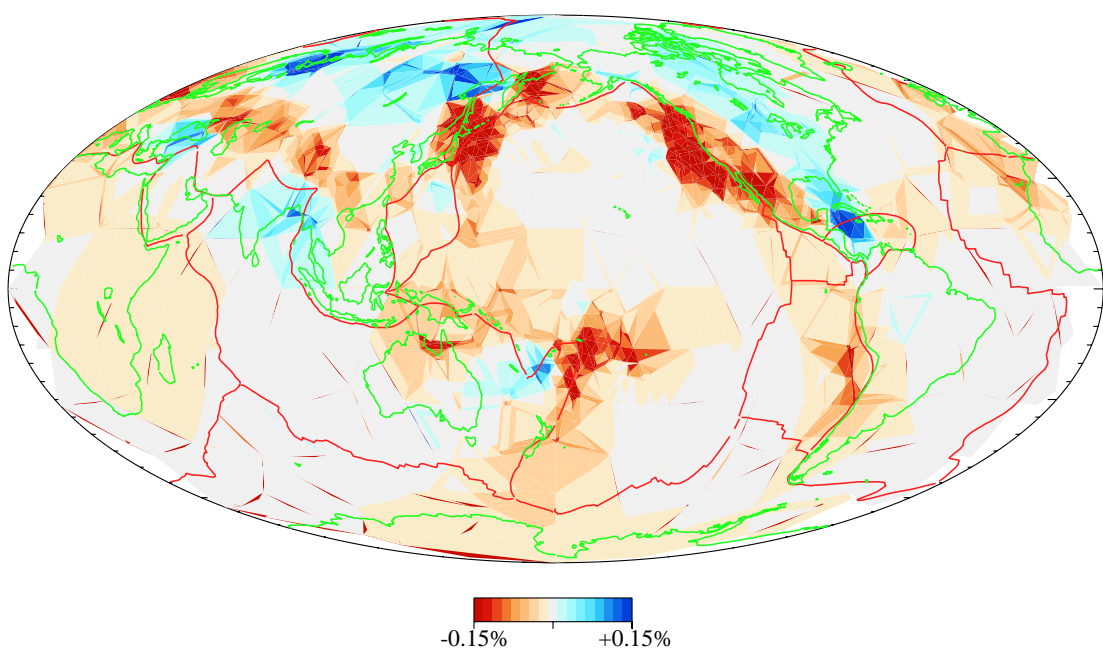
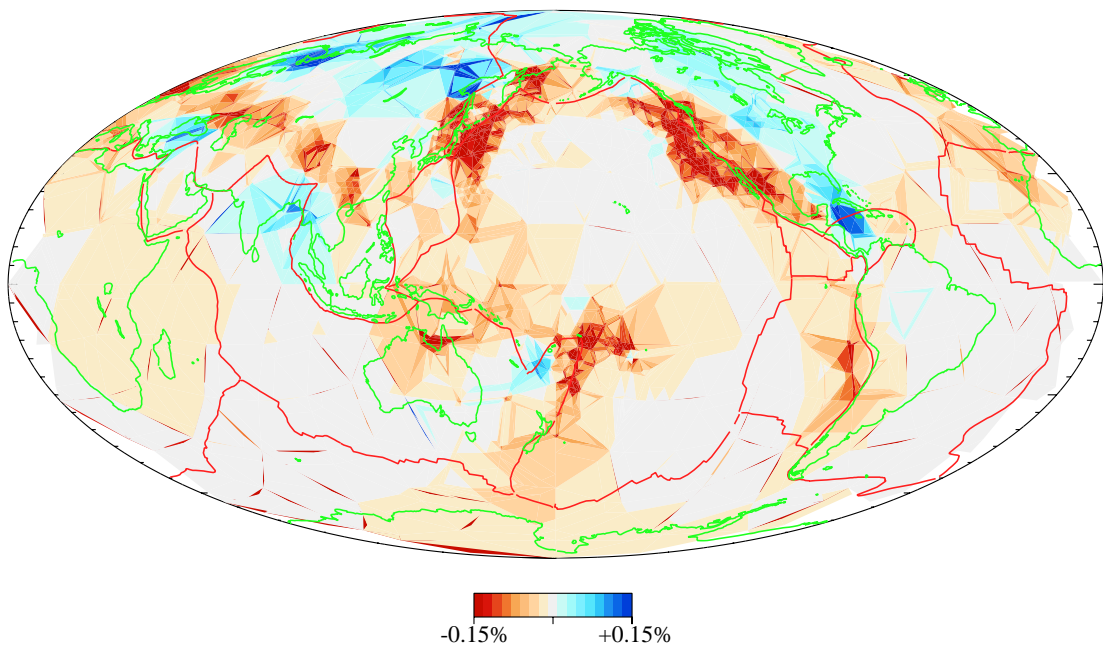


Figure C.16: *param2.1*

Figure C.17: *param2.2*Figure C.18: *param2.3*

C.2.3 Mesh Slices

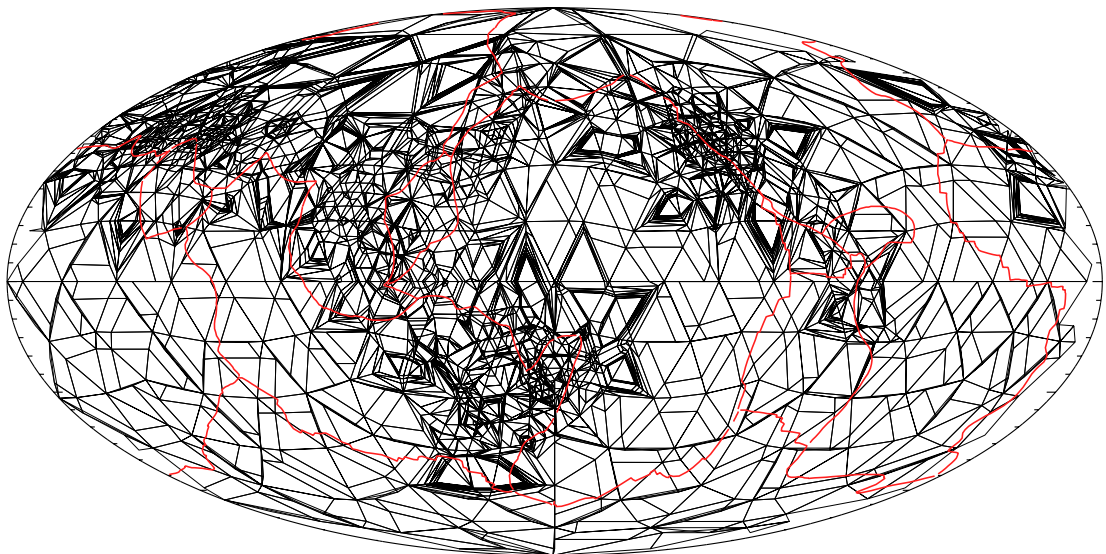


Figure C.19: *param2.3* at 500 km

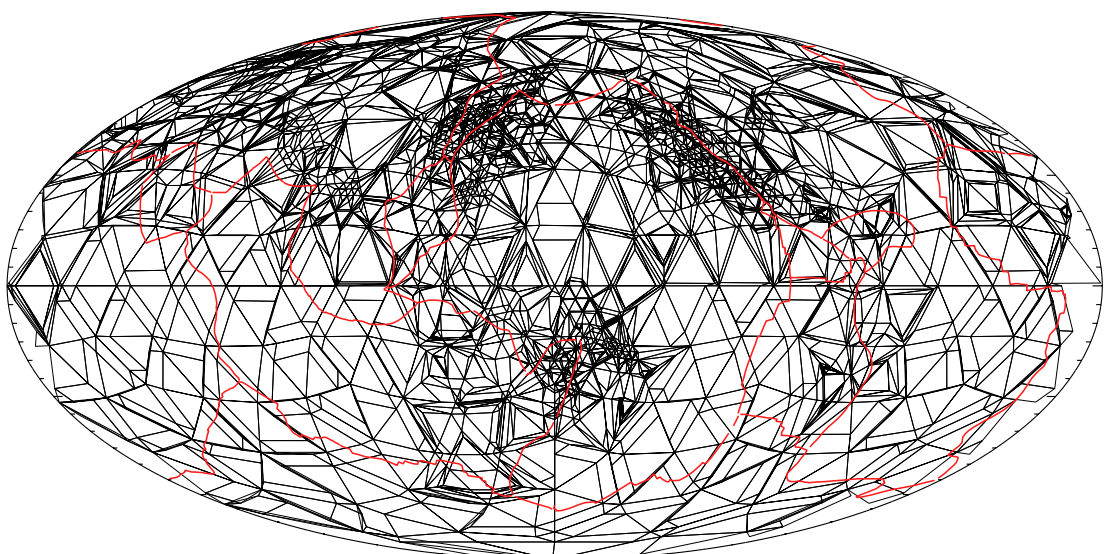


Figure C.20: *param2.3* at 1300 km

C.3 *param3.x*

C.3.1 500 km

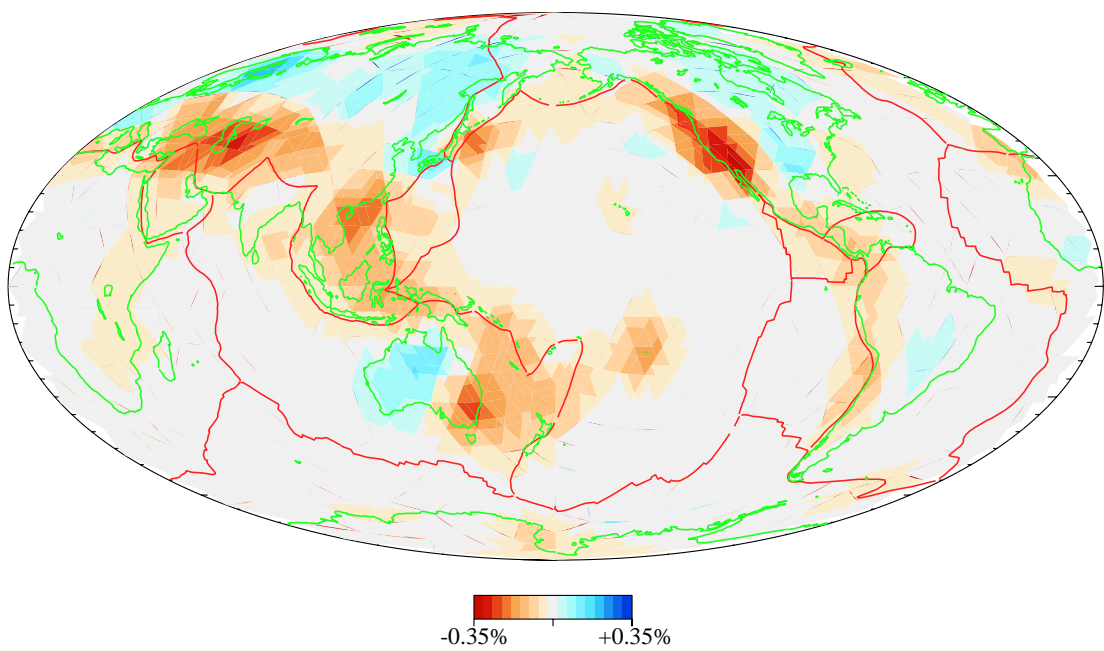


Figure C.21: *param3.0*

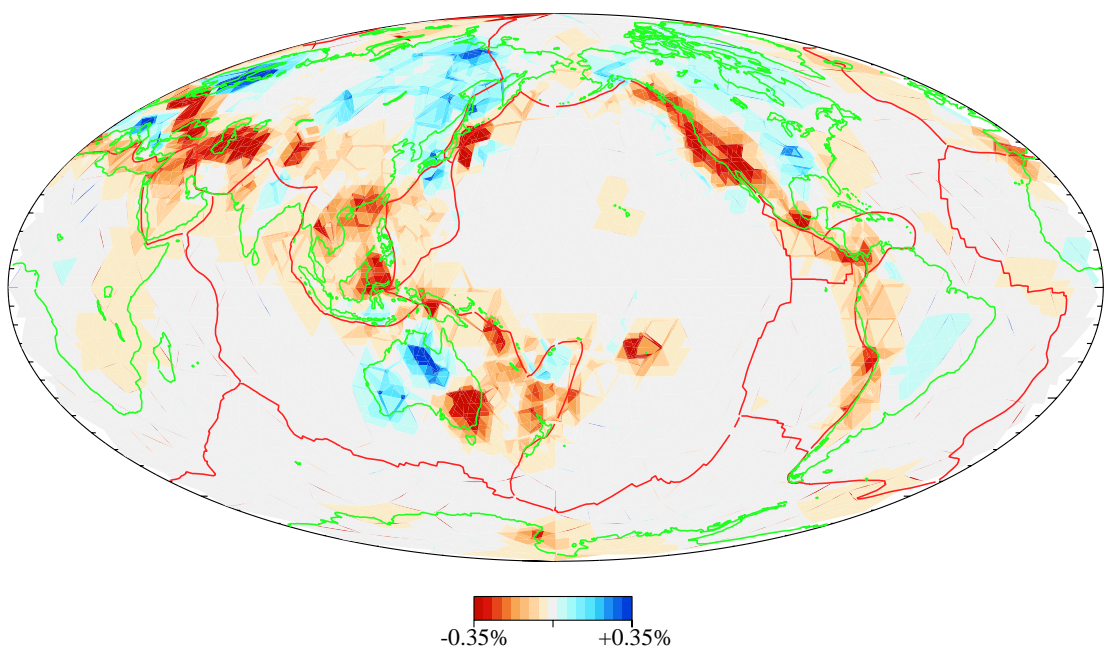
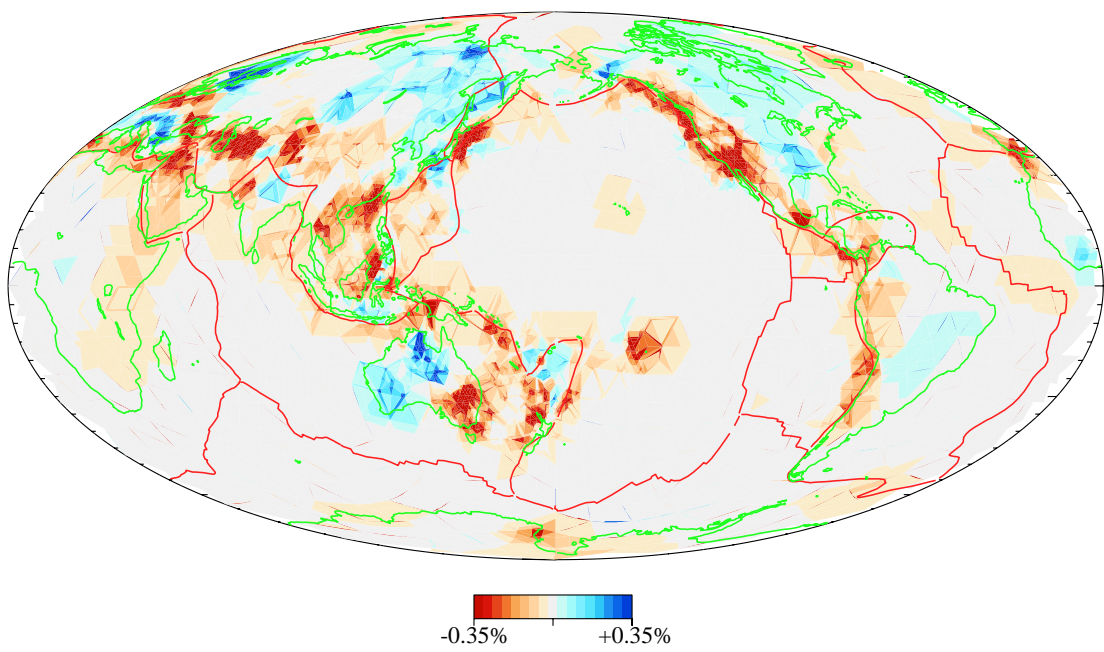
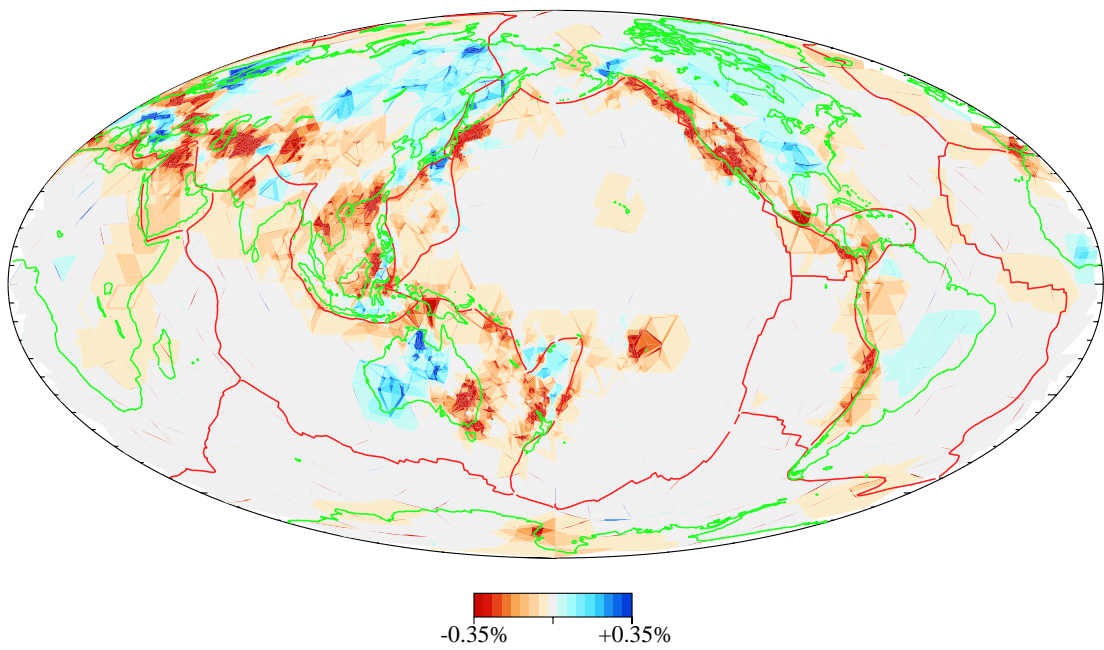


Figure C.22: *param3.1*

Figure C.23: *param3.2*Figure C.24: *param3.3*

C.3.2 1300 km

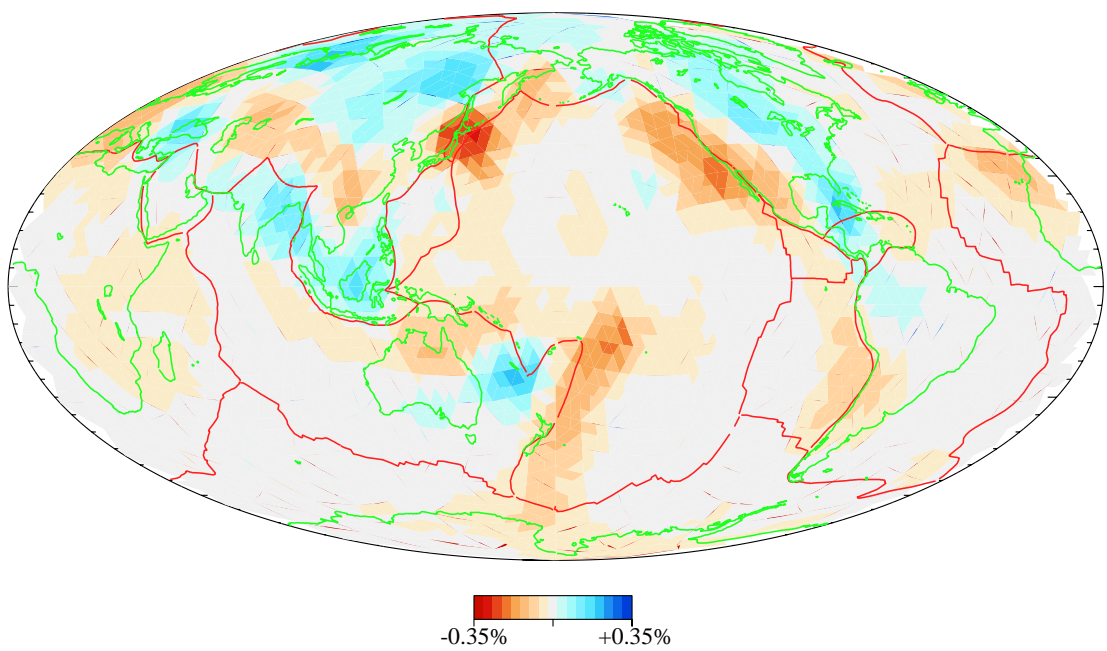


Figure C.25: *param3.0*

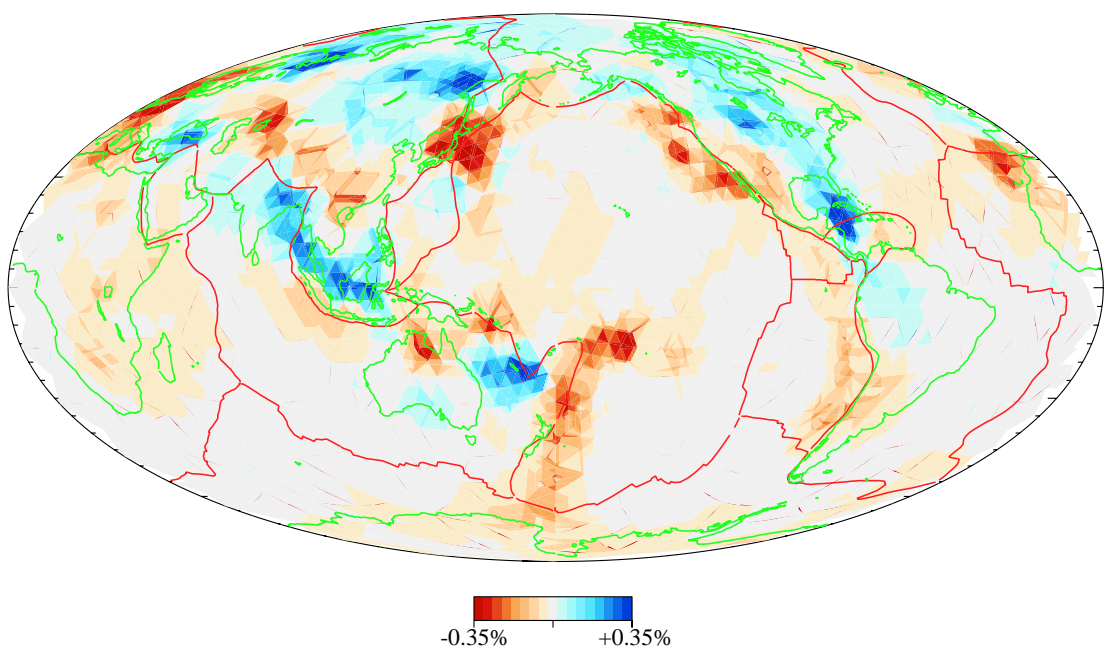
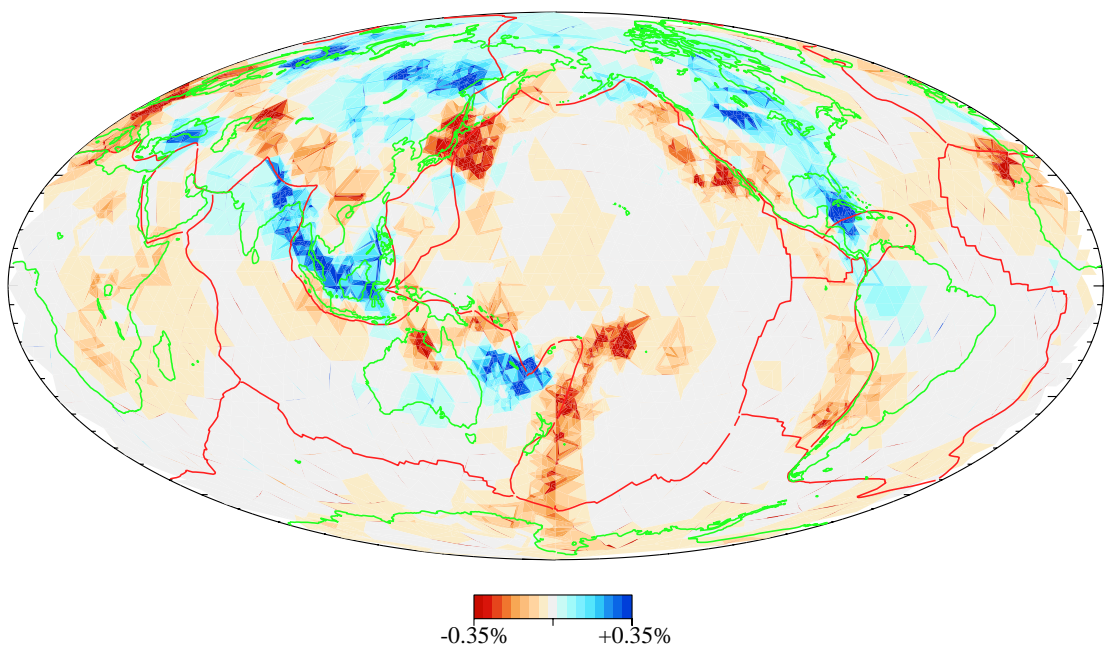
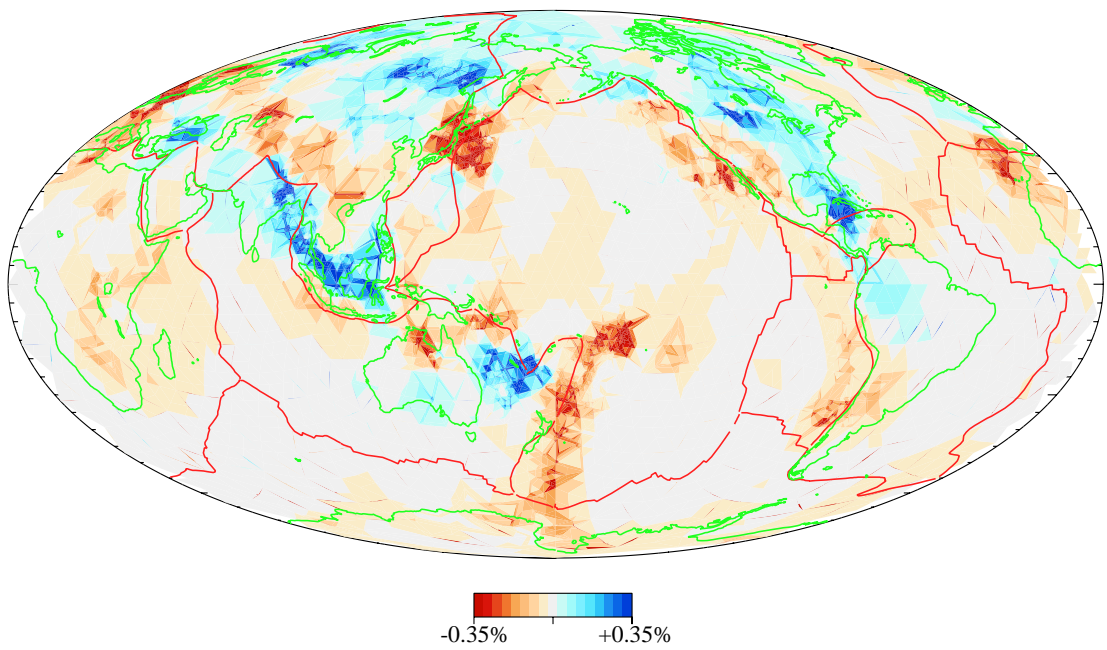


Figure C.26: *param3.1*

Figure C.27: *param3.2*Figure C.28: *param3.3*

C.3.3 Mesh Slices

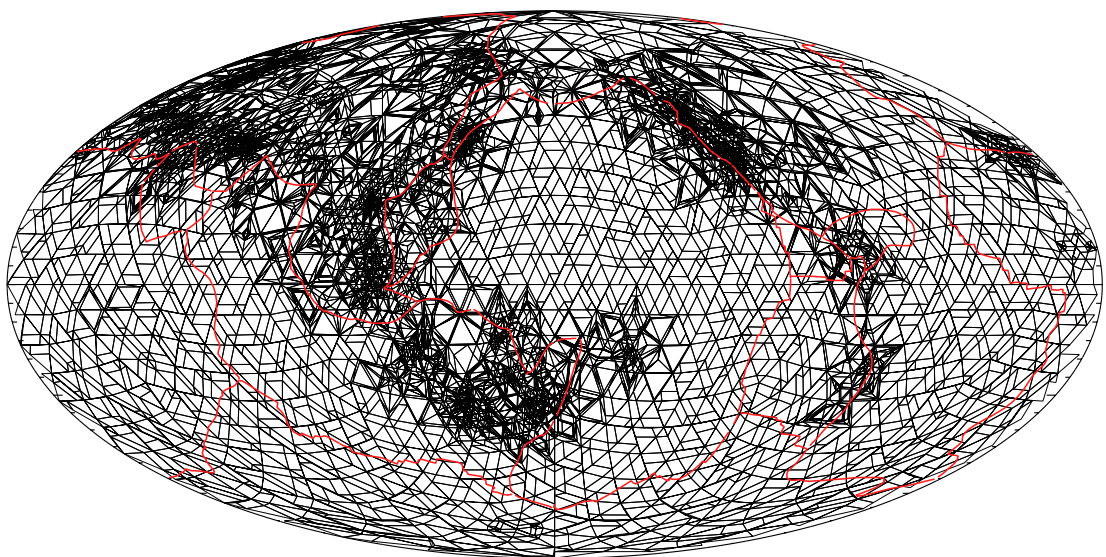


Figure C.29: *param3.3* at 500 km

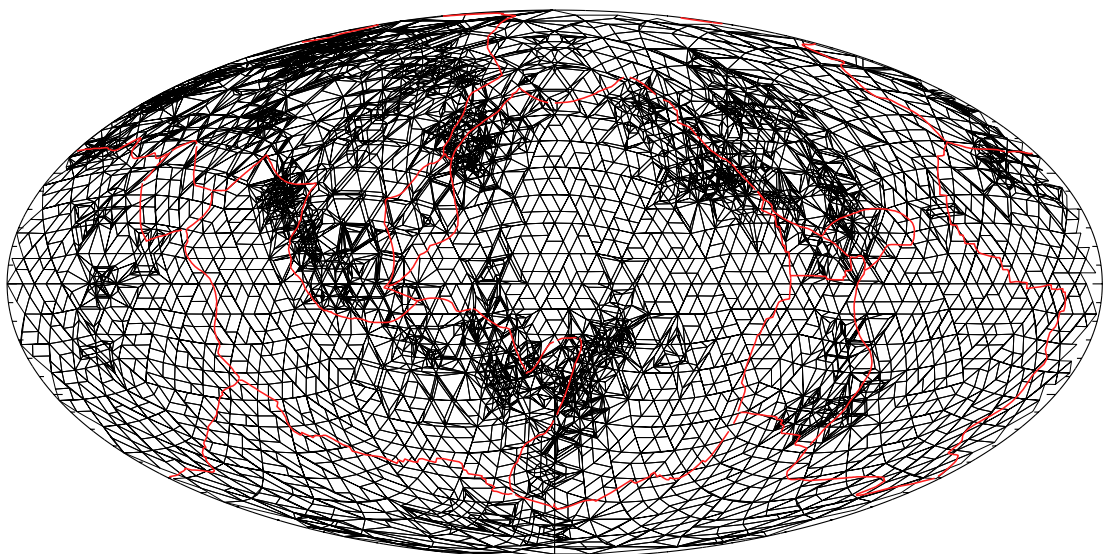


Figure C.30: *param3.3* at 1300 km

C.4 *param4.x*

C.4.1 500 km

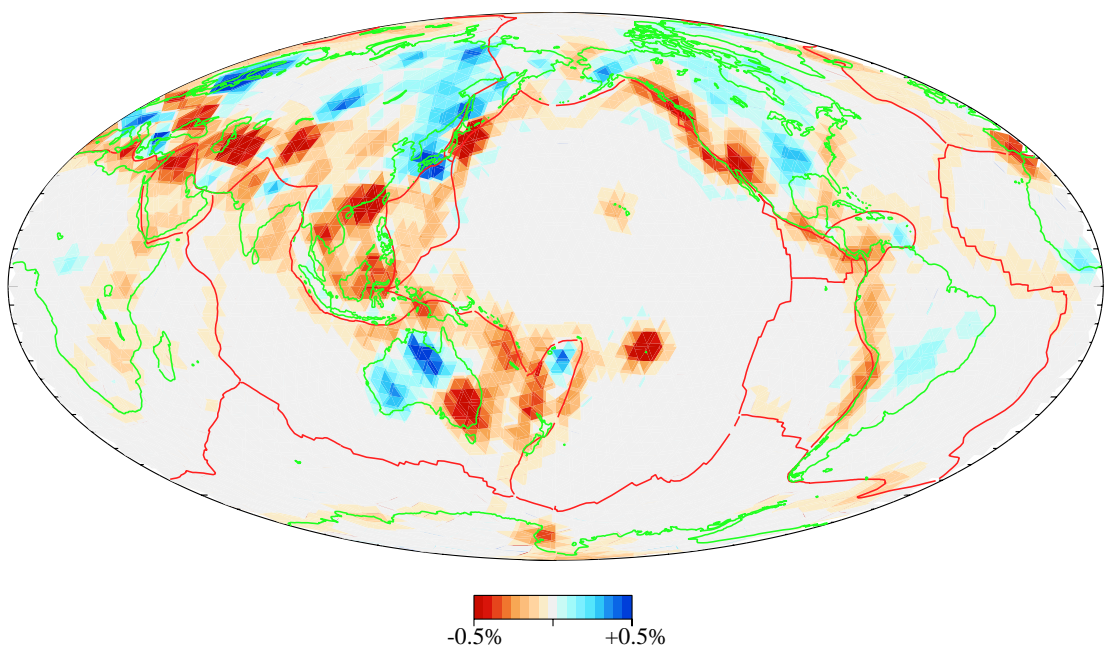


Figure C.31: *param4.0*

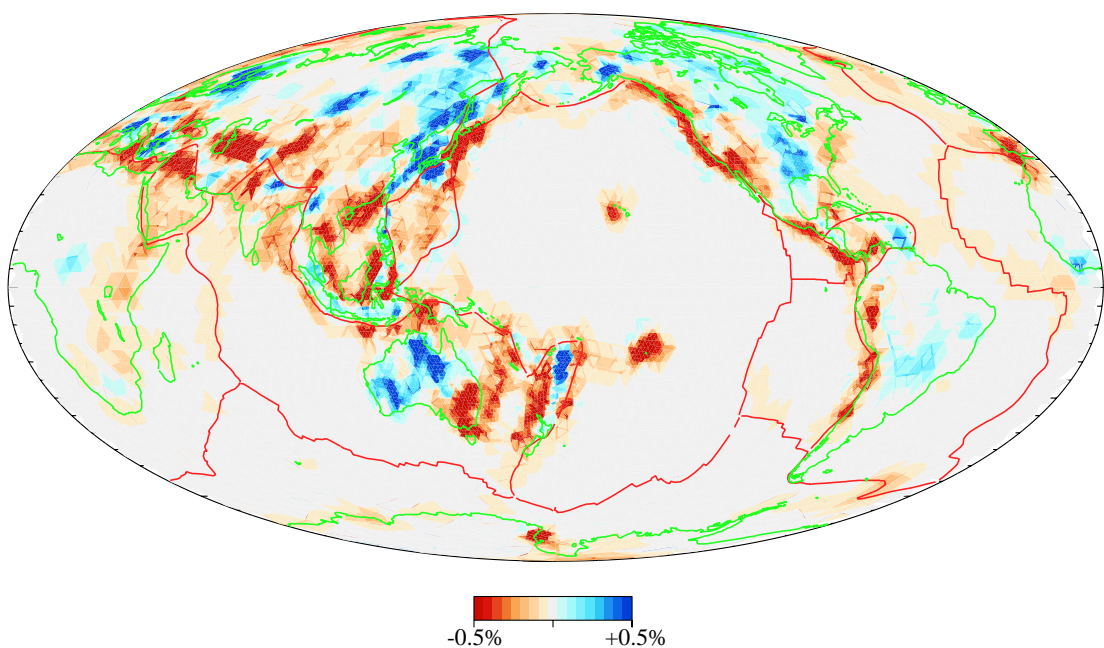


Figure C.32: *param4.1*

C.4.2 1300 km

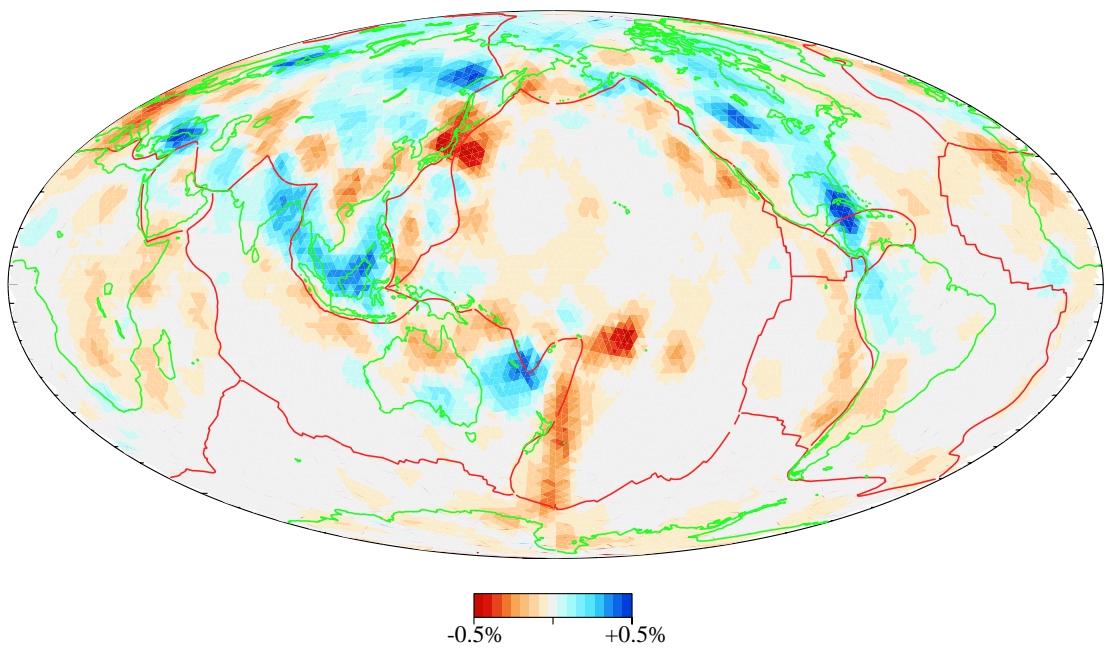


Figure C.33: *param4.0*

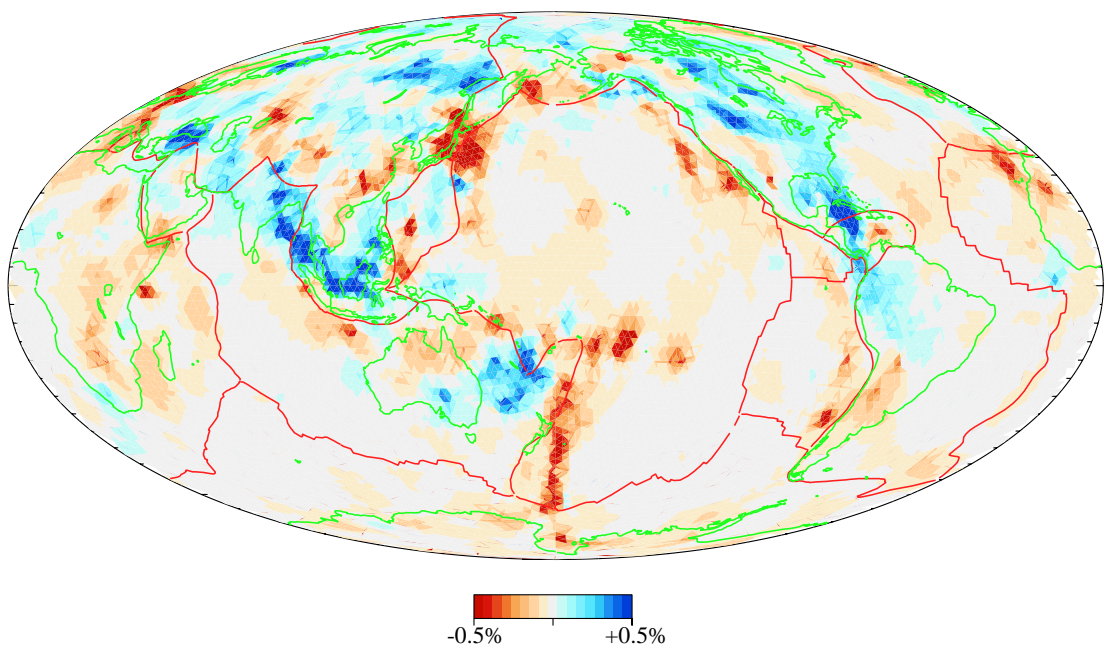


Figure C.34: *param4.1*

C.4.3 Mesh Slices

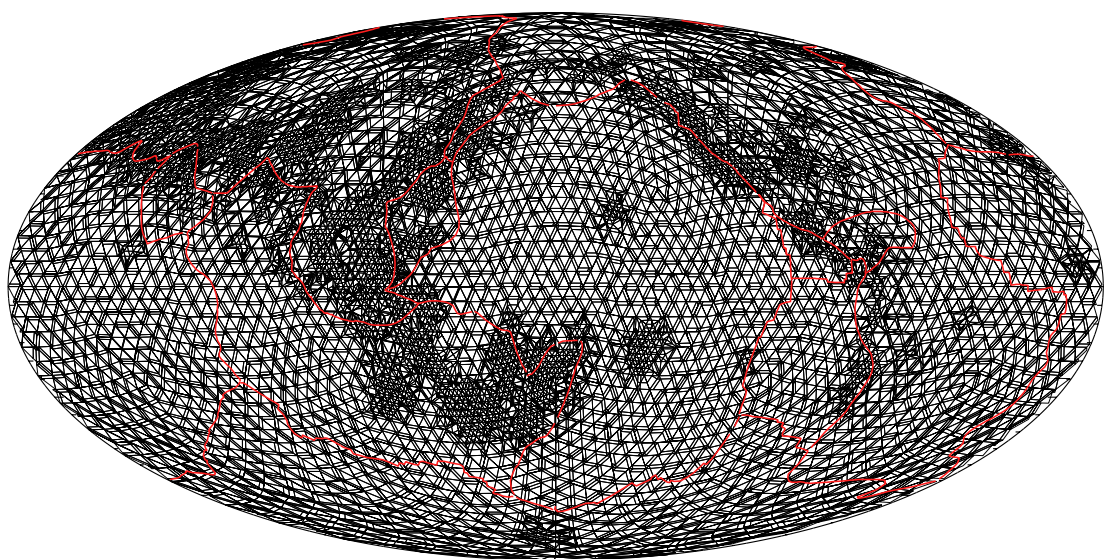


Figure C.35: *param4.1* at 500 km

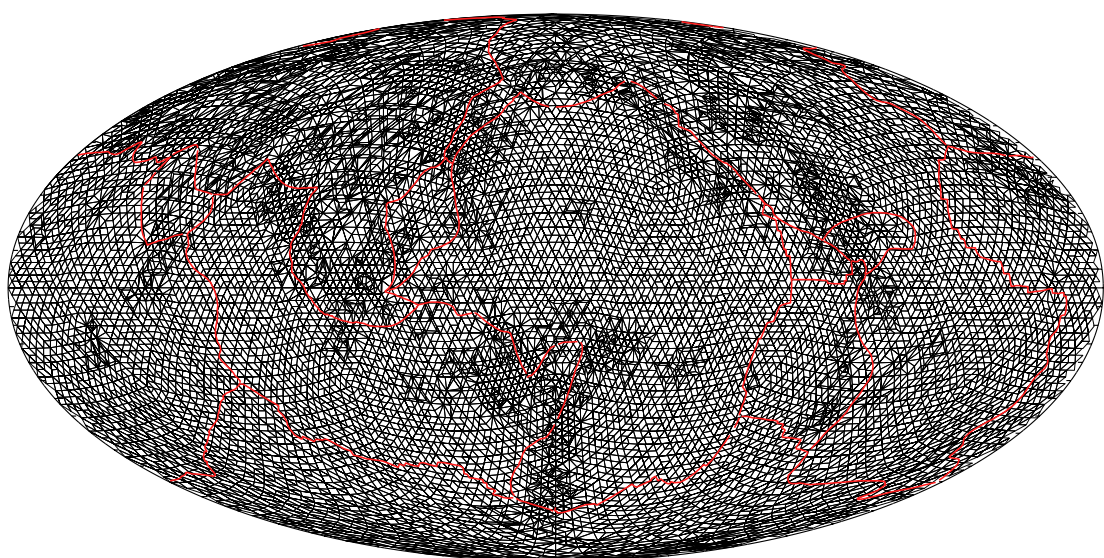


Figure C.36: *param4.1* at 1300 km

C.5 *P-Nature97*

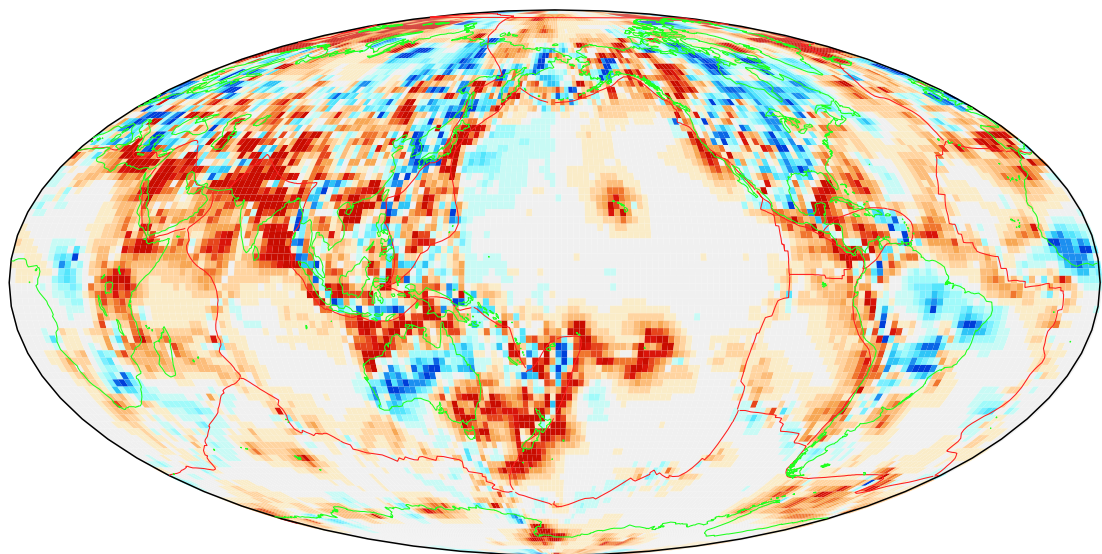


Figure C.37: 500 km

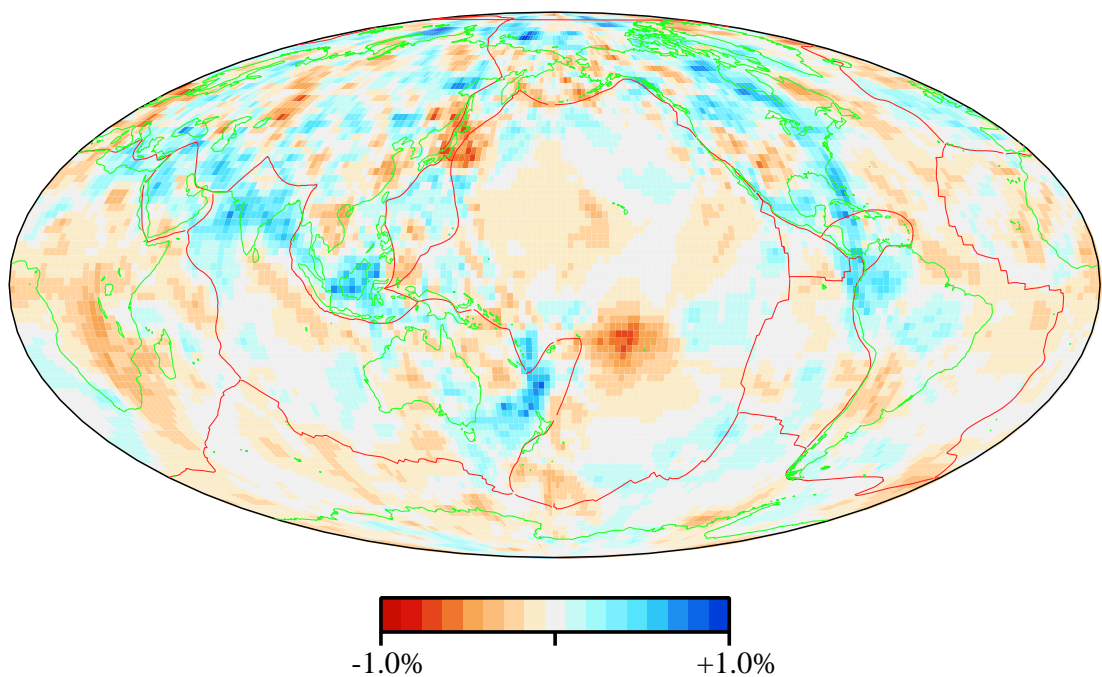


Figure C.38: 1300 km

Bibliography

- [1] K. Aki and P. G. Richards. *Quantitative Seismology*, volume II. Freeman, San Francisco, 1980.
- [2] C. B. Barber, D. P. Dobkin, and H. Huhdanpaa. The quickhull algorithm for convex Hull. Technical Report GCG53, Geometry Center, University of Minnesota, Minneapolis, July 1993.
- [3] M. Båth and A. J. Berkhouit. *Mathematical Aspects of Seismology*, volume 17 of *Seismic Exploration*. Geophysical Press, London, second edition, 1984.
- [4] R. A. Benson and D. S. McRae. A solution-adaptive mesh algorithm for dynamic/static refinement of two and three dimensional grids. In A. S.-Arcilla, J. Häuser, P. R. Eiseman, and J. F. Thompson, editors, *Numerical Grid Generation in Computational Fluid Dynamics and Related Fields*, pages 185–199. North-Holland, Amsterdam, 1991.
- [5] B. A. Bolt. *Earthquakes: A Primer*. Freeman, New York, 1978.
- [6] B. A. Bolt. The fine structure of the Earth’s interior. In *Earthquakes and Volcanoes*, chapter 6, pages 74–83. Freeman, San Francisco, 1980.
- [7] K. E. Bullen. *The Earth’s Density*. Chapman and Hall, London, 1975.
- [8] K. E. Bullen and B. A. Bolt. *An Introduction to the Theory of Seismology*. Cambridge University Press, Cambridge, fourth edition, 1985.
- [9] R. Burridge. *Some Mathematical Topics in Seismology*. New York University, New York, 1976.
- [10] I. F. Clark and B. J. Cook, editors. *Perspectives of the Earth*. Australian Academy of Science, Canberra, 1992.
- [11] C. G. Constable, R. L. Parker and P. B. Stark. Geomagnetic field models incorporating frozen-flux constraints. *Geophysical Journal International*, 113:419–433, 1993.

- [12] Information about silicone compounds. Dow Corning Corporation, 1987. DOW CORNING 3179 dilatant compound.
- [13] A. Curtis and R. Snieder. Reconditioning inverse problems using the generic algorithm and revised parameterisation. Unpublished, 1995.
- [14] R. A. Daly. *Our Mobile Earth*. Scribner, New York, 1926.
- [15] C. Davison. *The Origin Of Earthquakes*. Cambridge University Press, London, 1912.
- [16] T. K. Dey, H. Edelsbrunner, and S. Guha. Computational topology, In *Computational Geometry: Ten Years Later*, South Hadley MA, July 13–19 1996.
- [17] A. M. Dziewonski. Mapping the lower mantle: determination of lateral heterogeneity in P velocity up to degree and order 6. *Journal of Geophysical Research*, 89(B7):5929–5952, July 10 1984.
- [18] G. A. Eiby. *Earthquakes*. Muller, London, 1967.
- [19] T. Engelder. Geosc 20 homepage. Pennsylvania State University. November 1997. <http://www.geosc.psu.edu/~engelder/geosc20/>.
- [20] G. D. Garland. *Introduction to Geophysics — Mantle Core and Crust*. Saunders, Philadelphia, 1971.
- [21] The geometry center. University of Minnesota, November 1997. <http://www.geom.umn.edu/>.
- [22] D. Gubbins. *Seismology and plate tectonics*. Cambridge University Press, Cambridge, 1990.
- [23] Ó. Gudmundsson and M. Sambridge. A regionalized upper mantle (RUM) seismic model. *Journal of Geophysical Research*, in press, 1998.
- [24] B. Gutenberg and C. F. Richter. *Seismicity Of The Earth*. Princeton University Press, Princeton, 1949.
- [25] E. Hecht. *Optics*. Addison-Wesley, Reading MA, second edition, 1987.
- [26] E. W. Hobson. *The Theory of Spherical and Ellipsoidal Harmonics*. Cambridge University Press, London, 1931.
- [27] J. H. Hodgson. *Earthquakes and Earth Structure*. Prentice-Hall, New Jersey, 1964.

- [28] J. E. Hutchinson. Measure theory. Australian National University, Canberra, 1995.
- [29] H. Inoue, Y. Fakao, T. Tanabe, and Y. Ogata. Whole mantle P-wave travel time tomography. *Physics of the Earth and Planetary Interiors*, 59:294–328, 1990.
- [30] H. Jeffreys. *Earthquakes and Mountains*. Methuen, London 2nd edition, 1950.
- [31] M. J. S. Johnston, W. H. Bukan, L. C. Pakiser and A. C. Tarr. Earthquakes — can they be predicted or controlled? In R. R. Jones, editor, *the unsettled earth . . .*, pages 45–62. Ann Arbor Science, Michigan, 1975.
- [32] K. Kasahara. *Earthquake mechanics*. Cambridge earth science series. Cambridge University Press, Cambridge, 1981.
- [33] B. L. N. Kennett, E. R. Engdahl, and R. Buland. Constraints on seismic velocities in the Earth from traveltimes. *Geophysical Journal International*, 122:108–124, 1995.
- [34] W. H. K. Lee and V. Pereyra. Mathematical introduction to seismic tomography. In H. M. Iyer and K. Hirahara, editors, *Seismic Tomography: Theory and practice*, chapter 2, pages 9–22. Chapman and Hall, London, 1993.
- [35] A. Liu and B. Joe. Quality local refinement of tetrahedral meshes based on 8-subtetrahedron subdivision. *Mathematics of Computation*, 65(215):1183–1200, 1996.
- [36] T. Lo and P. L. Inderwiesen. *Fundamentals of Seismic Tomography*. Number 6 in Geophysical Monograph Series. Society of Exploration Geophysicists, Tulsa, 1994.
- [37] A. Michelini. An adaptive-grid formalism for travelttime tomography. *Geophysical Journal International*, 121:489–510, 1995.
- [38] T. J. Mitty, T. J. Baker, and A. Jameson/ Generation and adaptive alteration of unstructured three-dimensional meshes. In A. S.-Arcilla, J. Häuser, P. R. Eiseman, and J. F. Thompson, editors, *Numerical Grid Generation in Computational Fluid Dynamics and Related Fields*, pages 3–12. North-Holland, Amsterdam, 1991.
- [39] A. Morelli and A. M. Dziewonski. The harmonic expansion approach to the retrieval of deep Earth structure. In G. Nolet, editor, *Seismic Tomography*,

- Seismology and exploration geophysics, chapter 11, pages 251–274. D. Reidel, Dordrecht, 1987.
- [40] G. Nolet. Seismic wave propagation and seismic tomography. In G. Nolet, editor, *Seismic tomography*, Seismology and exploration geophysics, chapter 1, pages 1–23. D. Reidel, Dordrecht, 1987.
- [41] G. Nolet. Waveform tomography. In G. Nolet, editor, *Seismic tomography*, Seismology and exploration geophysics, chapter 13, pages 301–322. D. Reidel, Dordrecht, 1987.
- [42] G. Nolet. Solving large linearized tomographic problems. In H. M. Iyer and K. Hirahara, editors, *Seismic Tomography: Theory and practice*, chapter 9, pages 227–247. Chapman and Hall, London, 1993.
- [43] G. Nolet and B. Scheffers. Imaging with teleseismic data. In R. Cassinis, G. Nolet and G. F. Panza, editors, *Digital Seismology and Fine Modeling of the Lithosphere*, volume 42 of *Ettore Majorana international science series (physical sciences)*, pages 24–47. Plenum, New York, 1989.
- [44] A. Nur. Seismic rock properties for reservoir descriptions and monitoring. In G. Nolet, editor, *Seismic tomography*, Seismology and exploration geophysics, chapter 9, pages 203–235. D. Reidel, Dordrecht, 1987.
- [45] G. Nürnberg. *Approximation by Spline Functions*. Springer-Verlag, New York, 1989.
- [46] A. Plaza and G. F. Carey. About local refinement of tetrahedral grids based on bisection. In *5th International Meshing Roundtable*, Pittsburgh, October 10–11 1996.
- [47] M. C. Rivara. New mathematical tools and techniques for the refinement and/or improvement of unstructured triangulations. In *5th International Meshing Roundtable*, Pittsburgh, October 10–11 1996.
- [48] M. Sambridge. Earthquake location viewed as an inverse problem. In *Proceedings of a workshop on inverse problems*, pages 95–114, Canberra, 1986. Centre for Mathematics and Analysis, Australian National University.
- [49] M. Sambridge. *Seismic inversion for earthquake location and 3-d velocity structure*. PhD thesis, Australian National University, Canberra, October 1998.

- [50] M. Sambridge, J. Braun and H. McQueen. Geophysical parametrization and interpolation of irregular data using natural neighbours. *Geophysical Journal International*, 122:837–857, 1995.
- [51] M. Sambridge and Ó. Gudmundsson. Tomographic systems of equations with irregular cells. *Journal of Geophysical Research*, in press, 1998.
- [52] R. Snieder. Global inversions using normal modes and long-period surface waves. In H. M. Iyer and K. Hirahara, editors, *Seismic Tomography: Theory and practice*, chapter 3, pages 23–63. Chapman and Hall, London, 1993.
- [53] R. Snieder and M. Sambridge. Ray perturbation theory for traveltimes and ray paths in 3-d heterogeneous media. *Geophysical Journal International*, 109:294–322, 1992.
- [54] F. D. Stacey. *Physics of the Earth* Brookfield Pressm, Brisbane, third edition, 1992.
- [55] R. D. van der Hilst, S. Widiyantoro, and E. R. Engdahl. Evidence for deep mantle circulation from global tomography. *Nature*, 386:578–584, 10 April 1997.
- [56] A. van der Sluis and H. A. van der Vorst. Numerical solution of large, sparse linear algebraic systems arising from tomographic problems. In G. Nolet, editor, *Seismic tomography*, Seismology and exploration geophysics, chapter 3, pages 49–63. D. Reidel, Dordrecht, 1987.
- [57] Z. Wang and F. A. Dahlen. Spherical-spline parameterization of three-dimensional Earth models. *Geophysical Research Letters*, 22(22):3099–3102, 1995.
- [58] S. Widiyantoro. *Studies of seismic tomography on regional and global scale*. PhD thesis, Australian National University, Canberra, June 1997.
- [59] S. Yamamuro. *Differential Calculus in Topological Linear Spaces*, volume 374 of *Lecture Notes in Mathematics*. Springer-Verlag, New York, 1974.